

Sizing Aerosol Particles between One and Three Nanometers

Thesis By

Nicholas Anthony Brunelli

In Partial Fulfillment of the Requirements

for the Degree of

Doctor of Philosophy

CALIFORNIA INSTITUTE OF TECHNOLOGY

Pasadena, California

2010

(Defended December 4, 2009)

© 2010

Nicholas Anthony Brunelli

All Rights Reserved

Acknowledgements

Remember Love, and nothing else will matter. — Anon.

*You cannot teach a man anything; you can only help him find it within himself.
— Galileo Galilei*

I have had the pleasure of becoming good friends with many and learning from even more during my time at Caltech. Each will always hold a special place in my heart for who they are and what they have taught me. Without each one, I would not be the scientist, friend, or husband that I am. I could easily write an entire chapter about the memorable times, the struggles that friends have helped me through, and the numerous learning experiences that I have had, but I will limit myself to a few in particular.

First and foremost, I would like to thank my wife, Yoshie Narui. She is simply the best: listening to me, helping me, baking for me, and loving me. She has enabled me to achieve far greater accomplishments. Words cannot express my love and gratitude for her.

I would also like to acknowledge my family (mom, dad, Jeff, Bill, Mr. and Mrs. Narui (i.e. dad and mom #2), and Mitsu amongst the many others). You all have given me the strength, wisdom, motivation, and encouragement to succeed.

My research advisor Professor Konstantinos P. Giapis also deserves credit for my work as well. I am a more thoughtful, more patient, and more creative researcher due to his guidance. I entered Caltech as a naïve student and will leave Caltech confident in my analytical ability as a researcher. My favorite times will always be the long discussions that inevitably arose that would pique my interest in a topic of which I was usually unaware. His passion for knowledge has contributed to mine.

My work has also benefitted tremendously from the guidance of Professor Richard C. Flagan. His insistence that I take his aerosol physics class developed a passion that I never knew was there. Ultimately, our conversations have led to more questions than answers, but this is the true essence of science.

I would also like to acknowledge with great sincerity a particularly close group of friends: Chris and Sarah Alabi, Jason Gamba and Ashley Rhodes, Brendan and Charlotte Mack, John McKeen. I have the true pleasure of calling each of you my dear friend. You are all very special to me for your own reasons. I would be remiss not to mention my many thanks to John for arranging for me to stay with his family (Chuck, Linda, Mike, and Louie) while I did some experiments at the University of Minnesota.

The former members of my lab (Oleksandr, Xiangdong, Mike, Mohan, Jongwon, Carolyn, John “Ace,” and David) and those that I have done work with (Evan, Professor Jack L. Beauchamp, Jingkun, Dr. Attoui, Rob, Dave, Mary, Áron, Professor Sossina M. Haile, Dean, Adam, Julian) have been wonderful resources. Oleksandr helped me think about the nano-scopic world with his simulations. Xiangdong provided endless discussions about the most important topics (i.e., college football). Mohan introduced me to the microplasmas. Mike made me think more deeply about the problems that I was trying to solve and introduced me to the world of circuitry.

The members of the Davis lab (Eric, Heather, Leonard, John, Jonathan, Jelena, Ray, Ryan, Yasho, Yuri) and Professor Mark E. Davis have been particularly nice to me, allowing me to celebrate along with them and helping me with experiments. Their camaraderie and scientific discussions have made all the long days and nights well-worth working.

I would like to acknowledge Mike Vicic who has been a valued mentor to me. Our discussions of the educational process will always keep me CALM when I go into the classroom. He has provided me with many insights and a frank analysis that is truly eye-opening.

A special thanks goes out to Ernie and the members of the soccer team on which I have played (Ernie's A. F.). Our team has always played hard together and never let the score affect our attitude on the field. I hope the team will continue well-beyond the time that I am here.

Finally, I must thank Mike, Steve, Rick, Jaime, and Efrain. Mike and Steve taught me how to machine the parts and without them my thesis would not be possible. Rick regaled me constantly with stories of his vacation, making it seem like I had been there myself. Jaime and Efrain have been constant sources of motivation.

Abstract

The measurement of nanoparticle size is of primary importance to the fields of aerosol science and nanotechnology. Size affects the aerosol dynamics and impacts the optical, magnetic, and catalytic properties of nanoparticles. The size range from 1 to 10 nm is of particular interest because quantum effects and ambient aerosol nucleation occur in this range. Differential Mobility Analyzers are the primary instruments used currently to measure the size of aerosol particles, but diffusion impairs significantly their ability to size in the lower range (1–3 nm).

A primary focus of this thesis work has been to design, construct, and test a Radial Differential Mobility Analyzer, termed “nano-RDMA,” capable of measuring nanoparticles in the 1 to 12.5 nm size range with high resolution and transmission. The nano-RDMA was calibrated using electrospray techniques to aerosolize molecular ions for mobility analysis. The instrument was determined to have significantly improved resolution and transmission than the commercially available nano-DMA. Simulations of the nano-RDMA operation were performed to determine how the resolution could be improved.

The nano-RDMA has been employed to characterize *in-situ* size distributions of particles produced in an atmospheric pressure microplasma reactor. The operating parameters of the microplasma (i.e., plasma current, flow rate, precursor concentration, and precursor composition) were investigated to determine the effect on particle size distribution. The microplasma was further examined as a calibration source for narrow size distributions. Iron nanoparticles produced with the microplasma were used to grow nanotubes catalytically. A correlation was established between the size of the grown carbon nanotubes and the catalytic particles produced in the microplasma.

The nano-RDMA was also used as a size characterization and selection device in particle overgrowth experiments. Silicon nanoparticles produced in the microplasma were introduced into two different processing stages: a second microplasma and a furnace. The nano-RDMA permitted quick evaluation of how the operating conditions of the second processing stage affected overgrowth. The broad size distributions indicated that agglomeration was contributing to the measured size distribution, leading to the adoption of a Tandem DMA (TDMA) arrangement for overgrowth experiments. Limiting the size distribution with the first nano-RDMA permitted homogeneous overgrowth of silicon nanoparticles.

The microplasma was also investigated as a possible calibration source using the TDMA arrangement. While the microplasma produced a stable size distribution with a high concentration of nanoparticles, the measured resolution was lower than expected. The TDMA arrangement permitted studies of the thermal annealing of silicon nanoparticles. The particle size was observed to decrease with increasing temperature in a manner consistent with hydrogen evolution.

Table of Contents

| | |
|---|-------|
| List of Figures | xiv |
| List of Tables | xviii |
| List of Nomenclature | xix |
| Chapter 1: Introduction | 1 |
| 1.1. Introduction and Background | 1 |
| 1.2. Plasma Background | 3 |
| 1.3. Aerosol Mobility Measurements Background | 4 |
| 1.3.1. Particle Size | 5 |
| 1.3.2. Particle Concentration | 7 |
| 1.3.3. Log-Normal Distribution | 8 |
| 1.3.4. Agglomeration | 8 |
| 1.4. Dissertation Outline | 10 |
| References | 12 |
| Chapter 2: Radial Differential Mobility Analyzer for One Nanometer Particle Classification | 14 |
| 2.1. Introduction | 14 |
| 2.2. Experimental Method | 17 |
| 2.2.1. Instrument Design | 17 |
| 2.2.2. Instrument Calibration | 20 |
| 2.2.3. Instrument Coupling with Mass Spectrometer (in Collaboration) | 22 |
| 2.2.4. Instrument Comparison to Other DMAs (in Collaboration) | 23 |
| 2.3. Results | 25 |

| | |
|--|----|
| 2.3.1. Calibration..... | 25 |
| 2.3.2. Results: Mass Spectrometry..... | 26 |
| 2.3.3. Results: DMA Comparison..... | 27 |
| 2.4. Discussion..... | 28 |
| 2.4.1. Calibration..... | 28 |
| 2.4.2. Mass Spectrometry..... | 31 |
| 2.4.3. DMA Comparison..... | 32 |
| 2.5. Summary..... | 32 |
| References..... | 48 |
| Chapter 3: Finite Element Analysis of the nano-RDMA Geometry..... | 50 |
| 3.1. Introduction..... | 50 |
| 3.2. Theoretical Considerations..... | 54 |
| 3.3. Results and Discussion..... | 57 |
| 3.3.1. Electrostatics..... | 57 |
| 3.3.2. Incompressible Navier-Stokes..... | 58 |
| 3.3.3. Electrokinetic Flow..... | 58 |
| 3.3.4. Calibration Factor..... | 59 |
| 3.3.5. Resolution..... | 60 |
| 3.4. Summary..... | 63 |
| References..... | 79 |
| Chapter 4: Microhollow Cathode Discharge Operating Conditions Impact on Nanoparticle Size Production..... | 81 |
| 4.1. Introduction..... | 81 |

| | |
|--|-----|
| 4.2. Experimental Method..... | 82 |
| 4.3. Results and Discussion | 84 |
| 4.4. Summary | 86 |
| References..... | 95 |
| Chapter 5: Nanoparticle Production from Cathode Sputtering in High-Pressure Microhollow Cathode and Arc Discharges..... | 96 |
| 5.1. Introduction..... | 96 |
| 5.2. Experimental Method..... | 97 |
| 5.3. Results and Discussion | 98 |
| 5.4. Summary | 101 |
| References..... | 105 |
| Chapter 6: Microdischarge Synthesis of Fe Nanoparticles for Diameter-Controlled Growth of Carbon Nanotubes..... | 106 |
| 6.1. Introduction..... | 106 |
| 6.2. Experimental Method..... | 107 |
| 6.3. Results and Discussion | 110 |
| 6.4. Summary | 113 |
| References..... | 120 |
| Chapter 7: Instrument Calibration Using Tandem Differential Mobility Analysis with a Microplasma Source | 122 |
| 7.1. Introduction..... | 122 |
| 7.2. Experimental Method..... | 124 |
| 7.3. Results and Discussion | 127 |

| | |
|--|-----|
| 7.4. Summary | 132 |
| References..... | 141 |
| Chapter 8: Size Evolution of Annealed Silicon Nanoparticles..... | 143 |
| 8.1. Introduction..... | 143 |
| 8.2. Experimental Description | 145 |
| 8.3. Results and Discussion | 146 |
| 8.4. Summary | 150 |
| References..... | 157 |
| Chapter 9: Particle Size and Surface Modification of Aerosol Silicon Nanoparticles ... | 158 |
| 9.1. Introduction..... | 158 |
| 9.2. Experimental Method..... | 160 |
| 9.2.1. Dual Microplasma Setup..... | 160 |
| 9.2.2. Overgrowth | 162 |
| 9.2.3. Size-Selected Overgrowth | 163 |
| 9.3. Results and Discussion | 164 |
| 9.3.1. Dual Microplasma..... | 164 |
| 9.3.2. CVD Overgrowth..... | 167 |
| 9.3.3 Size-Selected Overgrowth | 168 |
| 9.4. Summary | 169 |
| References..... | 181 |
| Chapter 10: Future Work | 182 |
| 10.0. Introduction..... | 182 |
| 10.1. Improved Electrospray Apparatus | 182 |

| | |
|--|-----|
| 10.2. Conductivity of Nanoscale Solid Acid Fuel Cell..... | 183 |
| 10.3. Tandem Differential Mobility Analyzer Growth of Carbon Nanotubes..... | 185 |
| 10.4. Sensitive Faraday Cup Electrometer..... | 186 |
| 10.5. Nanoparticle Calibration Source for Differential Mobility Analyzers | 187 |
| 10.6. Nanoparticle Synthesis Using a Water Plasma Electrospray..... | 188 |
| References..... | 192 |
| Appendix I: Electrospray Sources | 193 |
| A1.1 Introduction..... | 193 |
| A1.2 Electrospray Apparatus: Detailed Assembly | 194 |
| A1.2.1 The Liquid Delivery System..... | 194 |
| A1.2.2 Electrospray for Volatilization of Molecular Ions | 195 |
| A1.2.3 Electrospray for Nano-structured Electrodes..... | 197 |
| Appendix II: Composite Nano-structured Solid Acid Fuel Cell Electrodes via Electrospray Deposition..... | 202 |
| A2.1. Introduction..... | 202 |
| A2.2. Experimental Method..... | 204 |
| A2.2.1. Deposition | 204 |
| A2.2.2. Solution Properties..... | 205 |
| A2.2.3. Oxygen Plasma Treatment..... | 206 |
| A2.2.4. AC Impedance Measurements | 206 |
| A2.3. Results and Discussion..... | 207 |
| A2.4. Summary | 209 |
| References..... | 222 |

| | |
|---|-----|
| Appendix III: A Tool for Uniform Coating of 300 mm Wafers with Nanoparticles..... | 223 |
| A3.1. Introduction..... | 223 |
| A3.2. Design | 227 |
| A3.3. Experimental Apparatus and Methods..... | 233 |
| A3.4. Results..... | 235 |
| A3.5. Conclusions..... | 237 |
| References..... | 255 |

List of Figures

| | |
|--|----|
| Figure 2.1. Simplified Schematic of RDMA Operation. | 34 |
| Figure 2.2. Detailed Schematic of the nano-RDMA..... | 35 |
| Figure 2.3. Schematic of Electrospray..... | 36 |
| Figure 2.4. Schematic of nano-RDMA and Mass Spectrometer. | 37 |
| Figure 2.5. Schematic of TDMA. | 38 |
| Figure 2.6. Inverse Mobility Distributions. | 39 |
| Figure 2.7. Geometric Mean Mobilities..... | 40 |
| Figure 2.8. Inverse Mobility Distributions. | 41 |
| Figure 2.9. Inverse Mobility Distributions Using Mass Spectrometer as Detector. | 42 |
| Figure 2.10. Mobility Distribution of Monomer and Dimer Using MS. | 43 |
| Figure 2.11. Mobility Distribution Comparison between nano-RDMA and nano-DMA. | 44 |
| Figure 2.12. Mobility Distribution of TMAI. | 45 |
| Figure 2.13. nano-RDMA Resolution..... | 46 |
| Figure 3.1. Outline of the Axis-Symmetric Model. | 64 |
| Figure 3.2. Electrostatics Solution..... | 65 |
| Figure 3.3. Inset of Aerosol Inlet Region. | 66 |
| Figure 3.4. Electrostatics Solution without Mesh..... | 67 |
| Figure 3.5. Navier-Stokes Solution..... | 68 |
| Figure 3.6. Electrokinetic Flow Solution..... | 69 |
| Figure 3.7. Electrokinetic Flow Solution without Mesh..... | 70 |
| Figure 3.8. Calibration Factor for Electrode Spacing..... | 71 |
| Figure 3.9. Calibration Factor for Aerosol Inlet Gap..... | 72 |
| Figure 3.10. Resolution of nano-RDMA. | 73 |
| Figure 3.11. Resolution for Different Electrode Spacings..... | 74 |
| Figure 3.12. Resolution for Different Aerosol Outlet Gaps..... | 75 |
| Figure 3.13. Resolution for Different Aerosol Inlet Gaps. | 76 |
| Figure 3.14. Electrokinetic Flow Solution at Optimal Voltage. | 77 |
| Figure 3.15. Resolution Comparison Between the nano-RDMA and RDMA. | 78 |
| Figure 4.1. Schematic of Microplasma. | 88 |

| | |
|---|-----|
| Figure 4.2. Schematic of Microplasma Deposition. | 89 |
| Figure 4.3. Size Distribution for Different Plasma Currents. | 90 |
| Figure 4.4. Size Distribution for Different Silane Concentrations. | 91 |
| Figure 4.5. Size Distribution for Different Plasma Flow Rates. | 92 |
| Figure 4.6. Size Distribution of Germanium Nanoparticles. | 93 |
| Figure 4.7. EDS of Germanium Nanoparticles. | 94 |
| Figure 5.1. Schematic of Sputtering Discharges. | 102 |
| Figure 5.2. Size Distributions of Positive Charged Particles. | 103 |
| Figure 5.3. Distribution of Negative Charged Particles. | 104 |
| Figure 6.1 Schematic of Microplasma for Fe Nanoparticles. | 114 |
| Figure 6.2. Size Distributions of Iron Nanoparticles. | 115 |
| Figure 6.3. AFM Images of CNTs. | 116 |
| Figure 6.4. Size Distribution of Nanotube Diameters. | 117 |
| Figure 6.5. Size Variation of Nanotubes and Nanoparticles. | 118 |
| Figure 7.1 Schematic of Tandem DMA. | 133 |
| Figure 7.2. Mobility Distribution from First nano-RDMA. | 134 |
| Figure 7.3. TDMA Mobility Distributions. | 135 |
| Figure 7.4. Normalized TDMA Mobility Distributions. | 136 |
| Figure 7.5. Shift of TDMA Mobility Distribution. | 137 |
| Figure 7.6. Transmission of the nano-RDMA. | 138 |
| Figure 7.7. Resolution Measured with the Tandem DMA. | 139 |
| Figure 8.1. Schematic of Tandem DMA Sintering Arrangement. | 151 |
| Figure 8.2. Size Distribution of First and Second nano-RDMA. | 152 |
| Figure 8.3. Size Variation of 3.1 nm Silicon Nanoparticles with Temperature. | 153 |
| Figure 8.4. Size Variation of 2.7 nm Silicon Nanoparticles with Temperature. | 154 |
| Figure 8.5. Size Variation of 1.7 and 1.3 nm Silicon Nanoparticles with Temperature. | 155 |
| Figure 8.6. Comparison of Size Variation with Temperature. | 156 |
| Figure 9.1. Schematic of Dual Microplasma. | 170 |
| Figure 9.2. Schematic of the Overgrowth Arrangement. | 171 |
| Figure 9.3. Schematic of the Tandem DMA Overgrowth Arrangement. | 172 |
| Figure 9.4. Size Distribution of the Dual Microplasma. | 173 |

| | |
|---|-----|
| Figure 9.5. Size Distribution of Dual Microplasma with Additional Silane. | 174 |
| Figure 9.6. Size Distribution Produced with Dual Microplasma Varying First Gap..... | 175 |
| Figure 9.7. Size Distribution Produced with Dual Microplasma Varying Second Gap. | 176 |
| Figure 9.8. Size Distribution with Overgrowth with Diffusion Mixing. | 177 |
| Figure 9.9. Size Distribution with Overgrowth with Jet Mixing. | 178 |
| Figure 9.10. Size Distribution without Overgrowth from Single Microplasma. | 179 |
| Figure 9.11. Size Distribution with Overgrowth in the Tandem DMA Arrangement.... | 180 |
| Figure 10.1. Electrospray Plasma | 191 |
| Figure A1.1. Schematic of the Electrospray Source. | 199 |
| Figure A1.2. Electrospray. | 200 |
| Figure A1.3. Schematic of Electrospray. | 201 |
| Figure A2.1. Fuel Cell Electrode Particle Size Comparison. | 211 |
| Figure A2.2. Schematic of the Electrospray. | 212 |
| Figure A2.3. Fuel Cell Assembly. | 214 |
| Figure A2.4. Nano-structured CDP. | 215 |
| Figure A2.5. X-ray Diffraction of CDP. | 216 |
| Figure A2.6. Dense CsH_2PO_4 Film. | 217 |
| Figure A2.7. Effect of Aging on Nano-structure. | 218 |
| Figure A2.8. Stabilized Electrode Nano-structure. | 219 |
| Figure A2.9. FTIR of Electrosprayed Electrode. | 220 |
| Figure A2.10. Impedance Plot | 221 |
| Figure A3.1. Schematic of Thermophoretic Depositor with Isotherms. | 239 |
| Figure A3.2. Modeled Temperature Profile. | 240 |
| Figure A3.3. Modeled Velocity Contours for Flow Rates of 1.5 and 15 SLM. | 241 |
| Figure A3.4. Modeled Velocity Contours for Flow Rates of 35 and 60 SLM. | 242 |
| Figure A3.5. Modeled Temperature Contours. | 243 |
| Figure A3.6. Modeled Stream Function Plots. | 244 |
| Figure A3.7. Modeled Deposition Profile. | 245 |
| Figure A3.8. Modeled Deposition Profile. | 246 |
| Figure A3.9. Modeled Deposition Profile. | 247 |
| Figure A3.10. Modeled Deposition Profile. | 248 |

| | |
|---|-----|
| Figure A3.11. Plot of Deposition Profile..... | 249 |
| Figure A3.12. Particle Size Distribution and Wafer Coverage..... | 250 |
| Figure A3.13. AFM Images of Deposited Particles..... | 251 |
| Figure A3.14. Modeled Inlet Temperature Distribution without Inlet Heating..... | 252 |
| Figure A3.15. Deposition Profile without Inlet Heating..... | 253 |
| Figure A3.16. Particle Deposition without Inlet Heating. | 254 |

List of Tables

| | |
|---|-----|
| Table 2.1. Mobility Data..... | 47 |
| Table 6.1 Measured Particle Size..... | 119 |
| Table 7.1. Fitting Parameters of First nano-RDMA Mobility Distributions | 140 |
| Table A2.1. Critical Electrospray Parameters..... | 213 |

List of Nomenclature

| | |
|----------|--|
| b | Electrode gap spacing (mm) |
| E | Electric field (V m^{-1}) |
| k | Boltzmann constant ($1.38 * 10^{-23} \text{ J K}^{-1}$) |
| m | Mass of background gas molecule (kg) |
| P | Pressure (pascal) |
| q | Elementary unit charge ($1.602 * 10^{-19}$ coulomb) |
| Q_a | Aerosol inlet flow rate (LPM, SLM or sccm) |
| Q_e | Excess outlet flow rate (LPM, SLM or sccm) |
| Q_s | Sample outlet flow rate (LPM, SLM or sccm) |
| Q_{sh} | Sheath inlet flow rate (LPM, SLM or sccm) |
| R_i | Inner radius of electrode (mm) |
| R_o | Outer radius of electrode; aerosol inlet radius (mm) |
| T | Temperature (K) |
| v_m | Migration velocity (cm s^{-1}) |
| Z_P | Electrophoretic mobility ($\text{cm}^2 \text{ V}^{-1} \text{ s}^{-1}$) |
| Z_P^* | Ideal electrophoretic mobility ($\text{cm}^2 \text{ V}^{-1} \text{ s}^{-1}$) |
| δ | Mobility shift (Z_P / Z_P^*) |
| η | Transmission |

Chapter 1: Introduction

1.1. Introduction and Background

Science is immersed in a period of investigating objects with dimensions on the nanoscale, including nanometer thick films (quantum wells), nanorods, nanotubes, nanowires, and nanoparticles. These objects often have optical,[1] magnetic,[2] and/or catalytic[3] properties that are different from micron-scale materials due to the quantum confinement effect. The smallest of these objects is the nanoparticle, and it can serve as the active component of a system[4] or can be used in the synthesis of nanorods,[5] nanotubes,[6] and nanowires.[7] The flexibility of nanoparticles increases its potential as a building block in future, more-complex structures.

Nanoparticles have been synthesized in many different ways, including using liquid and gas-phase techniques. For liquid techniques, each new particle composition requires a new optimization procedure of the synthesis parameters (i.e., precursor, concentration, surfactant, temperature, solvent) to obtain a narrow particle size distribution for the desired application. This process is inefficient if a small quantity of nanoparticles is desired for a particular application.

Gas-phase synthesis is preferred due to the continuous nature of particle production and the ease of manipulating aerosol particles. The classic reactor for nanoparticle production is the Sinclair–La Mer generator[8] that creates nanoparticles through the thermal decomposition of a precursor in a furnace at high temperatures. The reactor volume required to achieve high temperatures leads to long residence times, causing the particles to agglomerate and a broadening of the particle size distribution. A

narrower distribution of particles was obtained through using mixing jets to dilute the nanoparticles before agglomeration occurred.[9] Yet, a major obstacle for these systems is that the reactor walls tend to become coated with decomposed precursor and nanoparticles eventually fouling the reactor to the point that nanoparticle synthesis is no longer viable.

A microplasma is a simple, generic synthesis route for small quantities of nanoparticles of many chemical compositions.[10] Synthesis involves passing a gaseous precursor through the microplasma, where it decomposes and forms nanoparticles. The short residence time provides an intense reaction zone to produce nanoparticles. The microplasma operates steadily for hours, producing stable particle size distributions. The particle size distribution was measured *in situ* using a Radial Differential Mobility Analyzer (RDMA).

The combination of the microplasma and the RDMA was a solid initial platform on which to build, but was incapable of measuring these small particles without significant distortion of the size distribution. The microplasma produced particles in the 1 to 5 nm size range, and the RDMA was optimized for particle size measurements in the 8 to 100 nm size range.[11] The lower size limit of the RDMA is due to diffusion that causes measured size distributions to appear broader than they actually are. The breadth of a size distribution is an important indicator of the growth process. Broad distributions tend to result when growth occurs due to agglomeration whereas narrow distributions are the result of homogeneous nucleation.

The approach taken in this dissertation was to construct a new RDMA (i.e., the nano-RDMA) capable of measuring particle size as small as 1 nm, believed to be

produced in the microplasma. Before presenting any results on this combination, a brief background will be given on the individual topics.

1.2. Plasma Background

Plasma is a state of matter that consists of ions, electrons, and neutrals where the ionized species represent a significant percentage of the overall number density (i.e., 0.01% to 10%).[12] The large number density of the ions and electrons leads to the plasma volume being conductive and causes the plasma to exhibit collective dynamics with the presence of each species (i.e., ions and electrons) causing fields and influencing the motion of the other species.

Plasma operation is strongly influenced by the number density of neutrals, which is directly related to the system pressure. The microplasma used throughout this dissertation is a direct current microhollow cathode discharge (MHCD) that operates at atmospheric pressure. Sustaining a plasma at atmospheric pressure is quite difficult due to the numerous collisions between the ions and electrons that will quench the plasma.

The geometry of the MHCD facilitates this process. The MHCD consists of two electrodes with the cathode biased negatively with respect to the anode that are placed a fixed distance apart. The cathode is the crucial electrode and is cylindrical in nature with a characteristic radius on the order of 100 μm to decrease the electric field required to initiate the discharge. Inside the cathode, the high-energy electrons are created, and correspondingly the most intense plasma exists here.

The plasma glow extends from the inner volume of the cathode to the anode. The conductive nature of the plasma results in a small voltage drop across the plasma volume. Without the MHCD, the electric field is mainly in the axial direction, but with the

MHCD, the electric field becomes radial in direction with a strong electric field developing between the electrode and the plasma. The radial electric field confines the electrons inside the cathode and causes them to oscillate in a manner known as the Pendel effect.[13]

The second impact of the number of collisions at atmospheric pressure is collision-induced heating. Ions are accelerated and collide with neutral gas molecules transferring energy to the background gas molecules. The collisions increase the neutral gas temperature.

The combination of joule heating and high-energy electrons facilitate the decomposition of gas molecules in the MHCD. Decomposed gaseous precursor may lead to a local supersaturation of growth species that cluster and form nanoparticles. These become naturally charged due to the electrons and ions in the discharge and emerge as an aerosol.

1.3. Aerosol Mobility Measurements Background

An aerosol consists of a suspension of fine particles dispersed in a gas. The behavior of the particles is dependent upon and characterized by a number of factors. The most critical parameters for the studies considered herein are particle concentration, size, and size range. The goals of this section will be to discuss the topics of aerosol research relevant to this work, to give a brief overview of how these topics are related, and to indicate reasoning behind decisions made about equipment and analysis. The concepts discussed in this section will be utilized extensively in the following chapters without further explanation.

1.3.1. Particle Size

The relevant physics of particle motion are determined by the number and type of interactions with the background gas molecules. The dimensionless group that accounts for these interactions is the Knudsen number (Kn), defined as

$$Kn = \frac{2\lambda}{D_p}, \quad (1.1)$$

where λ is the mean free path of the background gas molecules and D_p is the mobility diameter of the particle. Small values of Kn (i.e., $Kn \ll 1$) correspond to the continuum limit, a regime in which particle motion is impeded due to collisions with the background gas. The mobility of a particle (B) in this regime is defined by the well-known Stokes-Einstein relationship:

$$B = \frac{1}{3\pi\mu D_p}, \quad (1.2)$$

where μ is the viscosity. The mobility relationship is different when the value of Kn nears unity (i.e., the transition regime). An empirical factor (the Stokes–Cunningham slip correction factor $C_c(Kn)$), [14] is introduced to account for the apparent slippage of gas molecules past the surface of the particle. The mobility relationship becomes

$$B = \frac{C_c(Kn)}{3\pi\mu D_p}. \quad (1.3)$$

This relationship holds for all values of Kn . The slip correction factor is directly proportional to Kn at large values of Kn . The mobility becomes proportional to the inverse of the diameter squared, indicating that smaller particles are more mobile due to decreased resistance to motion. The inverse squared dependence on diameter is the same that is observed for particle mobility in the free-molecular limit, which is

$$B = 0.441 \frac{(k_B T / m)^{0.5}}{p D_p^2}, \quad (1.4)$$

where k_B is the Boltzmann constant, T is the temperature, m is the mass of the background gas molecule, and p is the pressure. Given that the value of λ at standard conditions is approximately 60 nm and the particle diameters considered in this report are 10 nm and smaller, the transition regime expression will be utilized to convert particle mobility to mobility diameter.

The particle mobility diameter assumes that the particle is spherical. Formulas to account for different particle shapes can be applied,[15] but the particles measured in this report were not expected to be aspherical. The particle mobility diameter is not equivalent to the particle diameter, and the error in assuming so becomes important as the size approaches molecular and atomic dimensions. Tammet recognized the difference could be corrected with a simple formula:

$$d = D_p - d_g, \quad (1.5)$$

where d is the actual diameter of the particle and d_g is a correction related to the finite diameter of the background gas.[16] The value of d_g has been calculated from a few sources to be approximately 0.55 nm.[17]

The previous mobility expressions have been presented in terms of resistance to particle motion. The motion of the particle can be due to a variety of sources, including thermal energy (diffusivity) and electrical potential energy (electrophoretic mobility), resulting in the following mobility expressions:

$$D = B * k_B T; \quad (1.6)$$

$$Z_p = B * i q, \quad (1.7)$$

where D is the diffusivity, Z_p is the electrophoretic mobility, i is the number of elementary charges on a particle and q is the fundamental unit of charge (i.e., $1.602 * 10^{-19}$ coulombs). Diffusion causes an isotropic motion of the particle whereas electrophoretic motion is a directional process that depends on the electric field, E . The directionality can be exploited to classify aerosol nanoparticles according to their electrophoretic mobility due to differences in mobility diameter. The standard aerosol equipment to perform this separation is the differential mobility analyzer (DMA). A more complete description of the DMA will be provided in chapter 2.

1.3.2. Particle Concentration

Particle concentration is measured typically with two devices: a condensation particle counter (CPC) and a faraday cup electrometer (FCE). The CPC is primarily used for detection of low particle concentrations. CPC operation is based on measuring scattered light intensity from particles that have been enlarged through condensing a working fluid on the surface of the particle. It can be used to detect both neutral and charged particles, and the presence of multiple charges does not influence the detected concentration. The detector is ideal for many applications except those involving small particle sizes (<2.5 nm), as small particles can not be overgrown to larger sizes and therefore cannot be detected. Considerable research is currently underway to overcome this size limit.[18]

The FCE is used primarily for detection of high concentrations of charged particles found largely in nanoparticle synthesis systems. It detects particles through the current generated by charged particles that are collected on filter cartridges. No lower size limit exists for the FCE as the filtration efficiency improves as particle size

decreases. The limit on FCE operation is that detected currents must be greater than ± 1 fA, as the Johnson noise of the high impedance resistor in the detection circuit impedes detection below approximately 0.5 fA.[19] For the experiments described herein, the particle sizes detected were below the lower size limit of available CPCs and the measured concentrations were high ($\gg 1$ fA). Therefore, the FCE was the primary particle detection instrument.

1.3.3. Log-Normal Distribution

The total particle concentration and particle size can be measured independently, but significant information is gained about the system when measured together. The combination of size and concentration naturally lends itself toward analysis with a distribution function. For aerosol applications, the appropriate function is the log-normal distribution:[20]

$$f(D_p, N, D_{pg}, \sigma_g) = \frac{N}{(2\pi)^{0.5} \ln \sigma_g} \exp\left(-\frac{1}{2} \left(\frac{\ln D_p - \ln D_{pg}}{\ln \sigma_g}\right)^2\right) \quad (1.8)$$

where D_p is the mobility diameter, N is the concentration, D_{pg} is the geometric mean mobility diameter, and σ_g is the geometric standard deviation. The geometric standard deviation indicates the range of particle sizes. Its value provides important insight on the dynamics of the aerosol such as the importance of agglomeration.

1.3.4. Agglomeration

Agglomeration is the result of two particles colliding and sticking together, resulting in a physically larger particle (i.e., increases D_{pg} and σ_g) and a net loss of one

particle (i.e., decreases N). The agglomeration process between two particles (i and j) has been described theoretically as a rate ($J_{i,j}$), using the following equation:[14]

$$J_{i,j} = K_{i,j} N_i N_j, \quad (1.9)$$

where $K_{i,j}$ is the agglomeration coefficient and N_i is the concentration of particles with size i . The coefficient $K_{i,j}$ has many different forms, but generally depends on the diameters of the particles involved in the collision. Interestingly, $K_{i,j}$ is minimized when $i = j$, as particles with the same size will have the same mobility. These particles will move at the same rate, resulting in a average relative rate of motion that is smaller than if the particles were not the same size. This implies that monodisperse distributions will remain monodisperse longer than polydisperse aerosols of the same concentration. As the agglomeration process naturally creates a polydisperse aerosol, the distribution will continue to broaden (i.e., larger σ_g) with time until a self-preserving distribution (at t_{spd}) is reached that is characterized by a $\sigma_g > 1.3$. The particle concentration will decrease rapidly past t_{spd} . [14]

The particle size and concentration are the most important parameters in determining the amount of time before agglomeration will impact the measured size of the distribution. High concentration (N) and polydisperse (larger σ_g) aerosols will decrease the onset time for the effects of agglomeration. The effects of agglomeration can be overcome through reducing the number concentration and narrowing the size distribution, as is accomplished in the Tandem DMA (TDMA) arrangement (discussed further in chapters 8 and 9).

1.4. Dissertation Outline

The remaining chapters chronicle a majority of the work that has been completed. Chapter 2 will present work associated with the design, construction, and testing of the new differential mobility analyzer (i.e., the nano-RDMA). It will include instrument calibration results found using molecular ions, and work completed in collaboration with others. The mass spectroscopy work to confirm the identity of the molecular ion was completed with Evan Neiholdt in the lab of Professor J. L. Beauchamp. The comparison of the nano-RDMA to other DMAs was completed with Dr. Jingkun Jiang and Professor M. Attoui in the lab of Professor P. McMurry. Chapter 3 will present finite element simulations used to characterize the ideal operation of the nano-RDMA, and will include some recommended improvements to the nano-RDMA construction.

The remaining chapters will report work completed with the combination of the microplasma and the nano-RDMA. Chapter 4 will present some work completed to characterize the production of nanoparticles with the microplasma that was improved due to the use of the nano-RDMA. Particles were observed for lower precursor concentration than previously reported (i.e., <3 ppm) as well as without precursor due to cathode sputtering. The size distribution of particles produced from cathode sputtering are presented in chapter 5. The flexibility of the microplasma is demonstrated in chapter 6, where narrow size distributions of iron nanoparticles were synthesized. The iron nanoparticles were shown to produce similarly narrow distributions of carbon nanotubes. The growth of carbon nanotubes was completed in collaboration with Professor J. Kim.

Chapter 7 will discuss the microplasma as a particle source to calibrate the nano-RDMA in the Tandem DMA (TDMA) arrangement. The ability of the TDMA

arrangement will be demonstrated in chapter 8, where the size evolution of silicon nanoparticles is monitored as a function of the thermal processing temperature. While chapter 8 demonstrates the size reduction of silicon nanoparticles, chapter 9 will discuss the methods used to grow silicon nanoparticles to larger sizes.

Finally, some ideas for future work will be presented in chapter 10 before the electro spray sources created (appendix I) and some collaborative work completed with other students will be described (appendix II with Áron Varga and appendix III with Dean Holunga).

References

1. L. Canham, *Applied Physics Letters*, **57**, 1046, 1990.
2. S. Sun, and C. Murray, *Journal of Applied Physics*, **85**, 4325, 1999.
3. J. Grunes, J. Zhu, M. Yang, and G. Somorjai, *Catalysis Letters*, **86**, 157, 2003.
4. M. Ostraat, J. De Blauwe, M. Green, L. Bell, M. Brongersma, J. Casperson, R. Flagan, and H. Atwater, *Applied Physics Letters*, **79**, 433, 2001.
5. N. Jana, L. Gearheart, and C. Murphy, *Journal of Physical Chemistry B*, **105**, 4065, 2001.
6. Y. Li, W. Kim, Y. Zhang, M. Rolandi, D. Wang, and H. Dai, *Journal of Physical Chemistry B*, **105**, 11424, 2001.
7. Y. Cui, L. Lauhon, M. Gudiksen, J. Wang, and C. Lieber, *Applied Physics Letters*, **78**, 2214, 2001.
8. D. Sinclair, and V. La Mer, *Chemical Reviews*, **44**, 245, 1949.
9. D. Holunga, R. Flagan, and H. Atwater, *Industrial and Engineering Chemical Research*, **44**, 6332, 2005.
10. R. Sankaran, D. Holunga, R. Flagan, and K. Giapis, *Nano Letters*, **5**, 537, 2005.
11. S. Zhang, Y. Akutsu, L. Russell, R. Flagan, and J. Seinfeld, *Aerosol Science and Technology*, **23**, 357, 1995.
12. M. Lieberman, and A. Lichtenberg, *Principles of Plasma Discharges and Materials Processing*. (Wiley-Interscience, Hoboken, NJ, ed. Second, 2005).
13. K. Schoenbach, A. El-Habachi, W. Shi, and M. Ciocca, *Plasma Sources Science and Technology*, **6**, 468, 1997.

14. J. Seinfeld, and S. Pandis, *Atmospheric chemistry and physics*. (John Wiley and Sons, Inc., New York, 1998).
15. D. Song, I. Lenggoro, Y. Hayashi, K. Okuyama, and S. Kim, *Langmuir: The ACS Journal of Surfaces and Colloids*, **21**, 10375, 2005.
16. H. Tammet, *Journal of Aerosol Science*, **26**, 459, 1995.
17. B. Ku, and J. de la Mora, *Aerosol Science and Technology*, **43**, 241, 2009.
18. K. Iida, M. Stolzenburg, and P. McMurry, *Aerosol Science and Technology*, **43**, 81, 2009.
19. P. Horowitz, and W. Hill, *The Art of Electronics*. (Cambridge University Press, Cambridge, ed. Second, 1989).
20. L. Kiss, J. Söderlund, G. Niklasson, and C. Granqvist, *Nanostructured Materials*, **12**, 327, 1999.

Chapter 2: Radial Differential Mobility Analyzer for One Nanometer Particle Classification*

2.1. Introduction

Nanometer-sized aerosol particles are encountered extensively in research ranging from atmospheric science to nanotechnology. These particles form in the atmosphere through homogeneous nucleation of products of photochemical reactions. Originating as small clusters, these molecular-sized particles grow by condensation and coagulation. Nanoparticle synthesis in aerosol reactors proceeds similarly via homogenous nucleation and subsequent growth. For these and numerous other applications, measurements of the particle size distribution provide important insights into the growth dynamics of the aerosol. Furthermore, the ability to measure the size of nanomaterials is critical for applications in nanotechnology because optical, electrical, and magnetic properties at the nanoscale are size dependent.

The preferred instrument for measuring submicron aerosol particle size has been the differential mobility analyzer (DMA).[1-3] This instrument classifies charged particles according to their electrophoretic migration velocity in an electric field applied across a laminar, particle-free sheath flow, usually in the channel between coaxial cylindrical electrodes (cylindrical DMA). Charged particles are transmitted when their

* "Aerosol Science & Technology: Radial Differential Mobility Analyzer for One Nanometer Particle Classification," (42):53-59. 2009. Mount Laurel, NJ. Reprinted with permission."

migration velocity is near a value determined by instrument design as well as sheath flow rate, Q_{sh} . The ratio of the migration velocity, v_m , to the applied electric field, E , is called the particle mobility, Z_p , which is an inverse function of particle mobility diameter, D_p . This dependency implies that the smaller a charged particle is, the larger is its mobility and, thus, a smaller electric field will be required to reach the transmitted migration velocity of a given instrument ($v_m = Z_p E$). Particles with a particular Z_p will be maximally transmitted by properly setting E or, equivalently, the voltage V applied across the instrument electrodes.

Inherently, DMAs can resolve small differences in particle mobility. When diffusion is not important, the best attainable mobility resolution depends on the ratio of the volumetric flow rate of the sheath gas to that of the aerosol, Q_{sh}/Q_a . [4-5] This resolution is degraded by Brownian diffusion, which becomes important when the electrostatic potential energy of the migrating particle is small compared to its thermal energy. In this diffusion-limited regime, the theoretical resolution scales with $V^{1/2}$, which limits resolution for small particles.

To achieve high resolution classification of small particles requires making the residence time in the classification region small or correspondingly making the transmitted v_m large. When this condition is met, a high mobility particle (small particle size) can be classified at a high applied voltage. A short classification region is a straightforward way to reduce particle residence time. [6-7] Further improvements can be achieved by combining a short column with a large sheath flow rate. [8-10]

In contrast to the cylindrical DMA, Zhang et al. [11] and Fissan et al. [12] demonstrated a radial DMA (RDMA) design, where the sheath gas flows radially inward

between two flat electrodes (disks). The aerosol was introduced near the edge of the “primary” electrode and the charged particles were allowed to migrate toward the “counter” electrode in a uniform electric field. The combined flow was subsequently split unevenly between two outflow ports in the center of the electrodes. A small flow (classified flow, Q_s) was directed through the counterelectrode (across from the aerosol inlet annular slot) for further transmission to a particle detector; the remaining flow (excess flow, Q_e) exited through the center of the primary electrode. The initial RDMA was capable of classifying particles larger than 5 nm in diameter. In order to detect smaller particles, the migration velocity of those particles that are transmitted through the classifier must be increased. However, unlike in the cylindrical DMA design, the particle migration velocity of the original radial DMA design cannot be arbitrarily increased by increasing the sheath gas flow rate. A larger sheath flow leads to a correspondingly larger excess flow, which may cause turbulence in the excess outlet port. Turbulence generally degrades the resolution of the instrument and must be avoided. Alternatively, a reduction in particle residence time can be accomplished by using a smaller sizing region, and this approach was chosen for the new RDMA design.

In this section, the details are reported on the design, construction, and calibration of a RDMA, capable of classifying particles with sizes between 1 and 13 nm. As compared to the earlier RDMA design, the modified version reduces the residence time, first, by decreasing the distance between the aerosol inlet and sampling outlet, and second, by modestly increasing the sheath flow rate, while still avoiding turbulence. Instrument calibration is performed by employing gas ions as monodisperse particles in the 1 to 2 nm size range.

2.2. Experimental Method

2.2.1. Instrument Design

The goal of this work was to design an RDMA capable of nanoparticle classification down to one nanometer for use as an *in situ* diagnostic in nanoparticle synthesis reactors.[13] De la Mora and co-workers[7, 9-10] have demonstrated high resolution sizing in the one nanometer range by operating a short-column cylindrical DMA at very high flow rates (i.e., 500–2200 L min⁻¹). Such operation is impractical when instrument portability or power consumption is important or when the sheath gas must be of high purity to avoid trace impurity contamination. In such applications, the instrument must operate at a low sheath flow rate (~10 L min⁻¹).

In an RDMA, the mobility of particles transmitted with the highest efficiency is given by[11]

$$Z^* = \frac{Q_{sh} + Q_e}{2\pi(R_i^2 - R_o^2)} \frac{b}{V} = \frac{Q_{sh} + Q_e}{2\pi(R_i^2 - R_o^2)} \frac{1}{E}, \quad (2.1)$$

where R_i is the radius of the aerosol inlet to the classifying region, R_o is the radius of the sampled flow outlet port, b is the spacing between the electrodes, and V is the applied voltage. As in the original RDMA, R_o is set equal to 2.4 mm to match the inner diameter of 1/4" tubing, and an electrode spacing $b = 10$ mm is selected so that the device can operate up to $V = 10$ kV, while avoiding electrostatic breakdown when classifying the largest (lowest mobility) particles.

We are concerned with classification of particles in the free molecular limit, for which the electrical mobility of a singly charged particle is

$$Z_p = 0.441 \frac{q(kT/m)^{0.5}}{pD_p^2}, \quad (2.2)$$

where q is the elementary unit charge ($1.602 * 10^{-19}$ coulombs), k is the Boltzmann constant, T is the temperature, m is the mass of the gas molecules, p is the gas pressure, and D_p is the particle mobility diameter. Equation (2.2) is a free-molecular expression that describes well the correlation between diameter and particle mobility for the size range of interest in this study, but deviates from the transition regime expression for particle mobility by 4.6% for a mobility diameter of 10 nm. By combining equations (2.1) and (2.2), we find that RDMA classification of 1 nm particles requires an entrance radius of $R_i \approx 7.5$ mm when the sheath flow rate is $Q_{sh} = 10 \text{ L min}^{-1}$ and the operating voltage is $V = 60 \text{ V}$. Due to the reduced volume of the classifying region, the nano-RDMA should be more sensitive to electric field nonuniformities than the earlier design and require experimental characterization of the instrument.

While similar to the original RDMA,[11] the new design (termed “nano-RDMA” in the discussion that follows) incorporates several key changes. The first and most significant difference is the radius (labeled R_i in figure 2.1) of the circular slit where the aerosol is introduced that has been reduced from 50 to 7.5 mm. Second, the RDMA[11] achieved a resolution in the high voltage limit that was lower than that predicted for non-diffusive particles. It was later found (unpublished) that this was due to a combination of (1) imperfect concentricity between the knife edge and the inner surface that forms the annular aerosol entrance slot, and (2) a less-than-ideal pressure drop through that slot. In the present design, mounting of the knife-edge ring has been modified to ensure concentricity, while permitting adjustment of the aerosol inlet gap height with high precision. The knife edge (labeled in figure 2.2) and inner electrode are machined from

304 stainless steel (SS) to have a slip-fit tolerance on the radius, thereby ensuring concentricity and eliminating any gap through which the aerosol can leak. Precision shims were used to set and optimize the aerosol inlet gap. A shim thickness of 0.44 mm was found to give a minimum in the line width of the ion mobility distribution. Smaller gaps resulted in loss of signal that was attributed to diffusion losses in the inlet gap.

As in the original RDMA design, the aerosol is introduced tangentially into a continuous annular channel (so-called racetrack) between the pieces defining the inlet. A high voltage bias is applied to the aerosol entrance electrode; electrical contact is made through a screw (not shown), which is inserted through the top plate. Opposite this biased electrode is the counterelectrode that is grounded through a Swagelok union. The classified aerosol exits through a port in the center of the counter electrode.

The remaining pieces were made of white Delrin (except as noted). These include the outer shell, the top plate, the sheath gas inlet, the conical excess outlet, the inlet extension (not pictured) and a sheath gas distributor (made of porous polyethylene sheet with an average pore diameter of 25 μm). These pieces are scaled versions of parts from the original design with two exceptions:

- (1) The conical excess outlet was designed to fit inside the inner electrode from the top rather than being press fit from the bottom, as in the original RDMA. This piece is made of Delrin (dielectric). Computational fluid dynamics simulations performed using COMSOL Multiphysics indicated that the dielectric surface distorts the uniformity of the electric field within the classifying region. Field distortion was avoided by affixing a thin, metallic wire mesh to the bottom of the conical port, in electrical contact with the inner electrode. Operation of the RDMA with the conductive mesh yielded

higher particle transmission efficiency than observed in preliminary experiments without the mesh, thus confirming the simulation prediction. All data presented herein were obtained with the mesh in place.

(2) In the first design of the nano-RDMA, the aerosol was introduced directly into the racetrack through a grounded Swagelok fitting attached to the outer shell. The strong electric field, produced between this fitting and the biased upper electrode, caused particle loss to walls before entering the classification region.[14] To avoid this problem, the Swagelok fitting was moved away from the top electrode by incorporating a 20 mm long Delrin tube. The additional inlet length is expected to result in particle loss to the walls by diffusion. Two alternative approaches were also considered. First, the inlet tubing could be biased to the same potential as the upper electrode. For safety reasons, this option was not implemented. The second alternative was to maintain the upper electrode at ground potential and to bias the bottom electrode. This approach runs into the same issue it was attempting to fix and is less desirable since particle loss would occur in a section where the particles have already been classified.

2.2.2. Instrument Calibration

The performance of the new RDMA design was evaluated by using molecular ions (tetra-alkyl ammonium halides) based on the work and reported mobilities of Ude and de la Mora.[15] The molecular ions were produced by electrospraying solutions of the analyte species. The liquid delivery apparatus consisted of an Erlenmeyer flask (125 mL) fitted with a stopper through which two pieces of plastic tubing were inserted as depicted in figure 2.3. One tube was connected to a regulated air supply with fine pressure control (± 0.1 psi). The other tube was immersed into the liquid and was

connected to a stainless-steel capillary tube (O. D. \approx 1.6 mm and I. D. 127 μ m) that served as the electrospray nozzle. The nozzle was biased to 3.5 kV with respect to a fitting (cross) into which the capillary tube was inserted, through a threaded Delrin rod for electric isolation. Equal nitrogen flows (0.6 L min⁻¹ total flow) introduced through the side arms of the cross carry the electrosprayed ions through the outlet port. The electrospray nozzle and aerosol outlet were positioned vertically to prevent dripping that might cause an electrical short.

The calibration standards were ions of tetra-alkyl ammonium salts (tetra-propyl ammonium iodide (TPropylAI), tetra-butyl ammonium iodide (TButylAI) and tetra-heptyl ammonium bromide (THeptylAB)). Solutions were prepared that contained 0.47, 0.27 and 0.20 mmol L⁻¹ of these analytes, respectively, in 1-propanol (Sigma Aldrich, St. Louis, MO, 99.7% purity); the analyte concentrations are one-hundredth of those used in the work of Ude and de la Mora.[15] The substantial dilution ensured that mostly monomeric tetra-alkyl ammonium ions (R_4N^+ , M^+) and “dimers” ($(R_4NX)R_4N^+$, M_2X^+) were produced, thereby allowing unambiguous peak assignment without the need for coupling the RDMA to a mass spectrometer. Additional solutions with tetra-ethyl ammonium iodide (TEthylAI), tetra-pentyl ammonium bromide (TPentylAB) and tetra-hexyl ammonium bromide (THexylAB) in 1-propanol at concentrations of 0.20 mmol/L were employed to produce ions with similar mobilities. For TEthylAI (as well as tetra-methyl ammonium iodide), the crystals did not dissolve completely in 1-propanol and the actual dissolved concentration was unknown. The mobilities of the latter three salts have not been previously measured by DMA.

A sheath flow rate of 10 L min^{-1} was chosen for the calibration experiments. The combined sheath flow and aerosol inlet flow are split so that the excess flow rate is 10 L min^{-1} and the sampled flow rate is 0.6 L min^{-1} (i.e., $Q_{sh} = Q_e$ and $Q_a = Q_s$). While the choice of aerosol flow rate was fixed to mimic the operating conditions of a nanoparticle synthesis reactor, the sheath flow rate of 10 L min^{-1} was found to produce the narrowest distributions of the molecular ions. The device should be capable of operating at higher aerosol flow rates, but additional optimization of the aerosol inlet gap might be necessary.

Molecular ion concentration was calculated from the current output of a home-made faraday cup electrometer as a function of voltage applied to RDMA electrodes. A computer with a 16-bit analog output channel was used to remotely program the voltage output of a 10 kV power supply (Acopian model P010HD3). The RDMA was operated in stepping mode, which consisted of applying a fixed voltage and waiting 5 s at each voltage before the recording the average current over a 1 s measurement interval. While shorter waiting times (as short as 2 s) produced similar distributions, all measurements were done at 5 s waiting times to ensure steady state operation.

2.2.3. Instrument Coupling with Mass Spectrometer (in Collaboration)

The identity of the electrosprayed molecular ions was confirmed by affixing the nano-RDMA to the entrance of a mass spectrometer, as shown in figure 2.4. The components were assembled in series in the following order: electrospray source, nano-RDMA (second version), and Mass Spectrometer (Finnigan LCQ Deca Ion Trap Mass Spectrometer (LCQ-MS)). The electrospray source was the same used for calibration measurements and is more completely described in appendix I. The molecular ions

measured in this arrangement were TPropylAI, TButylAI, TPentylAI, THexylAB, THeptylAB, and tetra octyl ammonium bromide (TOctylAB).

The electrospray source was connected to the nano-RDMA using standard Swagelok fittings. The nano-RDMA was positioned in front of the LCQ-MS using a breadboard plate (150 mm x 150 mm) made for mounting optical elements, a pair of custom-built plates, and optic mounting posts (O. D. \approx 12 mm). The assembly aligned the sample outlet of the nano-RDMA with the atmospheric pressure inlet (API) of the LCQ-MS. Due to the ports on the nano-RDMA and the construction of the LCQ-MS, the sample outlet of the nano-RDMA and the API of the LCQ-MS were separated by a distance of 25 mm. The gap was reduced to less than 1 mm by attaching a Swagelok (1/4") to tube stub (1/8") fitting on the nano-RDMA outlet.

The nano-RDMA is operated with a 10 L min^{-1} sheath flow rate of nitrogen and in voltage stepping mode. The voltage on the DMA is provided from a high voltage power supply (Ultravolt 2 kV supply) that is controlled externally with a Labview program. The program set the voltage and then kept it constant for a 30-second interval, repeating this process for a fixed interval of voltages. The Labview program was started at the same time that a time-based scan in the MS software was started that had a duration long enough to ensure data would be collected over the complete voltage scan. The data were analyzed using a MatLab program that averaged the signal produced by the molecular ions over the 30-second interval that the voltage was held constant.

2.2.4. Instrument Comparison to Other DMAs (in Collaboration)

The performance in terms of transmission and resolution of the nano-RDMA was compared to the nano-DMA (cylindrical DMA designed for measuring nanoparticles in

the 1–30 nm range) and the original RDMA (radial DMA designed for measuring nanoparticles in the 10–100 nm range). Four different monomers were measured in this study: tetra methyl ammonium iodide (TMAI), TPropylAI, THeptylAB, and tetra dodecyl ammonium iodide (TDodecAI).

The setup consisted of an electrospray source followed by a tandem DMA arrangement with two commercially available electrometers used as the detectors, as shown in figure 2.5. The electrospray source was similar to that described previously with the exception that the capillary was fused silica and the high voltage bias was provided through the solution. The first instrument was a high-resolution DMA (HR-DMA)[9] operating with a high sheath flow rate whose voltage was fixed at the peak of the monomer mobility distribution. The sampled outlet flow from the first DMA was split into two with one stream directed toward an electrometer for upstream concentration measurements and the other stream directed to the inlet of the second ‘test’ DMA.

The second DMA was operated in voltage stepping mode using recirculating sheath flow rates of 6 (data not shown), 10, and 15 L min⁻¹ (data not shown). The aerosol flow rate was 0.6, 1, and 1.5 L min⁻¹, respectively. These flow rates were selected to maintain the aerosol to sheath flow rate ratio of 1:10, as is typical for aerosol measurements. The highest sheath flow rate tested was limited to 15 L min⁻¹ as higher flow rates resulted in turbulence in the nano-RDMA. After collecting the mobility distributions for each ion, the signal from the second electrometer was normalized by that of the first electrometer to determine the particle transmission. The resolution was determined in the same way as in the calibration section.

2.3. Results

2.3.1. Calibration

From equation (2.1), the product $Z_p * V$ is observed to depend on the DMA geometry and sheath flow rate. Based on this equation, the theoretical $v_m * b$ was calculated to be $109.8 \text{ cm}^2 \text{ s}^{-1}$. Fitting the concentration distributions of the monomers and dimers for the previously reported salts, the experimental value was found to be $125.61 \pm 0.93 \text{ cm}^2 \text{ s}^{-1}$. Using this value, each voltage is converted to an inverse mobility ($1/Z_p$) and the distribution for each tetra-alkyl ammonium salt ion is shown in figure 2.6. The mobility distributions for the monomer and dimer are fitted well with two separate Gaussian distributions. As shown in figure 2.7, the measured mean inverse mobilities match the previously reported values over the entire range.

The experimental value for $Z_p * V$ is 14.4% higher than theoretical estimate based on equation (2.1). The difference is partially due to non-uniformities in the electric field that were not taken into account in the derivation of equation (2.1), which therefore requires a higher voltage to classify ions of a known Z_p . The deviation occurs as the ions migrate toward the axis of the device. Here, the holes in the electrodes for the excess and sample flow outlet ports decrease the effective field ($E = V/b$). Although the excess flow outlet port is covered with a SS mesh, the field is nonetheless decreased. Also, the model assumes a radial source for the aerosol. In the actual device, the aerosol enters the classification region through a finite gap in the upper electrode between the knife edge (a) and the inner electrode (b), thus introducing uncertainty in the estimation of the radial distance. This is particularly problematic for the nano-RDMA since the gap is comparable in size to the radial distance to the knife edge. Hence, the mobility of the

particles transmitted through the nano-RDMA is estimated using an empirical calibration factor, i.e.,

$$Z^* = \frac{Q_{sh} + Q_e}{2\pi(R_i^2 - R_e^2)} \frac{b}{V} \frac{1}{f_{mob}}, \quad (2.3)$$

where $f_{mob} = 0.874 \pm 0.009$.

As with the previous salt solutions, DMA scans of electrosprayed solutions of TEthylAI, TPentylAB and THexylAB revealed new peaks in the mobility spectra with reasonable inverse mobility values, plotted in figure 2.8. The measured inverse mobility distributions of these compounds are presented in figure 2.7. As before, each individual peak was fit with a Gaussian distribution. The mean inverse mobility found for each ion is listed in table 2.1 along with the values for the calibration standards.

2.3.2. Results: Mass Spectrometry

The mobility distribution recorded with the LCQ-MS for the monomer of each molecular ion is presented in figure 2.9. The molecular ion was detected at approximately the same voltage reported previously when a Faraday cup electrometer was used as the detection, confirming the identity of the molecule detected. The spectra are plotted with error bars corresponding to the standard error of the signal, demonstrating that a 30-second interval produces a stable signal.

An extended voltage scan was captured to confirm the identity of the dimer and trimer peak for THEptylAB, as shown in figure 2.10. The mass spectrum for the monomer peak consisted of a single mass at a molecular weight of 410. The region corresponding to the dimer region consisted of three different species: monomer, dimer, and doubly charged quadramer. The monomer is most likely due to transmission through

the nano-RDMA of the dimer followed by fragmentation upon reaching the API of the LCQ-MS, but this has not been proved. Detection of the doubly charged quadramer is not unexpected as it should have the same mobility as the singly charged dimer. The third peak in the distribution consisted of more molecular weights than the first, including the monomer, dimer, trimer, and quadramer, indicating that this peak is not due to a monomobile species.

2.3.3. Results: DMA Comparison

A plot of the normalized mobility spectra for the molecular ions analyzed with the nano-RDMA and the nano-DMA as the “test” DMA are presented in figure 2.11. The mobility spectra for the salts with the three largest monomers were narrow, single modal distributions. Comparing the nano-RDMA and the nano-DMA data, the transmission was observed to be approximately a factor of three and five higher (not shown) for the nano-RDMA compared to the nano-DMA and RDMA, respectively. Interestingly, the mobility spectra for the TMAI monomer contained three separate peaks, as shown in figure 2.12. Three separate peaks were not observed in the mobility spectra using the other DMAs. It was determined that the second and third peak were due to methanol (or an impurity in the methanol solvent) clusters that transmitted the HR-DMA[9] in a multiply charged state and discharged one and two electrons, producing less mobile species. The presence of three peaks in the mobility spectra for the TMAI molecular ion made the data unsuitable for transmission analysis.

2.4. Discussion

2.4.1. Calibration

An important figure of merit for size measurements is the instrument mobility resolution, which is defined as the ratio of the mean particle mobility over the full width at half maximum of the mobility distribution:[5]

$$\mathfrak{R} = \frac{Z_p}{\Delta Z_{p,FWHM}} . \quad (2.4)$$

In the non-diffusive limit, the theoretical resolution equals $\mathfrak{R}_{nondiff} = Q_{sh}/Q_a$, which corresponds to a value of 16.7 ($Q_{sh}/Q_a = 10/0.6$) for the conditions used in this experiment. When the ratio eV/kT is small, Brownian diffusion degrades the resolution, which becomes proportional to $V^{1/2}$. Flagan[5] showed that the resolving power of an ideal DMA operated in the diffusive limit is

$$\mathfrak{R}_{diff} = 0.425 \left[\frac{Pe_{mig}}{G_{mig}} \right]^{\frac{1}{2}} , \quad (2.5)$$

where, for the RDMA, $Pe_{mig} = eVf_{mob}/kT$. The factor, G_{mig} , depends upon the sheath and aerosol flow rate as well as the particulars of the DMA geometry and the assumed gas flow profile. The non-diffusive and diffusive resolution limits can be combined to compare with the measured resolutions,[7] according to the following equation:

$$\mathfrak{R}_{Exp} = \sqrt{\left(\frac{1}{R_{nondiff}^2} + \frac{1}{R_{diff}^2} \right)^{-1}} . \quad (2.6)$$

Measurements made using monomobility ions enables direct determination of the mobility resolution from the widths of the mobility peaks seen in figures 2.6 and 2.8. Experimentally, the instrument resolution was calculated for each molecular ion

monomer and dimer from the mobility distribution fits found previously and plotted in figure 2.13. Over the range of voltages used, the resolution of the monomeric molecular ion (M^+) is found to increase with voltage with approximately the same slope as that predicted in the diffusive (high mobility/small particle) limit. The observed resolution is clearly smaller than predicted when assuming uniform parallel flow and uniform electrical fields. Empirically for the nano-RDMA, we find $G_{mig} = 17.3 \pm 1.1$; this deviates from the simplistic model estimate of $G_{mig} = 10.5$. One possible explanation for the observed resolution being lower than theoretically predicted is the possibility of a recirculation bubble near the stagnation point on the axis of the instrument.[16] Regardless of the cause of deviation, the nano-RDMA is observed to operate in the diffusive limit for the range of mobilities of the molecular ions measured in this study. Yet, the instrument clearly demonstrates resolving ability for particle mobilities that were not even measurable with the original RDMA.

For the dimer molecular ions ($(MX)M^+$), the measured resolution falls below that of the monomer ions, but they appear to follow the same $V^{1/2}$ power law. The data preclude the possibility that the resolution begins to degrade as the voltage increases since the THeptyLAB monomer resolution follows the $V^{1/2}$ trend of the monomers and is measured at nearly the same voltage as the TPropylAI dimer. While not rigorously tested, the observed difference in the trends of the resolution for the monomers and the dimers could be due to the non-spherical nature of the dimer. As observed for significantly larger particles[17] classified at low voltages (i.e., <2000 V), the dimers tend to migrate through the DMA with an orientation that approaches random. Since the

orientation of the dimer can affect the drag force, the dimers will be transmitted over a broader range of voltages leading to a lower effective mobility.

The results presented above have been discussed in terms of inverse mobility, but this quantity is hard to visualize. The real-space analog of inverse mobility is diameter. In the free-molecular limit, the mobility diameter is larger than the physical particle diameter by 0.3 to 0.4 nm.[18] The observed difference between the two diameters corresponds to the radius of the background gas molecules. In terms of mobility diameter, particle sizes as small as 1.03 nm (TEthylAI monomer ion) were sized with a standard geometric deviation (σ_g) of 1.05 (Resolution of ~ 4.7). Resolution increased with diameter reaching a value of ~ 7 at 1.47 nm (monomer ion of THeptyLAB), which corresponds to a σ_g of 1.035. In other words, this instrument can differentiate a particle with a diameter of 1.0 nm from a particle with a diameter 1.1 nm. More importantly, this instrument has the necessary resolving power to distinguish growth by vapor deposition from that by coagulation down to a mobility diameter of 1 nm, since the experimentally observed σ_g is much smaller than the self-preserving distribution value of about 1.3 associated with coagulation. Beyond measuring the size of molecular ions, the instrument can be utilized for larger ions. Based upon the empirical calibration constant determined from measuring molecular ions, the upper size limit for the sheath flow rate investigated here is calculated to be 13 nm. To characterize the instrument response for particles larger than 1.8 nm will require additional measurements using the tandem DMA technique or larger molecular ions.

2.4.2. Mass Spectrometry

The mass spectrometer confirmed the molecular weight of the electrosprayed monomers unambiguously. The instrument resolution could be calculated from the mobility spectra to be a value of 7 for the THeptylAB monomer. This is similar but slightly lower than what was observed when detecting the ions with a faraday cup electrometer. The exact origin of the difference was not determined, but it could be related to the introduction of the ions through the API. The resolution could be readily changed through adjusting the aerosol flow, as expected. This adjustment could be valuable in cases where slightly higher resolution is needed. Yet, the flow rate adjustment has an impact on the transmission to the LCQ-MS, and the standard error of the distribution increases.

The mass measurements provided significant information about the dimer peak. A significant fraction of the total signal from the dimer peak is observed at the molecular weight of the monomer. Detection of the monomer is most likely a by-product of dimer fragmentation upon entering the API of the LCQ-MS. In addition to the monomer and dimer, the doubly charged quadramer was detected in the second peak. The presence of the quadramer could be partially responsible for the lower resolution of the dimer peak reported for the instrument calibration.

The mass analysis of the third peak in the mobility spectrum confirmed previous expectations that the third peak in the mobility distribution was not due to a single species. This peak is most likely a multiply charged species containing several of the molecular ions that evaporates upon entering the API of the LCQ-MS and therefore is not appropriate for determining the resolution.

2.4.3. DMA Comparison

The tandem DMA experiments provided important information about the transmission and resolution of the nano-RDMA in comparison to other similar devices. The transmission increased with molecular ion size since fewer particles are lost to diffusion as the particle size increase. The measured transmission was higher than the other devices tested, but could be improved with a better design of the aerosol inlet extension (simulations discussed in chapter 3). Still, the higher transmission of the nano-RDMA offers the ability to detect lower particle concentrations that could be invaluable in field measurements. Also, having the transmission information permits a more accurate description of the concentration of unknown aerosol sources.

The resolution of the nano-RDMA was also higher than the other DMAs tested. The detection of multiple peaks in the TMAI mobility spectra addresses the importance of resolution in mobility measurements. The first DMA transmitted multiple species of different charge states. Without the higher resolution offered with the nano-RDMA (higher than the other DMAs compared), the transmission data would be improperly calculated. The multiply charged particles would produce a greater current in the first electrometer than singly charged particles would produce in the second electrometer.

2.5. Summary

We described a nano-RDMA that enables the classification of molecular ions with mobility diameters in the range of 1 to 1.8 nm. The instrument was calibrated using monomer ions. Non-uniformities in flow and electric field emanating from the very short classification region required empirical corrections to the predicted mobility response and resolution from which an upper limit for size measurement was calculated to be 13 nm.

While the nano-RDMA operates in the diffusive limit for these molecular ions, its resolving power is, nonetheless, substantial and should enable investigation of aerosol or nanoparticle growth dynamics at mobility diameters as small as 1 nm.

Coupling of the nano-RDMA with the LCQ-MS confirmed the identity of the molecular ions as well as provided information about the other peaks. The resolution of the monomer peak was slightly lower than that measured for the calibration. The dimer peak was found to contain a significant fraction of monomer and dimer molecular weights as well as a small amount of doubly charged quadramers. The heterogeneity of this peak could contribute to the lower-than-expected resolution for the dimer peak.

Comparing the nano-RDMA operation with similar DMAs showed that the transmission and resolution were higher for this device. The higher resolution proved valuable as the nano-RDMA was able to detect multiple peaks in the mobility spectra of TMAI. The high transmission and resolution demonstrated in these measurements will make the nano-RDMA an attractive option when selecting a mobility measuring device.

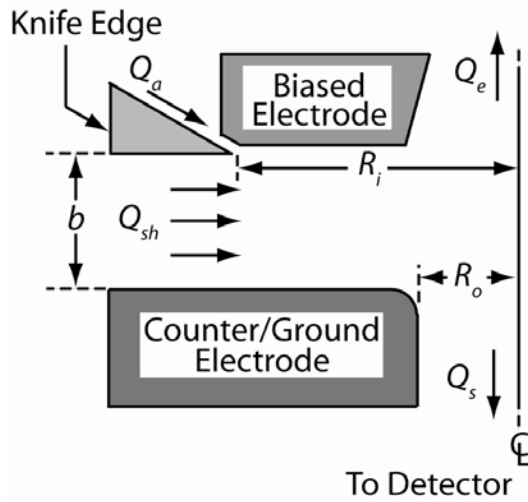


Figure 2.1. Simplified Schematic of RDMA Operation.

Simplified schematic of the nano-RDMA operation illustrating the direction of the sheath gas flow (Q_{sh}), the aerosol inlet (Q_a), the sampled outlet (Q_s), and the excess flow outlet (Q_e).

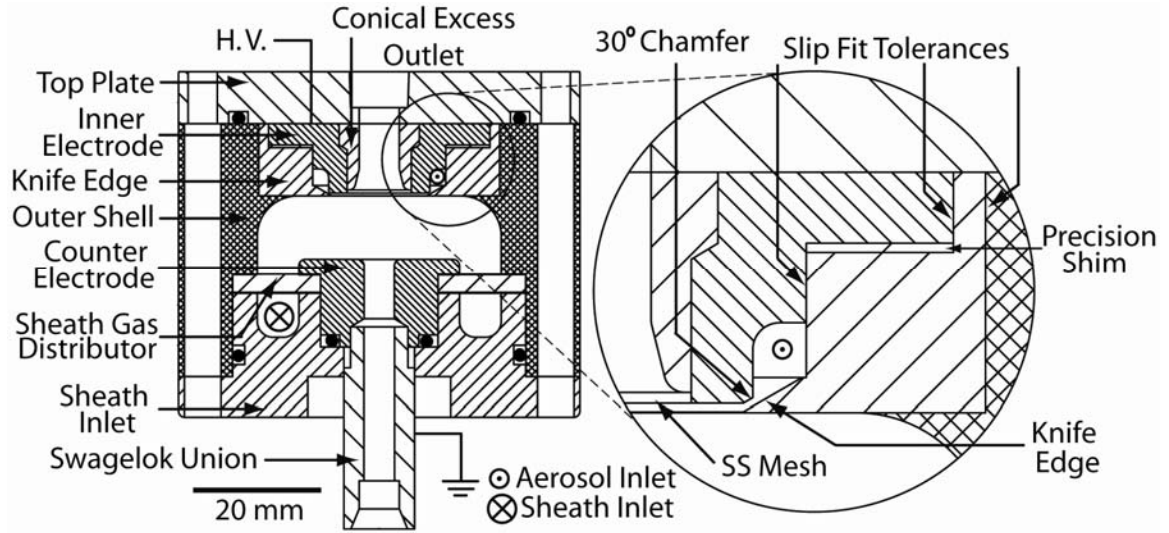


Figure 2.2. Detailed Schematic of the nano-RDMA.

Detailed schematic of the nano-RDMA. The materials used for construction are noted in the text. Filled circles represent O-Rings. The inset depicts the slip-fit tolerances and the knife edge in more detail as well as the location where precision shim disks are placed to create a gap between the chamfer and the knife edge through which the aerosol leaves the racetrack and enters the sizing portion of the device.

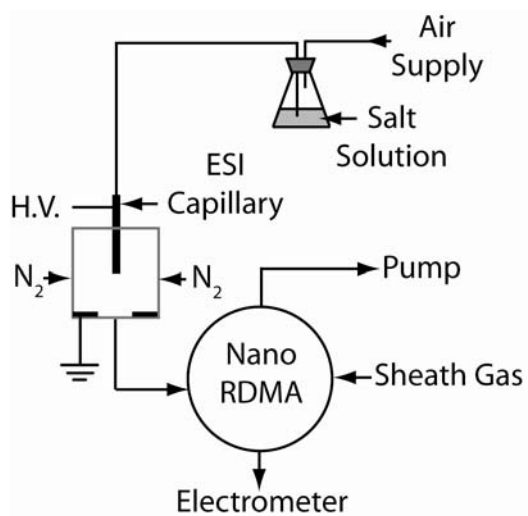


Figure 2.3. Schematic of Electro spray.

Schematic of electro spray and nano-RDMA combination used to measure molecular ions and determine the resolution of the nano-RDMA.

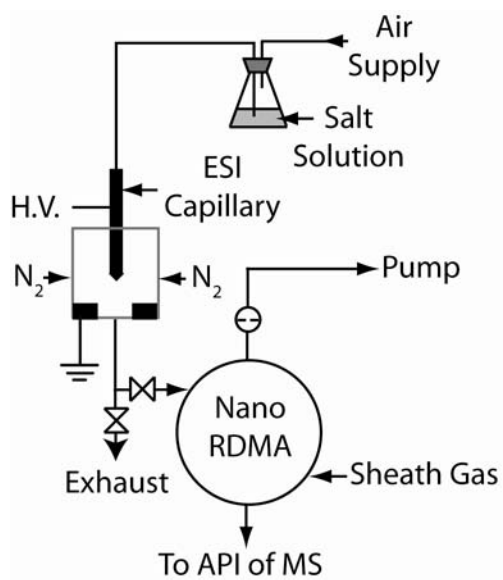


Figure 2.4. Schematic of nano-RDMA and Mass Spectrometer.

Schematic of the experimental set up used to measure the combined mobility and mass distribution.

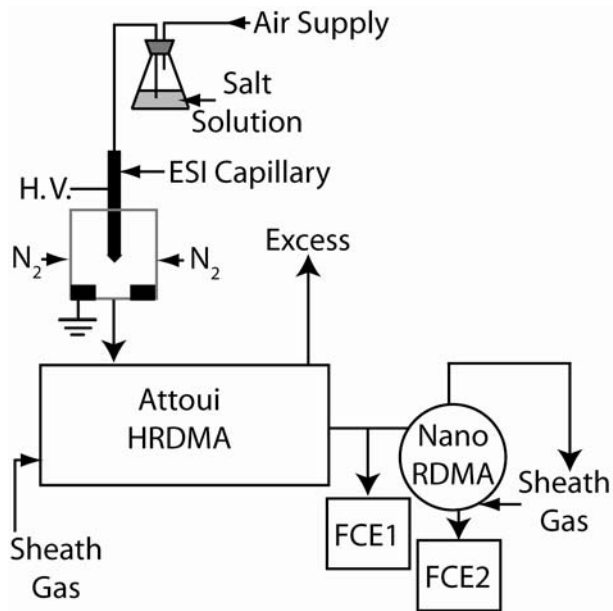


Figure 2.5. Schematic of TDMA.

Schematic of the tandem DMA arrangement used to determine transmission and resolution of the second DMA.

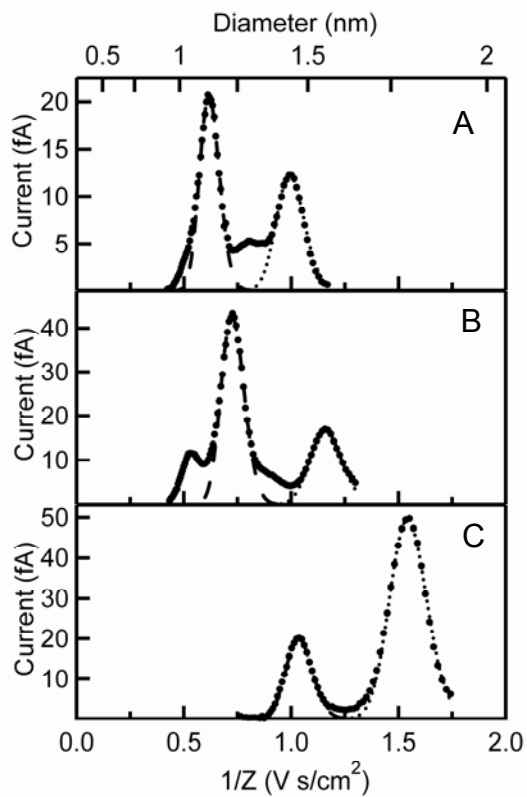


Figure 2.6. Inverse Mobility Distributions.

Inverse mobility distributions of (A) TPropylAI, (B) TButylAI, and (C) THeptylAB. The long dash curve fits the M^+ (i.e., R_4N^+) distribution and the short dash curve fits the M_2X^+ distribution. The mobility values plotted are scaled values.

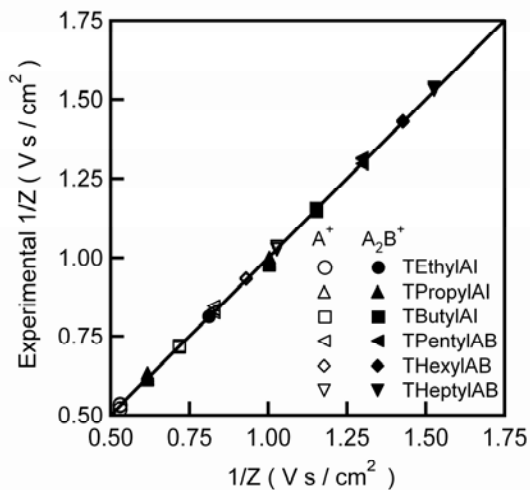


Figure 2.7. Geometric Mean Mobilities.

Compilation of the geometric mean mobilities obtained from fitting size distributions plotted versus the mobility found previously (Ude and de la Mora 2005). The empty symbols are for the monomer and the filled symbols are for the dimer.

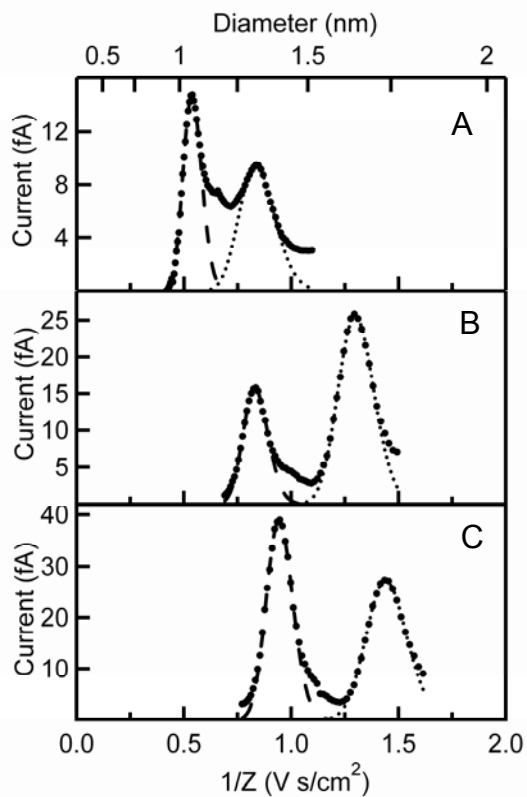


Figure 2.8. Inverse Mobility Distributions.

Inverse mobility distributions of (A) TEthylAI , (B) TPentylAB, and (C) THexylAB.

The long dash curve fits the M^+ (i.e., R_4N^+) distribution and the short dash curve fits the M_2X^+ distribution. The mobility values plotted are scaled values.

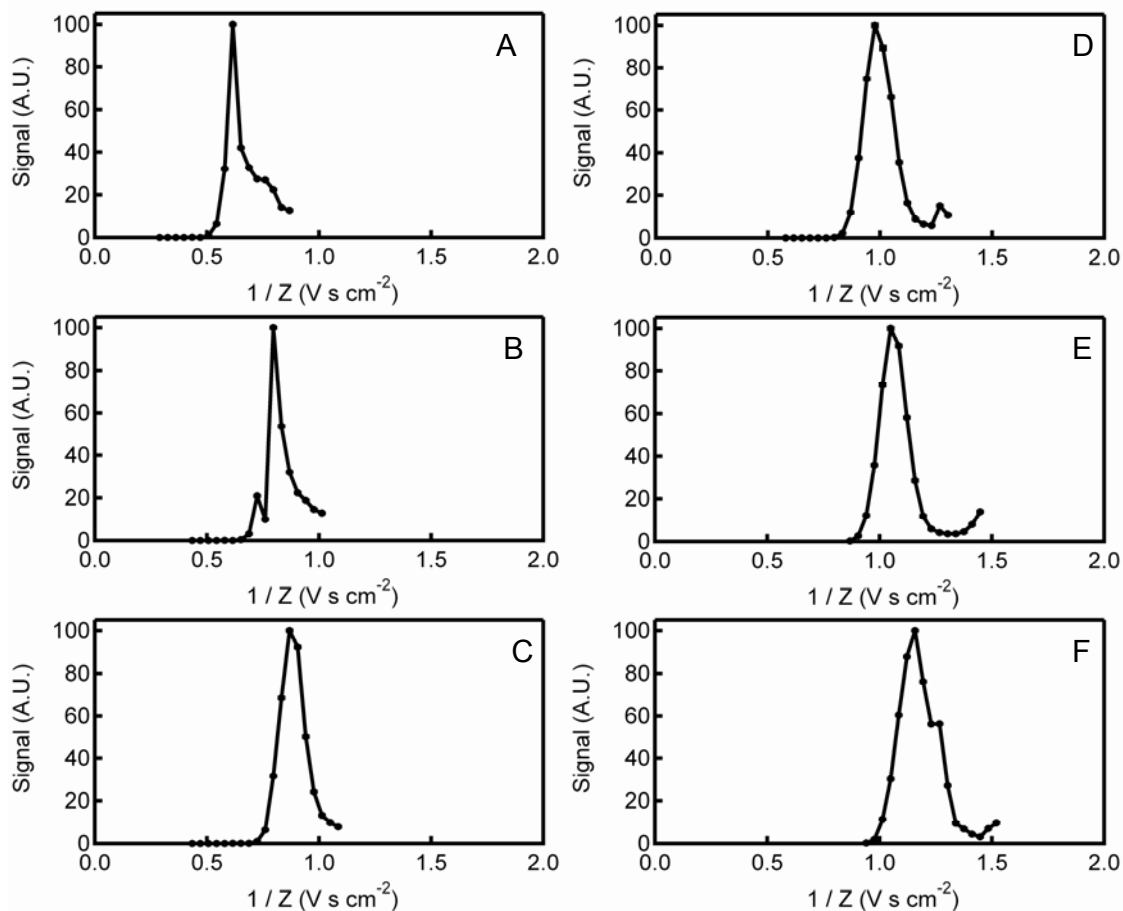


Figure 2.9. Inverse Mobility Distributions Using Mass Spectrometer as Detector.

Inverse mobility spectra recorded with the LCQ-MS for the monomer of (A) TPropylAI, (B) TButylAI, (C) TPentylAI, (D) THexylAB, (E) THeptylAB, and (F) TOctylAB.*

* The mobility spectra were recorded with a sheath flow rate of 11 L min⁻¹. The data have been corrected to account for the higher flow rate.

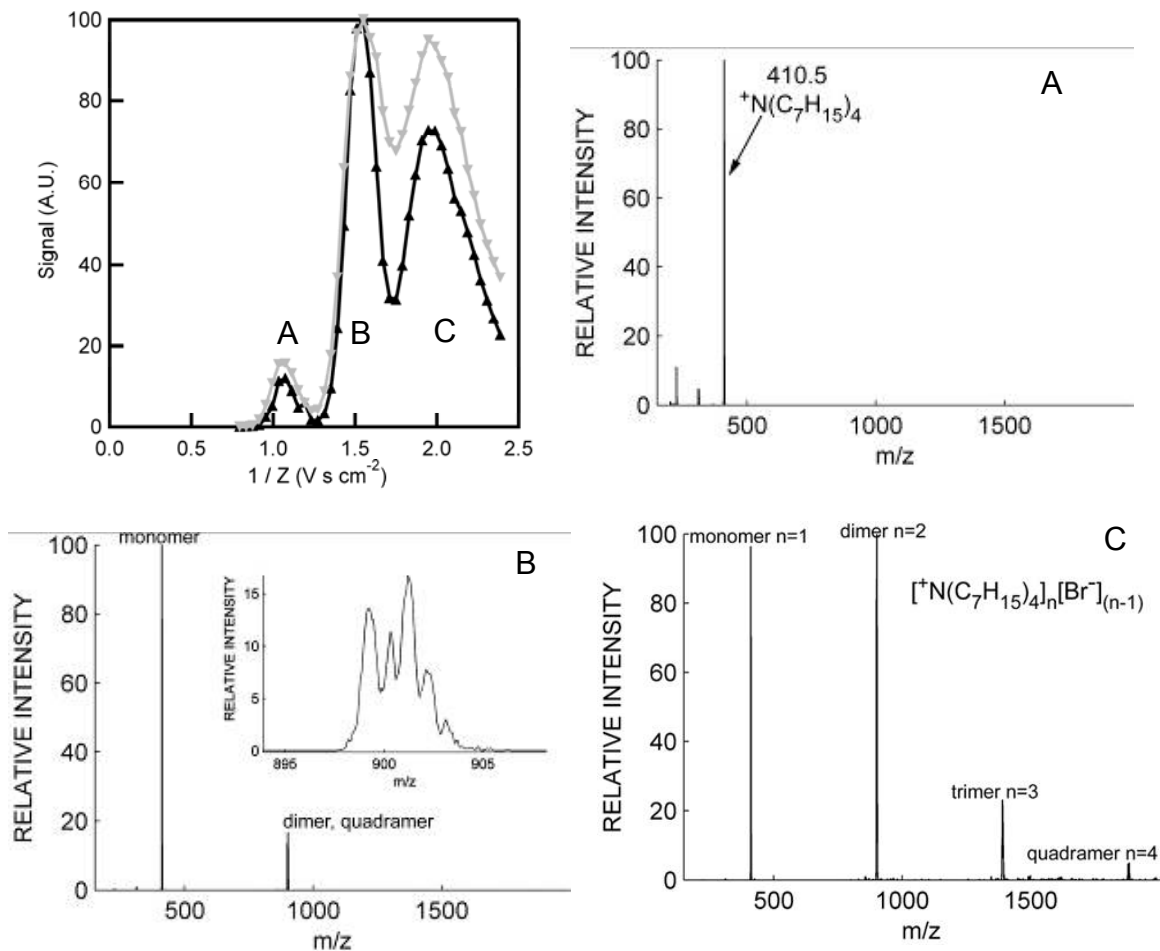


Figure 2.10. Mobility Distribution of Monomer and Dimer Using MS.

Extended mobility spectra capturing the monomer (A), the dimer (B), and a third peak (C) for the high resolution (black triangles up; $Q_a = 500$ sccm) and low resolution (gray triangles down; $Q_a = 1000$ sccm) cases. (A) The mass spectra for the monomer region of the mobility distribution. (B) The mass spectra for the dimer region of the mobility distribution with the inset depicting the presence of the doubly charged quadrumer. (C) The mass spectra for the third peak of the mobility distribution indicating the presence of trimer and quadrumer.

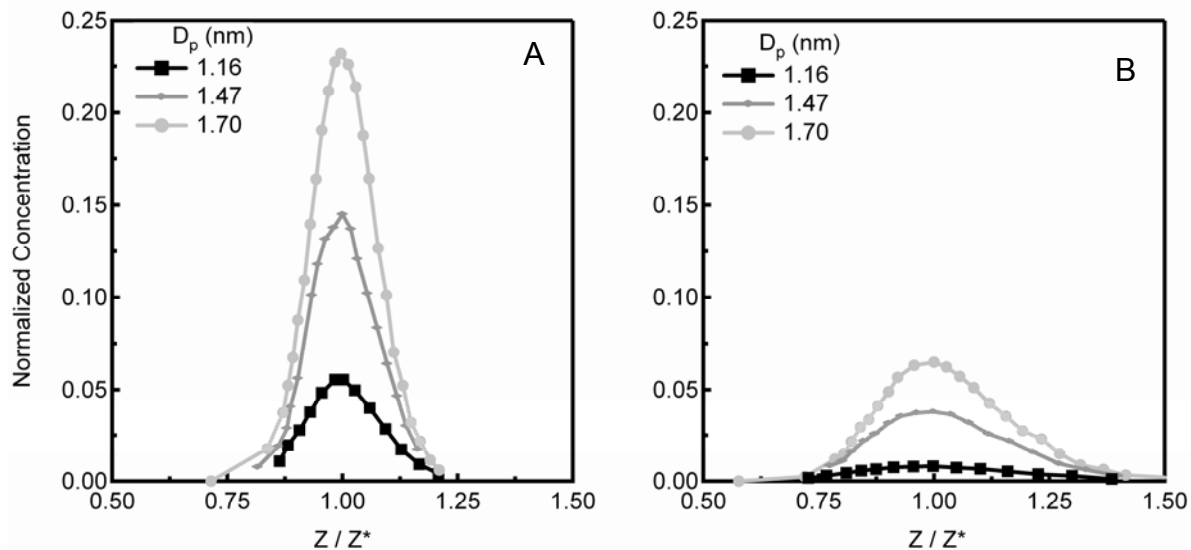


Figure 2.11. Mobility Distribution Comparison between nano-RDMA and nano-DMA.

(A) Normalized mobility spectra for molecular ions of different size measured with the nano-RDMA. (B) Normalized mobility spectra for molecular ions of different size measured with the commercial nano-DMA. The calibration standards are the molecular ions used previously: D_p of 1.16 nm is TPropylAI, 1.47 is THeptylAB, and 1.70 is TDodecylAI.

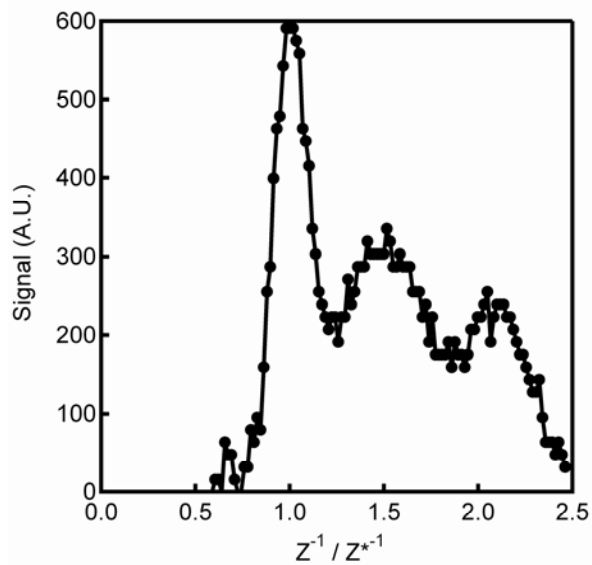


Figure 2.12. Mobility Distribution of TMAI.

Mobility spectra recorded with the nano-RDMA of a stream containing TMAI that is size selected with a HR-DMA. The first peak is due to the molecular ion TMAI whereas the second and third peaks have been determined to be due to either methanol clusters or impurities in the methanol.

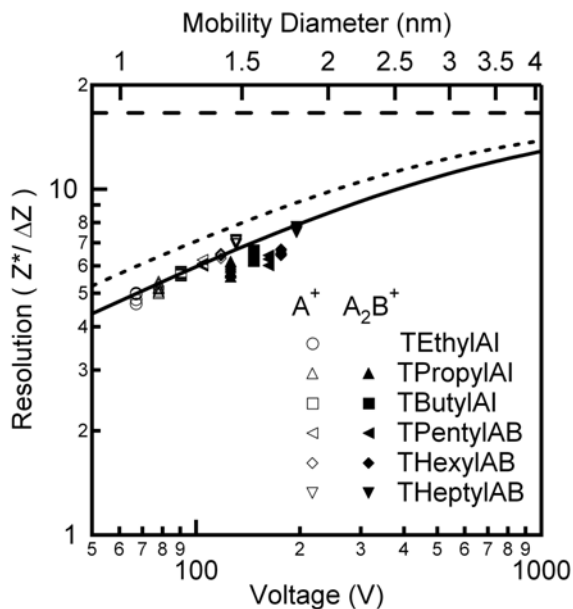


Figure 2.13. nano-RDMA Resolution.

Comparison of the theoretically calculated and experimentally measured resolution. The empty symbols correspond to the monomer whereas the filled symbols are for the dimer. The solid line corresponds to the fit of the experimental data while the dashed lines are the calculated theoretical limits in the diffusion regime (short dash) and in the absence of the effects of diffusion.

Table 2.1. Mobility Data.

Previously determined and experimentally measured inverse mobilities for each of the different tetra-alkyl ammonium salts as well as the calculated resolution. The values listed under the heading M^+ corresponds to monomers for the appropriate molecular ion whereas the values listed under $(MX)M^+$ correspond to the dimers.

| Molecular Ion | Previous $1/Z^*$ ($\text{cm}^2/\text{V s}$) | Mean V (V) | Mean $1/Z$ ($\text{cm}^2/\text{V s}$) | Standard Deviation ($\text{cm}^2/\text{V s}$) | Mean Resolution | Standard Deviation |
|---------------|--|-----------------|--|--|-----------------|--------------------|
| M^+ | | | | | | |
| TEthylAI | - | 66.6 | 0.531 | 0.007 | 4.88 | 0.15 |
| TPropylAI | 0.619 | 77.8 | 0.619 | 0.007 | 5.18 | 0.14 |
| TButylAI | 0.718 | 90.5 | 0.721 | 0.002 | 5.70 | 0.06 |
| TPentylAB | - | 105.1 | 0.837 | 0.006 | 6.07 | 0.09 |
| THexylAB | - | 117.7 | 0.937 | 0.001 | 6.42 | 0.06 |
| THeptylAB | 1.030 | 129.6 | 1.032 | 0.004 | 7.02 | 0.08 |
| $(MX)M^+$ | | | | | | |
| TEthylAI | - | 102.7 | 0.8177 | 0.007 | - | - |
| TPropylAI | 1.006 | 124.5 | 0.991 | 0.009 | 5.89 | 0.22 |
| TButylAI | 1.153 | 145.3 | 1.157 | 0.003 | 6.39 | 0.22 |
| TPentylAB | - | 164.8 | 1.312 | 0.010 | 6.23 | 0.21 |
| THexylAB | - | 180.0 | 1.433 | 0.002 | 6.51 | 0.11 |
| THeptylAB | 1.529 | 193.1 | 1.537 | 0.004 | 7.62 | 0.10 |

* Ude and de la Mora, 2005.

References

1. E. Knutson, and K. Whitby, *Journal of Aerosol Science*, **6**, 443, 1975.
2. R. Flagan, *Aerosol Science and Technology*, **28**, 301, 1998.
3. P. McMurry, *Atmospheric Environment*, **34**, 1959, 2000.
4. M. Stolzenburg, University of Minnesota (1988).
5. R. Flagan, *Aerosol Science and Technology*, **30**, 556, 1999.
6. D. Chen, D. Pui, D. Hummes, H. Fissan, F. Quant, and G. Sem, *Journal of Aerosol Science*, **29**, 497, 1998.
7. J. Rosell-Llompart, I. Loscertales, D. Bingham, and J. Fernandez de la Mora, *Journal of Aerosol Science*, **27**, 695, 1996.
8. L. De Juan, and J. Fernandez de la Mora, *Journal of Aerosol Science*, **29**, 617, 1998.
9. S. Rosser, and J. Fernandez de la Mora, *Aerosol Science and Technology*, **39**, 1191, 2005.
10. P. Martínez-Lozano, and J. de la Mora, *Journal of Aerosol Science*, **37**, 500, 2006.
11. S. Zhang, Y. Akutsu, L. Russell, R. Flagan, and J. Seinfeld, *Aerosol Science and Technology*, **23**, 357, 1995.
12. H. Fissan, A. Pöcher, S. Neumann, D. Boulaud, and M. Pourprix, *Journal of Aerosol Science*, **29**, 289, 1998.
13. R. Sankaran, D. Holunga, R. Flagan, and K. Giapis, *Nano Letters*, **5**, 537, 2005.
14. Y. Kousaka, K. Okuyama, M. Adachi, and T. Mimura, *Journal of Chemical Engineering of Japan*, **19**, 401, 1986.
15. S. Ude, and J. Fernandez de la Mora, *Journal of Aerosol Science*, **36**, 1224, 2005.

16. J. Fernandez de la Mora, *Journal of Aerosol Science*, **33**, 411, 2002.
17. A. Zelenyuk, Y. Cai, and D. Imre, *Aerosol Science and Technology*, **40**, 197, 2006.
18. H. Tammet, *Journal of Aerosol Science*, **26**, 459, 1995.

Chapter 3: Finite Element Analysis of the nano-RDMA Geometry

3.1. Introduction

Measurements of the particle size distribution of aerosol nanoparticles have enabled new fundamental information about the atmosphere,^[1] *in situ* optimization of nanoparticle production,^[2] and controlled investigations of aerosol dynamics.^[3] At the heart of these measurements is the differential mobility analyzer (DMA). A DMA classifies charged aerosol particles according to their mobility (Z_p) in an electric field (E) between two electrodes (spaced a distance b apart). Particles enter the classifying region where the electric field is present and traverse a particle-free sheath flow (Q_{sh}). Particles with a certain mobility will exit through the opposite electrode after a fixed distance in the electric field. The device specifics (i.e., electrode spacing, sheath flow rate, geometry, and classifying region length) determine the voltage (V) required to obtain the requisite electric field to transmit particles of a particular range of mobilities through the device. The relative range of mobility distributions transmitted determines the instrument resolution. Resolution along with fraction transmitted and size range are the important characteristics of device performance.

A recent trend of aerosol research has been to develop tools capable of measuring particle size with atomic dimensions.[4-7] The major theoretical limitation on device performance for small particles is diffusion.[8] Diffusion spatially broadens the particle

distribution within the DMA, resulting in a broader range of voltages over which particles of a fixed single mobility are transmitted. Diffusion simultaneously limits transmission, as the spatial broadening of the distribution results in losses to the walls of the device.

Improving resolution and transmission is typically accomplished through reducing residence time and, therefore, spatial broadening of the particle distribution in the device. Residence time can be decreased either through increasing the sheath flow rate (Q_{sh}) or decreasing the spacing between the aerosol entrance and sample exit. The sheath flow rate can be increased up to the point where turbulence is induced, and the spacing between entrance and exit can be decreased only to a certain extent.

It has been shown that an optimum exists in the classifying column length for the cylindrical DMA (cDMA) geometry that consists of two coaxial cylinders with R_2 and R_1 . The condition that maximizes resolution is when the sizing column length is equal to the electrode spacing (i.e., $l = R_2 - R_1$). The optimum dimensions are not as clear for the Radial DMA (RDMA). The RDMA consists of parallel disk electrodes with the aerosol entering at R_2 and exiting through a hole in the center of the opposite electrode with a radius R_1 .

The theoretical guidelines for optimum performance are straightforward in appearance, but the actual device performance is usually less than theoretically predicted. The most significant limit on achieved resolution experimentally is usually attributed to electrode alignment for the cDMA and Winklmayr DMAs, as axial asymmetry has a significant impact on resolution. Often the impact is significant enough to warrant extreme care in alignment in order to achieve absolute best tolerances. The electrode

alignment in the RDMA also impacted the achieved resolution in the original RDMA, but this inefficiency has been limited in the design of the nano-RDMA.

The device transmission also improves with decreased residence time. The transmission through the classifying region is often secondary in importance as other areas impact transmission through losses due either to electrophoresis or to diffusion. These areas are often three dimensional in nature and therefore will not be treated due to memory limitations. For the purposes of this section, only transmission in the sizing region was considered.

Perfect agreement is not expected between theoretical and experimental results, but a few assumptions could be responsible for some of the disparity. The major simplifications in the theoretical analysis are the assumptions of a uniform electric field, a parabolic or plug flow profile, and a dirac delta function for the aerosol input location. The assumption of a dirac delta distribution at the inlet is actually quite good. The initial spatial distribution of the particles is quite finite provided that the gap of the aerosol inlet is set properly. Too wide of a gap would have the same effect as diffusion.

The assumption of uniform electric field is more problematic. The best electrode alignment will not ensure an electric field that is uniform throughout the device. The electric field in the area near the aerosol inlet and outlet is not perfectly axial, as the electrodes are not solid. The electrodes must permit particle transmission, resulting in some degree of field penetration or distortion in these areas. These non-uniformities should remain azimuthally symmetric, but could potentially impact the device performance.

The assumed flow profiles and field are not entirely correct for either the radial DMA (RDMA) or cylindrical DMA (cDMA) configuration. The flow field separates in the center of the RDMA, a clear deviation from the ideal flow profiles. The flow profile in the cylindrical DMA is disrupted by the introduction of the aerosol stream and the removal of the sample stream. These effects should be more substantial for DMAs where the aerosol inlet and outlet are a significant fraction of the device size than they are for the designs used to measure larger particles.

These assumptions have enabled theoretical analysis to provide guidelines for DMA design, but the actual impact of each assumption requires a computational approach to evaluate. For the purposes of this paper, we will present simulation results of the recently developed nano-RDMA.[9] The nano-RDMA was developed to measure nanoparticle size in the 1 to 12.5 nm range with high resolution and therefore the classifying region is small. Any non-idealities in design are magnified as they comprise a significant portion of the classifying region. For most DMA designs, lack of axial symmetry or concentricity is usually a major factor, but the nano-RDMA was designed to ensure a high degree of concentricity. While manufacturing perfection was not achieved with the nano-RDMA, improvements in resolution should also be achievable through design improvements.

In a previous report, finite element modeling of the aerosol behavior inside a mobility analyzer provided a clearer picture as to the deficiencies of the device operation.[10-11] Altering the device construction resulted in improved performance. In this report, we will present geometry modifications of the nano-RDMA that were simulated to determine the effect on resolution and transmission. We will explore how

simulated results deviated from theoretical assumptions. Finally, we will discuss recommendations for improvements.

3.2. Theoretical Considerations

The internal structure of the nano-RDMA was modeled assuming a two-dimensional axisymmetric geometry—a full-scale three-dimensional model was computationally prohibitive. Consequently, the results fail to capture some of the dynamics of the racetrack region, the aerosol inlet extension, the sheath gas distributor porous material, and the three-dimensional aspects of the mesh on the excess outlet. The racetrack region is included in the model in an axisymmetric manner so that particle deposition as the aerosol passes through the knife edge region is captured qualitatively. A separate analysis will be given for the aerosol inlet extension.

A MatLab script was used to generate the model geometry to be tested to permit facile testing of numerous parameters of the nano-RDMA. The standard model is shown in figure 3.1. The script enabled multiple permutations to the standard geometry, including the following parameters: (1) the knife edge gap size (parameter a), (2) the sizing column size (parameter b), and (3) the aerosol outlet size (parameter c). Additional simulations investigated the effect of the mesh on the excess outlet and the effect of aerosol flow rate. A majority of the simulation used the aerosol and sheath flow rates of 0.6 and 10 standard liters per minute (SLM) used in calibrating the nano-RDMA. The more common flow rates of 1 and 10 SLM (aerosol and sheath respectively) were simulated as well. Finally, a comparison is made between the nano-RDMA and the original RDMA.[12] The angle of convergence of the bottom plate was also simulated

but the results will not be presented here. Converging DMAs are known to result in lower resolution and this result was confirmed in the simulations.

For each set of parameters, the fraction transmitted (i.e., flux exiting the sample outlet divided by flux entering the aerosol inlet) was recorded for particles with integer mobility diameters in the range of one to ten nanometers. For each diameter, the geometry was simulated for a range of voltages around the ideal transmission voltage for the particle mobility diameter for the standard geometry. The step size for voltage variation was 0.005 of the ideal voltage.

The geometry was constructed and then loaded into a second MatLab script to be analyzed. The same script could be used for most of the different simulations.[13] The script allowed COMSOL to generate a standard mesh for the geometry that is refined using the standard method twice to generate a finer mesh followed by two further refinements of the mesh in sizing region of the device. Fewer refinements in the mesh resulted in poor performance of the model wherein the concentration profile did not match expected behavior or the mesh did not have sufficient density to ensure convergence.

The simulations required three modules to be solved to determine transmission for a given geometry: electrostatics, incompressible Navier-Stokes, and electrokinetic flow. The modules were solved sequentially rather than simultaneously, as the later is very memory intensive. The electrostatics module was solved first and then the incompressible Navier-Stokes and finally the electrokinetic flow. The incompressible Navier-Stokes module was only solved once for each geometry model since changing particle size and applied voltage did not affect the flow field. Rather than solving the

electrostatic module multiple times for each voltage and geometry, the electrostatic module was solved with the voltage scaled between zero and unity. The magnitude of the voltage was accounted for in the electrokinetic module through multiplying the particle mobility by the voltage. The electrokinetic module was solved repeatedly for each voltage, particle size, and geometry.

The transmission data were compiled, and a MatLab script was used to compute the calibration factor for the geometry, the transmission, and the resolution. The calibration factor was determined from fitting the transmission data as a function of voltage for each particle size to a lognormal distribution. From the product of the particle mobility and the geometric mean, the calibration factor was determined. The transmission and resolution were found using a separate fitting function that used the Stolzenburg transmission function and the non-linear fitting program *nlinfit* of MatLab. The program fit the transmission data using the following equation:

$$f(Z_p) = \frac{\Gamma_{out}}{\Gamma_{in}} = \eta(Z_p^*) \Omega_{Stolzenburg}(Z_p, Z_p^*, \beta, \delta = 0, \sigma_{Stolzenburg}), \quad 3.1$$

where $f(Z_p)$ is the ratio of the flux leaving the sampled outlet (Γ_{out}) to the flux entering the aerosol inlet (Γ_{in}), $\eta(Z_p^*)$ is the mobility dependent transmission efficiency, Z_p^* is the ideal mobility of a particular particle size, $\Omega_{Stolzenburg}$ is the Stolzenburg transfer function, β is the ratio of the aerosol to sheath flow rate (Q_a / Q_{sh}), δ is a parameter accounting for unbalanced flows (here it is 0), and $\sigma_{Stolzenburg}$ is the Stolzenburg broadening coefficient. The fitting routine solved for $\eta(Z_p^*)$ and $\sigma_{Stolzenburg}$ for each particle size, and subsequently converted $\sigma_{Stolzenburg}$ to a resolution.

3.3. Results and Discussion

3.3.1. *Electrostatics*

The solved electrostatic module for the standard geometry is shown in figure 3.2. The electric field lines were perpendicular to the z-axis for the most part with the exception of three locations where distortions from the uniform electric field lines are found. The first location is near the sample outlet where the electric field lines point toward the bottom plate. This distortion would cause charged particles to migrate in the direction of the arrow. Unlike the excess outlet, the sample outlet was not covered with a mesh, as this would impact particle transmission. The second distortion location was near the sheath gas inlet. As the particles were not introduced into this region, the electric field was not as important here as it is in other places. The final field distortion location was near the knife edge inlet, which is shown in greater detail in figure 3.3. The electric field was reduced in strength and is non-uniform across this region, providing a distribution of electric fields that particles experience upon entering the sizing portion of the device. The arrow indicating direction of the electric field on the top of the knife edge actually pointed upward. This would result in a favorable narrowing of the distribution as it emerges from this region that would improve the assumption of a dirac delta distribution of particles entering the classifying region.

The permutation from the standard geometry that caused the greatest divergence of the electric field was the removal of the mesh on the excess outlet. Removing the mesh on the excess outlet caused the electric field to be distorted in the excess outlet region in addition to the distortions in the electric field present with the mesh, as shown in figure 3.4. Also, the average magnitude of the electric field was less without the mesh

than with the mesh. A higher applied voltage was necessary to create the same magnitude of electric field.

3.3.2. Incompressible Navier-Stokes

The solution to the incompressible Navier-Stokes for the standard geometry is presented in figure 3.5. The streamlines were inclined relative to the electrode and not parallel as the parabolic and plug flow profiles assume. This should not affect particle transmission or resolution as the particles must traverse the same total amount of sheath gas to reach the streamlines exiting as the sampled flow. This solution changed only in minor ways with all geometry permutations. One unexpected behavior was that the separation streamline occurred closer to the middle of the gap than would be expected based on the ratio of the flow rates of 0.6 SLM sampled flow and 10 SLM excess flow, but no apparent recirculation zone was found at the separation streamline. The second insight obtained was that the high flow rate in the excess outlet results in a correspondingly high Reynolds number in this region and presents the main limitation to increasing the sheath flow rate. The diameter could be expanded here to permit operation with a higher sheath flow rate.

3.3.3. Electrokinetic Flow

The solution to the electrokinetic flow module for the standard geometry is presented in figure 3.6 with the applied voltage set as the theoretical voltage. The particles enter through the knife edge gap and remain narrowly distributed in space until they reach the area below the mesh. The particle stream in this area distributed more broadly in space with a fraction of the particles exiting with the excess outlet flow, and

the remaining particles exit with the sampled outlet flow. If this solution was overlaid on the incompressible Navier-Stokes solution, the region where this separation occurred does not overlap with the location where the separation of flow stream lines do. The electric field must force the particles through the location where the streamlines separate. If an actual recirculation zone did appear in this region,[14] the electric field should prevent any charged particles from accumulating.

Without the mesh, the particle trajectories change substantially for the same applied voltage, as shown in figure 3.7. The average field strength was reduced to the point where the entire particle stream exited the device with the excess flow. A higher applied voltage was required to transmit particles to the sampled outlet.

3.3.4. Calibration Factor

The calibration factor was determined for the different geometry permutations modeled. It was found to be $110.2 \text{ cm}^2/\text{s}$ for the standard geometry with the mesh in place, whereas it was $131.4 \text{ cm}^2/\text{s}$ without the mesh. The experimentally determined value of the calibration factor ($125.6 \text{ cm}^2/\text{s}$)[9] is between these two limits. This suggests that the mesh does not ensure electric field uniformity across the entire outlet. It is plausible that the porous nature of the mesh diminished the effective field in the center of the device introducing electric field non-uniformities. The magnitude of the electric field on the mesh could be altered independently to simulate the porous nature of the mesh as it was a separate boundary in the model. Using a value of between 0.85 and 0.90V on the mesh boundary reproduced approximately the experimentally observed calibration factor.

The other parameters that affect the calibration factor were the gap between plates (*b*), the aerosol outlet gap (*c*), and the aerosol inlet gap (*a*). Smaller gaps between the

electrodes decreased the calibration factor, as shown in figure. 3.8. The decreased gap caused the flow to accelerate, but simultaneously increased the electric field and decreased the axial distance necessary to travel to be transmitted to the sampled flow. The aerosol inlet gap changed the effective electrode spacing and therefore affected the calibration factor in a similar manner, as shown in figure 3.9.

The aerosol outlet gap determined the length of the classifying column. Smaller outlet gaps corresponded to a longer classifying region and a more uniform electric field, resulting in a smaller calibration factor, which was consistent with theoretical expectations. The calibration factor determined for changes in the aerosol flow rate (Q_a) changed only in a minor way (less than 1%) and this was reflected in the theoretical equation for transmission that omitted this variable.

3.3.5. Resolution

The transmission data for the different particle sizes was well fit using the Stolzenburg transfer function to obtain the resolution of the standard geometry, which is shown in figure 3.10. The resolution rose sharply and leveled off at a value of approximately 15. This was lower than expected since the theoretical limit is 16.7, a value based on the ratio of the sheath to aerosol flow rate.[8] The possible causes for this behavior were the electric field distortions near the aerosol inlet and outlet, and the spatial broadening in the region near the mesh. Examining the electrokinetic module, the spatial broadening of the distribution before the region near the mesh was minimal and therefore was less likely responsible for the deviation. However, the spatial broadening near the mesh was more significant and was a possible cause of the lower-than-expected resolution.

The resolution without the mesh was lower than the resolution with the mesh even though the voltage used to classify particles of the same mobility was higher without the mesh. The solution without the mesh has the same distortions near the aerosol inlet as the one with the mesh. Yet, the one without the mesh has a greater degree of distortion in the region near the mesh that could be responsible for the difference. These results suggested that the field distortions can affect resolution even when axis-symmetric.

The second important parameter simulated was the separation between the electrodes, the results of which are shown in figure 3.11. The electrode separation (b) that maximized resolution was 7.5 mm. The simulations indicated that an optimum existed for the RDMA when the aerosol inlet radius (R_2) is equal to the electrode gap (b), suggesting that the aerosol outlet gap (R_1) did not impact the resolution. Simulations that varied the aerosol outlet gap (c) showed that the resolution is only affected in a minor way by this parameter, as shown in figure 3.12. Reducing the electrode spacing to 7.5 mm will limit the maximum operating voltage of the nano-RDMA to 7.5 kV. The impact of such a change on maximum measurable particle size would need to be determined experimentally. This improvement did increase the resolution to about 15.7 but still not to the theoretical limit.

The aerosol inlet gap did have a small impact on resolution, as shown in figure 3.13. Decreasing the gap spatially restricted the particles, which improves the resolution slightly. Simulating a geometry with the optimal electrode spacing ($b = 7.5$ mm) and the optimal inlet gap did not lead to a further improvement in resolution.

The inability to achieve the maximum resolution indicated a minor inherent inefficiency in the RDMA design. Examining the electrokinetic result at the voltage

corresponding to the maximum transmission showed an incomplete separation, see figure 3.14. A portion of the aerosol exited with the excess flow, indicating that at maximum transmission the voltage is not sufficient to drive all of the particles into the sampled outlet flow. The cause could be the non-uniform electric field in the aerosol outlet region. The electric field directed the particles toward the bottom plate, expanding the aerosol over a broader region. Using a higher voltage than optimum would improve the separation, but would simultaneously force particles to deposit on the bottom plate. The net result of the incomplete separation was a broadening of the measured distribution and a maximum resolution that was lower than theoretically achievable.

A more uniform electric field could be generated for the purposes of these simulations using a flat internal boundary across the aerosol sampled outlet. The model could not be solved with this change due to memory limits, as the second internal boundary created a high density of mesh points.

Overall, the resolution of the nano-RDMA is still considerably better than the resolution of the RDMA for the 1 to 10 nm size range, as shown in figure 3.15. The maximum resolution achieved is higher for the nano-RDMA, as well. The lower maximum resolution for the RDMA is most likely a result of the spacing between the inlet and outlet (R_2) being more than the electrode gap (b). The figure includes the resolution for the higher aerosol flow rate of 1 SLM for the nano-RDMA and RDMA. The maximum resolution is again lower than the theoretical value for most likely the same reasons as described before.

3.4. Summary

The resolution of the current nano-RDMA can be improved through decreasing the electrode spacing (b) to a value of 7.5 mm. The optimum condition for the RDMA geometry is therefore when the inlet radius (R_2) equals the electrode spacing (b). Modifying the electrode gap maximized the resolution, but did not quite achieve the theoretical resolution most likely due to a non-uniformity in the electric field. The simulation results indicate that the assumptions of parabolic/plug flow profile and dirac delta spatial distribution at the inlet were approximations but did not impact the resolution. The assumption of uniform electric does impact the resolution as the non-uniform electric field in the aerosol outlet region spatially broadens the distribution.

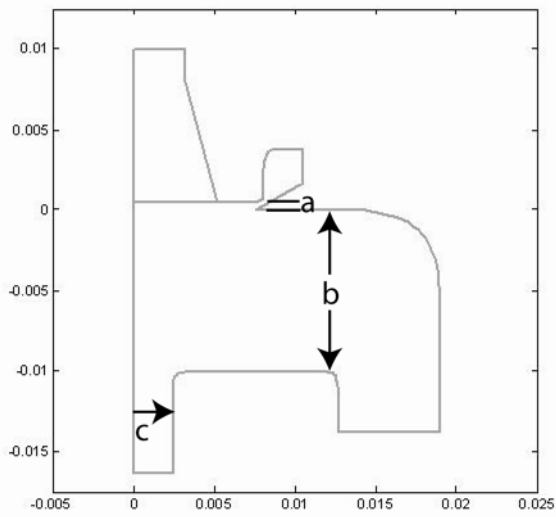


Figure 3.1. Outline of the Axis-Symmetric Model.

Outline of the axis-symmetric two-dimensional model used to calculate the resolution of the nano-RDMA. The aerosol inlet gap (a), the electrode spacing (b), and the aerosol outlet gap (c) are labeled accordingly.

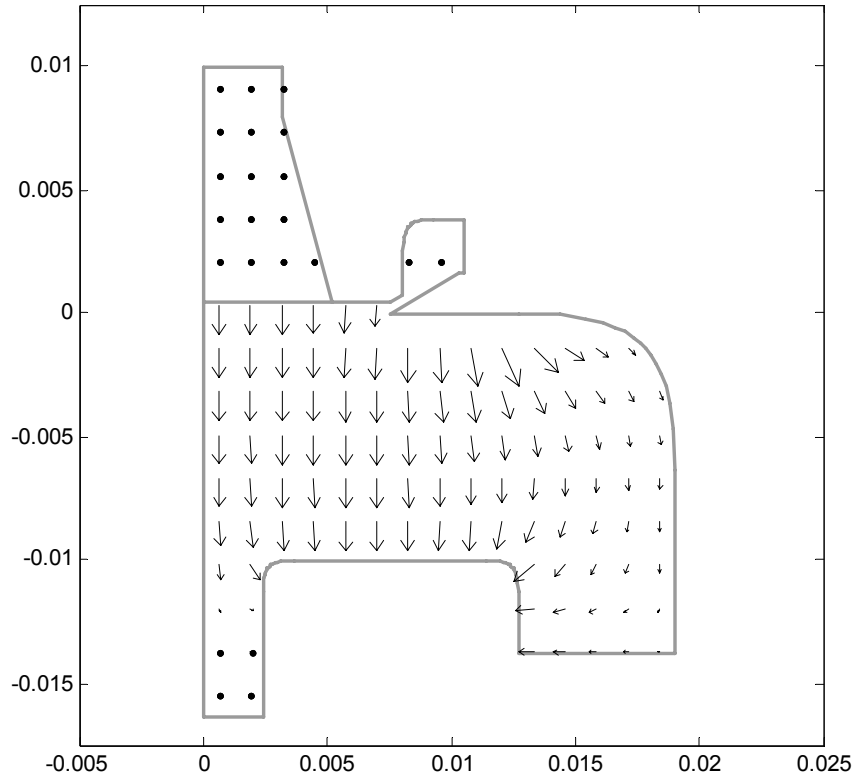


Figure 3.2. Electrostatics Solution.

Solution of the electrostatics module for the standard nano-RDMA geometry.

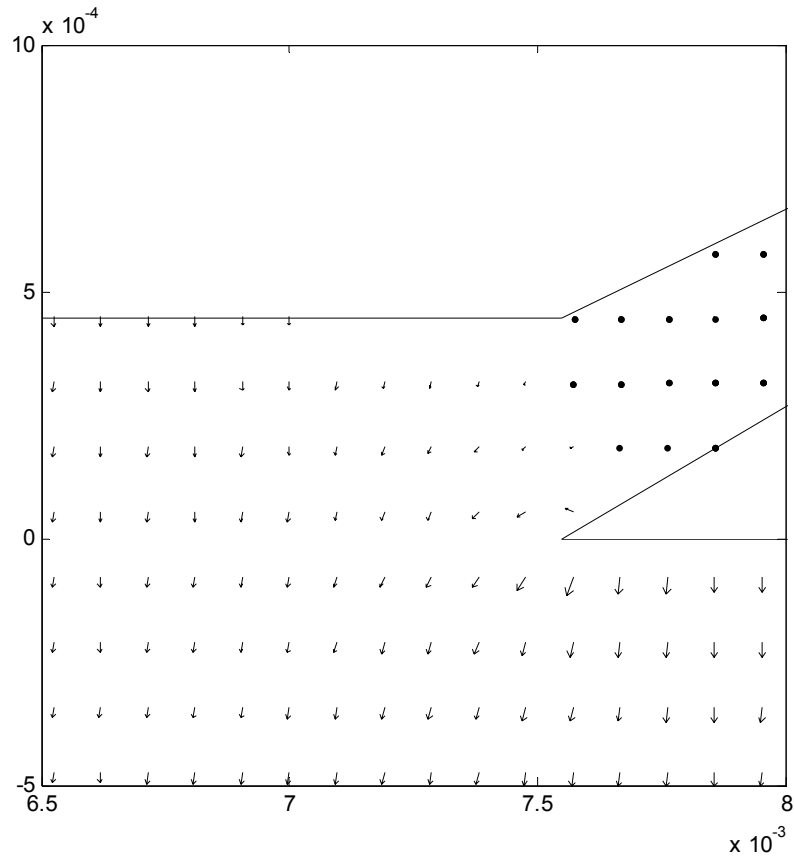


Figure 3.3. Inset of Aerosol Inlet Region.

Inset of the aerosol inlet region demonstrating the direction of the electric field.

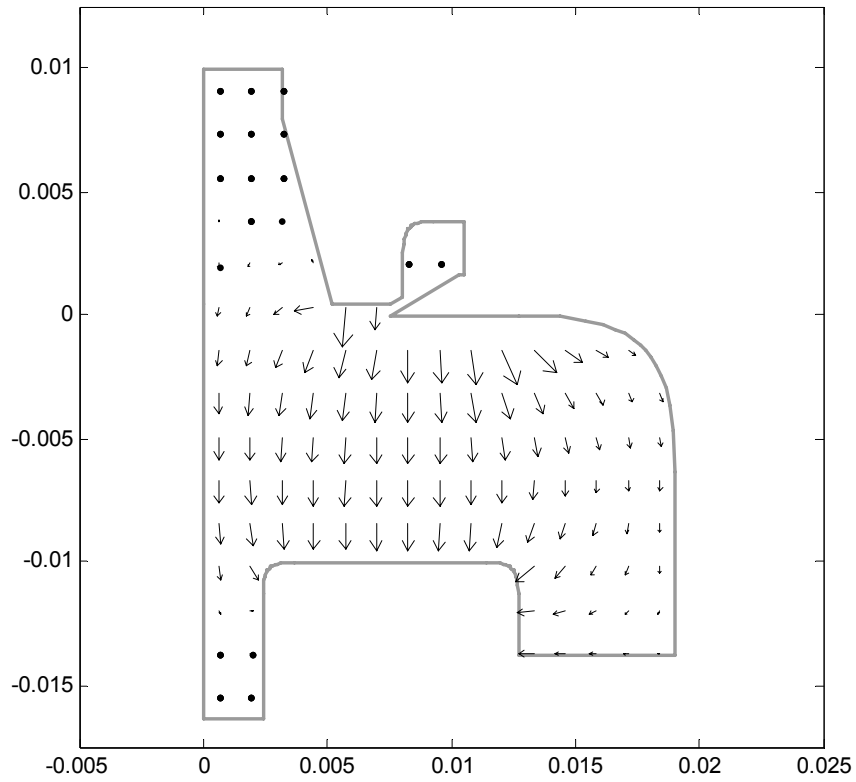


Figure 3.4. Electrostatics Solution without Mesh.

Solution to electrostatics module for the standard geometry without the mesh on the excess outlet.

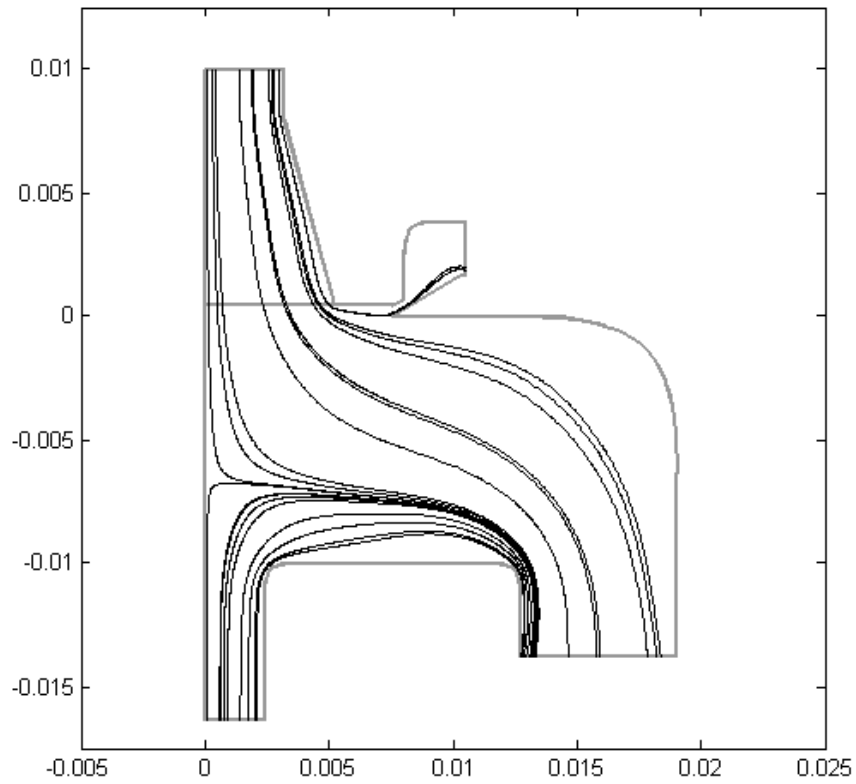


Figure 3.5. Navier-Stokes Solution.

Solution to the incompressible Navier-Stokes module for the standard nano-RDMA geometry. The flow rates are balanced with an aerosol and sheath flow rate of 0.6 and 10 SLM, respectively.

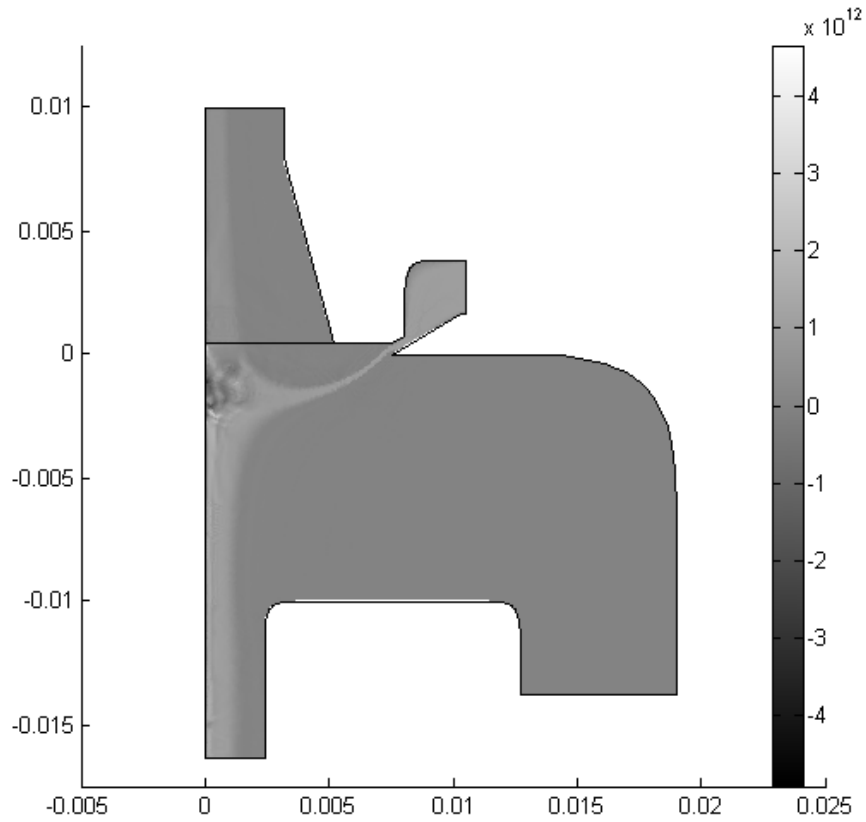


Figure 3.6. Electrokinetic Flow Solution.

Solution to electrokinetic flow module for the standard nano-RDMA geometry for particles with a 10 nm mobility diameter. The applied voltage is the theoretical voltage necessary to transmit 10 nm particles.

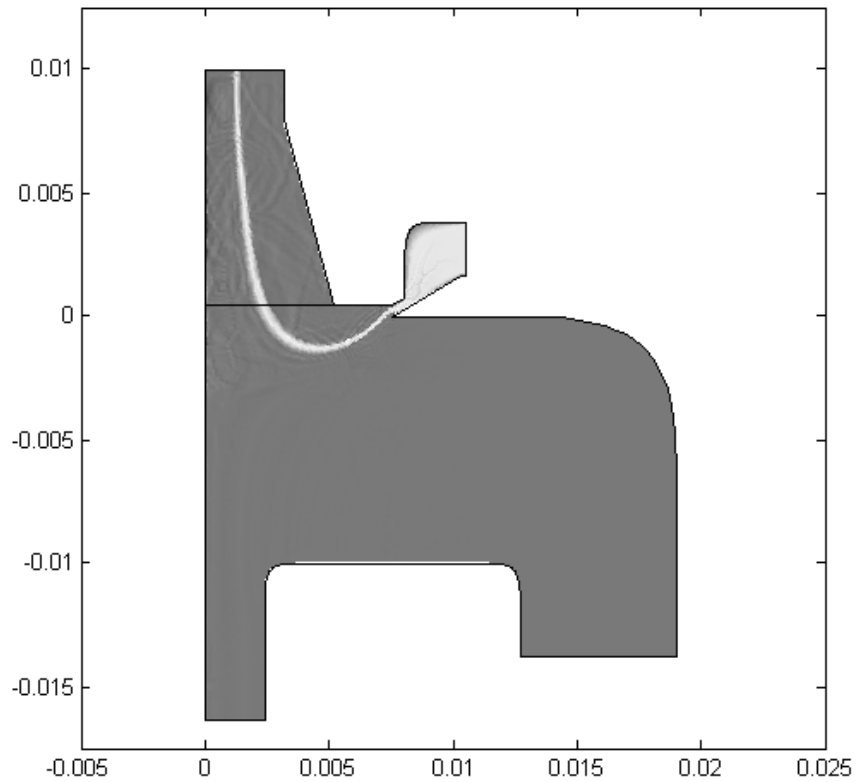


Figure 3.7. Electrokinetic Flow Solution without Mesh.

Solution to electrokinetic flow module for standard nano-RDMA geometry without the mesh on the excess outlet for 10 nm particles. The voltage was the ideal theoretical voltage necessary to transmit 10 nm particles.

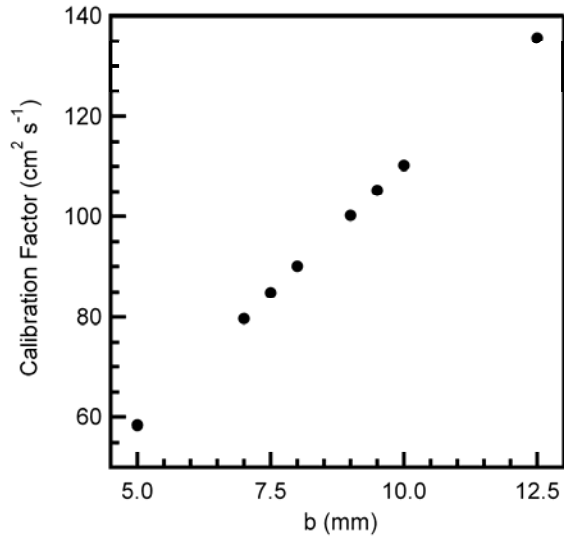


Figure 3.8. Calibration Factor for Electrode Spacing.

Calibration factor for different electrode gap spacings (b). The standard gap was 10 mm.

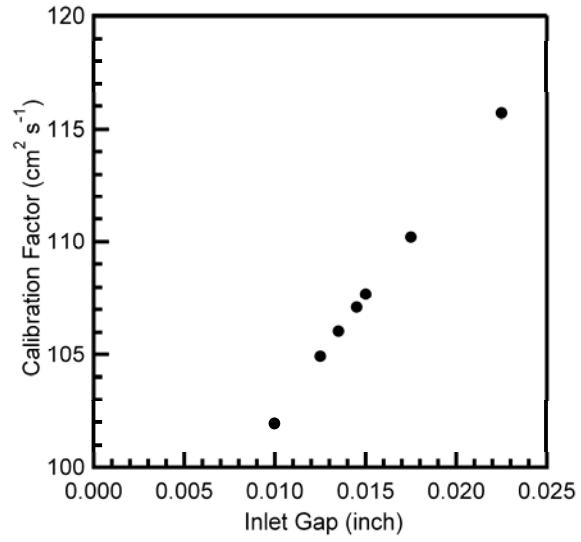


Figure 3.9. Calibration Factor for Aerosol Inlet Gap.

Calibration factor for different aerosol inlet gaps. The standard gap was 0.0175 inch.

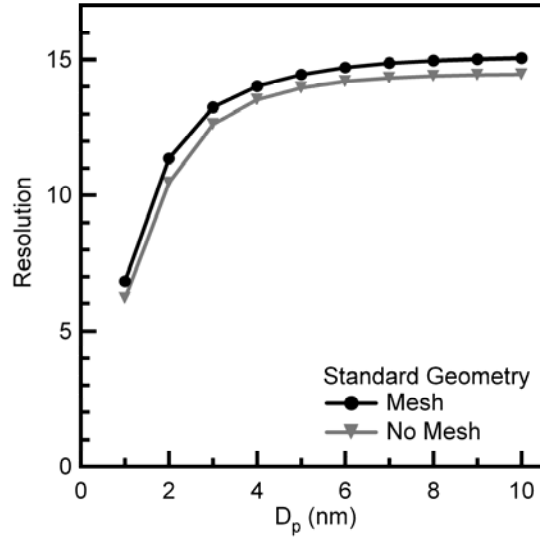


Figure 3.10. Resolution of nano-RDMA.

Comparison of the resolution for the standard nano-RDMA geometry with and without the mesh.

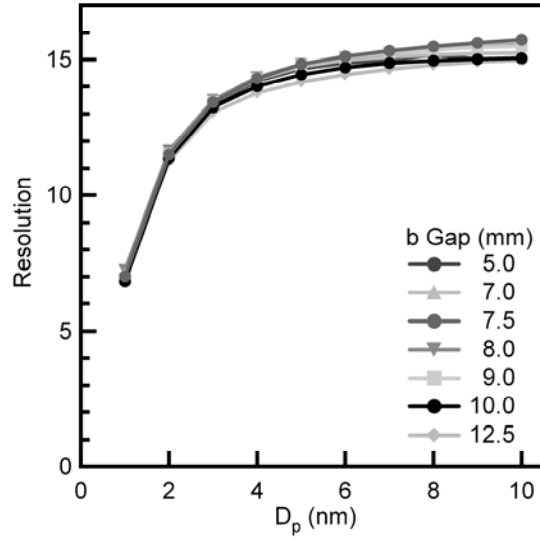


Figure 3.11. Resolution for Different Electrode Spacings.

Comparison of the resolution for the standard nano-RDMA geometry with different electrode gap spacings (b). The standard gap was 10 mm.

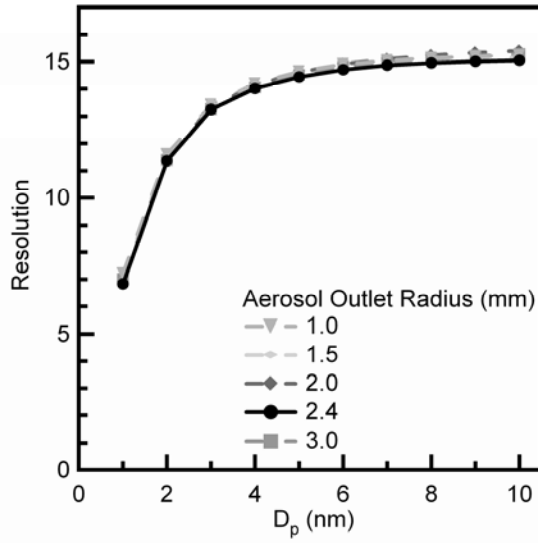


Figure 3.12. Resolution for Different Aerosol Outlet Gaps.

Comparison of the resolution for the standard nano-RDMA geometry for different aerosol outlet gaps (R_2). The standard gap was 2.4 mm.

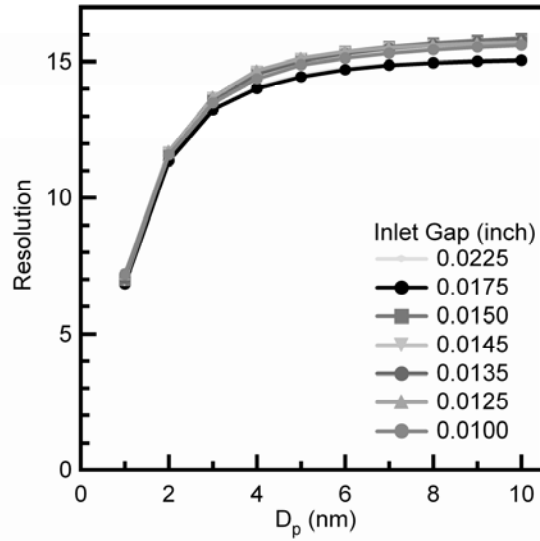


Figure 3.13. Resolution for Different Aerosol Inlet Gaps.

Comparison of the resolution for the standard nano-RDMA geometry with different aerosol inlet gaps. The standard gap was 0.0175 inch.

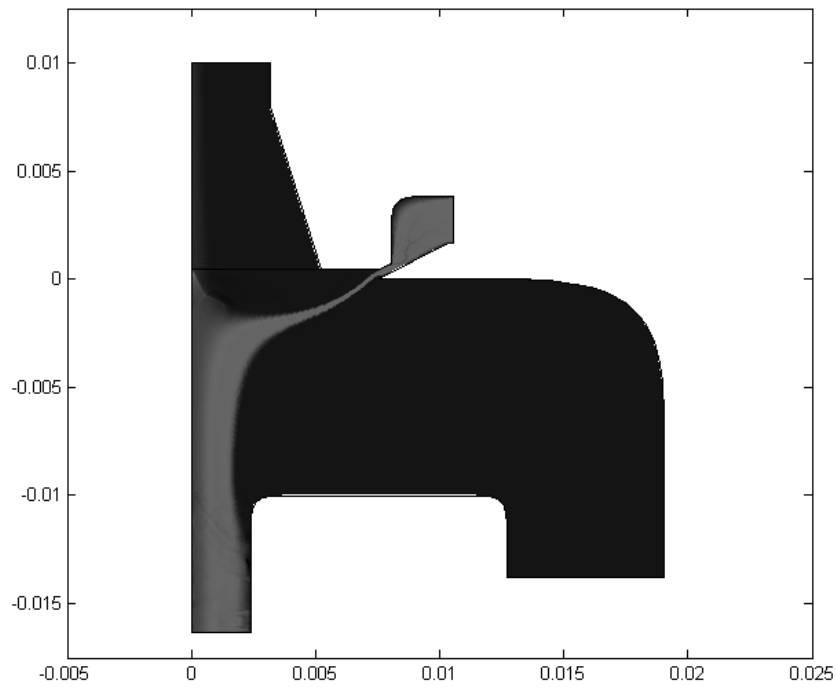


Figure 3.14. Electrokinetic Flow Solution at Optimal Voltage.

Solution to electrokinetic flow module for optimal voltage using the standard nano-RDMA geometry. The particle mobility diameter was 10 nm.

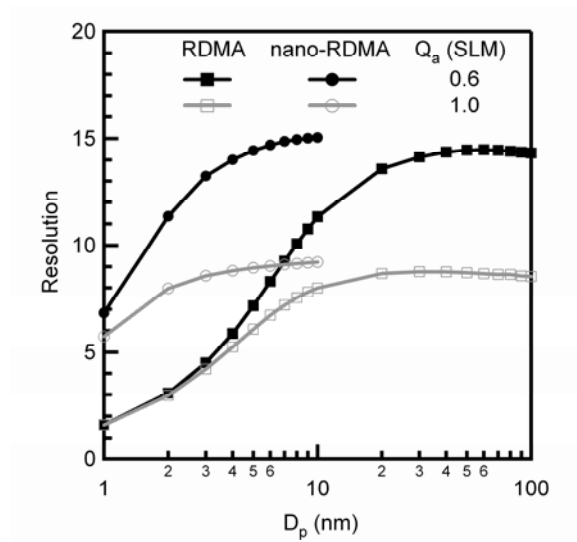


Figure 3.15. Resolution Comparison Between the nano-RDMA and RDMA.

Comparison of the resolution between the nano-RDMA and the RDMA using two different flow-rate ratios.

References

1. M. Kulmala, I. Riipinen, M. Sipila, H. Manninen, T. Petaja, H. Junninen, M. Maso, G. Mordas, A. Mirme, and M. Vana, *Science*, **318**, 89, 2007.
2. D. Holunga, R. Flagan, and H. Atwater, *Industrial and Engineering Chemistry Research*, **44**, 6332, 2005.
3. D. Rader, and P. McMurry, *Journal of Aerosol Science*, **17**, 771, 1986.
4. S. Friedlander, and D. Pui, *Journal of Nanoparticle Research*, **6**, 313, 2004.
5. J. Santos, E. Hontañón, E. Ramiro, and M. Alonso, *Atmospheric Chemistry and Physics*, **9**, 2419, 2009.
6. J. Rosell-Llompart, I. Loscertales, D. Bingham, and J. Fernandez de La Mora, *Journal of Aerosol Science*, **27**, 695, 1996.
7. D. Chen, D. Pui, D. Hummes, H. Fissan, F. Quant, and G. Sem, *Journal of Aerosol Science*, **29**, 497, 1998.
8. R. Flagan, *Aerosol Science and Technology*, **30**, 556, 1999.
9. N. Brunelli, R. Flagan, and K. Giapis, *Aerosol Science and Technology*, **43**, 53, 2009.
10. D. Chen, D. Pui, G. Mulholland, and M. Fernandez, *Journal of Aerosol Science*, **30**, 983, 1999.
11. D. Chen, and D. Pui, *Journal of Aerosol Science*, **28**, 985, 1997.
12. S. Zhang, Y. Akutsu, L. Russell, R. Flagan, and J. Seinfeld, *Aerosol Science and Technology*, **23**, 357, 1995.

13. *The script file had to be modified slightly for the simulations of the aerosol outlet radius. Decreasing the size of the outlet radius resulted in a re-numbering of the boundaries that required altering the boundary conditions appropriately.*
14. J. Fernandez de la Mora, *Journal of Aerosol Science*, **33**, 411, 2002.

Chapter 4: Microhollow Cathode Discharge Operating Conditions Impact on Nanoparticle Size Production

“There’s plenty of room at the bottom.” — R. Feynman

4.1. Introduction

Nanoparticles have emerged as a principle component in many fields of research, ranging from heterogeneous catalysis^[1] to aerosol science^[2] to biology.^[3] The aspects of nanoparticles that enable these applications are the ratio of surface area to volume and/or the quantum confinement effect of the nanoparticles. The actual particle size is invariably one of the most important factors in determining the resultant optical, magnetic, and/or catalytic properties.

The desire to control precisely particle size has led to many synthesis techniques, including liquid and aerosol methods. Liquid methods have improved substantially in their ability to generate monodisperse distributions,^[4-5] but at the difficulty associated with using surfactants to cap and to control the growth process may not be desirable. Aerosol methods are favorable in this regard as collection can proceed independent of synthesis and the capping material can be selected.^[6]

A microhollow cathode discharge (MHCD) was recently demonstrated to generate an aerosol of silicon nanoparticles from silane.^[7] The size of nanoparticles produced was measured *in situ* using a standard aerosol technique with a Radial

Differential Mobility Analyzer (RDMA) to be in the 3 to 5 nm size range. The only variable reported to affect the nanoparticle size was the concentration of silane passed through the discharge.

The RDMA was capable of the size measurements, but was not ideal since it was not designed to measure particle size below 8 nm.[8] A new RDMA (i.e., the nano-RDMA) has recently been reported that is fully capable of making size measurements in the 1 to 12 nm size range.[9] In this section, particle size measurements made using a nano-RDMA will be reported from the synthesis of nanoparticles. The effect on particle size of the following parameters will be reported: (1) silane concentration, (2) plasma flow rate, (3) plasma current, and (4) germanium concentration (no silane).

4.2. Experimental Method

The size of nanoparticles produced using a MHCD were determined using the setup shown in figure 4.1. The MHCD was constructed as previously reported.[7] Briefly, the discharge consisted of two electrodes where one was a stainless steel (SS) capillary (cathode, I. D. $\approx 180 \mu\text{m}$, length 15 mm) and the other was a SS tube (anode, O. D. $\approx 3 \text{ mm}$). The two electrodes are maintained at a fixed separation of 1 mm. Between the electrodes the discharge was sustained using a high voltage power supply with a current-limiting resistor in series. The electrodes were enclosed inside a glass tube (O. D. $\approx 12 \text{ mm}$) using UltraTorr and Swagelok fittings.

Three separate gas streams controlled with mass flow controllers were delivered to the MHCD. Two gas streams (an ultrahigh purity argon and the other 20 ppm silane in argon or 21 ppm germane in argon) were passed through the capillary. This stream passed directly through the most intense portion of the plasma that was located inside of

the capillary. The third stream was introduced in the gap between the electrodes where the afterglow of the discharge was visible. This stream served to dilute the particle stream emerging from the capillary. The combined stream with a total flow rate of 600 standard cubic centimeters per minute (sccm) passed through the anode that is connected to the nano-RDMA for *in situ* particle size analysis. The flow rate through the capillary was maintained at 150 sccm for the experiments studying the effects of plasma power and hydrogen concentration. For the experiments varying the flow rate through the capillary, the concentration of silane was maintained constant at 3 parts per million (ppm).

The nano-RDMA used for these measurements was the first version. It was operated in voltage stepping mode for all experiments using a 10 standard liters per minute (SLM) nitrogen sheath flow rate. Stepping mode consisted of setting the voltage on the nano-RDMA and waiting two seconds while this voltage stabilized. The current produced by the charged particles transmitted through the nano-RDMA was measured with a home-built Faraday cup electrometer sensitive to ± 1 fA.

The particle composition of the germanium nanoparticles was confirmed through depositing directly from the discharge on a silicon wafer that was cleaned with hydrofluoric acid (the composition of silicon nanoparticles was confirmed in the previous report[7]). In this configuration, the wafer was positioned so that it rested on the anode on top of a holder that allowed the gas flow to exit through holes drilled through the radius, as shown in figure 4.2. After exposing the sample to air, the sample was analyzed using energy dispersive spectroscopy (EDS) in a scanning electron microscope (SEM).

4.3. Results and Discussion

The results for experiments varying plasma current are presented first. In figure 4.3, the particle size distributions measured for various current levels is presented. Except for the lowest current (i.e., 2.5 mA), the distributions were approximately identical. This indicates a saturation type behavior in plasma current. The plasma current was closely associated with input power as the voltage between the electrodes varies slightly with current. Beyond a certain power input, the MHCD did not require additional power to decompose the gaseous precursor. Due to these data, the MHCD was operated typically using plasma currents of 7.5 mA.

Operating with the lowest power impacted the heating in the discharge and the energy distribution of the electrons. The plasma absorbed less power and did not experience as much joule heating, lowering the neutral gas temperature of the discharge. At the same time, the plasma density was lower, resulting in fewer available energetic electrons to further ionize neutral species and to break apart molecules. Due to these two effects at low power, it is likely that less precursor was decomposed and therefore the result was smaller nanoparticles.

The results for different silane concentrations were repeated as well using the range-appropriate nano-RDMA. As shown in figure 4.4, the size distributions revealed a similar trend of increasing particle mobility diameter with increasing precursor concentration, but the measured distributions were narrower than previously reported due to the better resolution of the nano-RDMA. The size distributions broadened and increased in concentration of particles produced with increasing concentration as well, as reported previously. The concentrations measured here are similar to those reported

previously. The final observation made using the nano-RDMA was that particles smaller than 2.5 nm were found for concentrations less than 3 ppm.

The third parameter investigated was the effect of the flow rate through the capillary on particle size production, demonstrated in figure 4.5. It was found that the flow rate through capillary does not affect particle size produced. This result was somewhat peculiar as the different flow rates should correspond to different residence times in the discharge. It is important to note that flow rate through the capillary is most likely not directly related to residence time, as the plasma volume inside the capillary could expand or contract depending on the actual flow rate. The flow rate through the plasma did not appear to affect the concentration of particles produced either despite a greater amount of precursor (same concentration) passing through the discharge. To fully explain this result would require simulations of the process that led to particle formation as well as the particle dynamics in and after the discharge. A possible explanation for this result is due to particle loss. With the same precursor concentration, the discharge nucleated particles of identical size for each of the flow rates tested. At the higher capillary flow rates, the flow rate of the argon stream introduced in the afterglow portion was lower. With the gas emerging from the capillary expanding and the lower flow rate mixing in the afterglow, more particle deposition could occur at the anode. The lower sheath flow rate would decrease the buffer thickness that particles would have to travel to deposit on the anode.

The final variable investigated for its affect on particle size production was germane concentration in the discharge, shown in figure 4.6. The particle size increased and the size distribution broadened with increasing amounts of germane introduced into

the flow through the capillary. The germanium nanoparticle size produced was larger than the silicon nanoparticle produced with similar precursor concentrations. The difference could partially be attributed to bond length, but could also be due to a difference in growth kinetics.

The maximum concentration of germane that could be introduced into the discharge for extended periods of time was 4 ppm. This was lower than the limit for silane (5 ppm). Using high concentrations of precursor caused material to deposit inside the capillary, increasing the pressure upstream of the capillary. The capillary would eventually clog completely, extinguishing the microplasma and requiring installation of a new capillary.

The identity of the germanium nanoparticles were confirmed through collecting the nanoparticles on a silicon substrate and measuring the energy dispersive spectra (EDS) in a SEM, as shown in figure 4.7. The spectra confirmed the presence of germanium, but also included silicon, oxygen, and carbon from the substrate. No metallic impurities from the capillary were observed. The lack of metallic impurities was a significant observation given the results associated with sputtering of the capillary (chapter 5). This suggested that a gaseous precursor introduced into the microplasma inhibited sputtering. The same material that caused the capillary to clog at high precursor concentrations most likely deposits on the capillary walls, coating the surface and preventing the sputtering of the metallic electrode.

4.4. Summary

The effect of three important parameters (plasma power, flow rate, and gas composition) on particle size produced was measured. The mean particle size and

standard geometric deviation increased with silane concentration passed through the discharge, but the size distributions were narrower than previously reported due to the improved resolution of the nano-RDMA. A threshold plasma current is needed for the discharge to form particles with identical sizes while the flow rate through the capillary did not affect the particle size produced or number concentration. Introducing germane into the discharge resulted in the production of germanium nanoparticles and did not produce additional sputtered material.

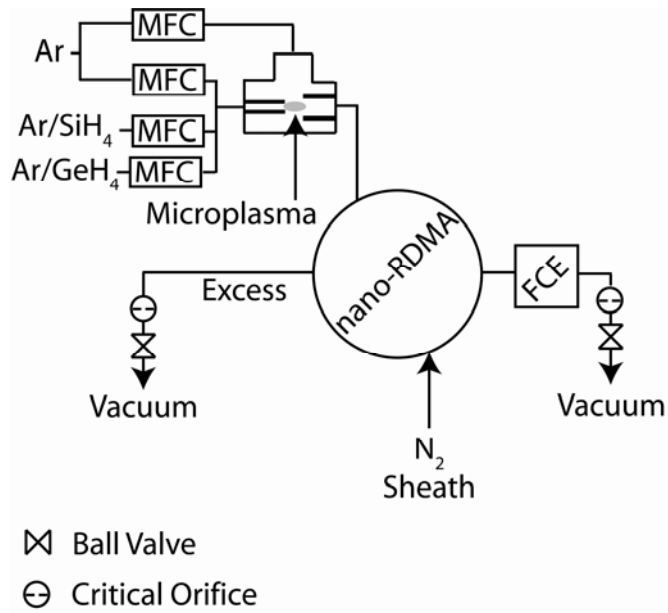


Figure 4.1. Schematic of Microplasma.

Schematic of experimental set up used to measure the effect of the microplasma operating conditions on nanoparticle production.

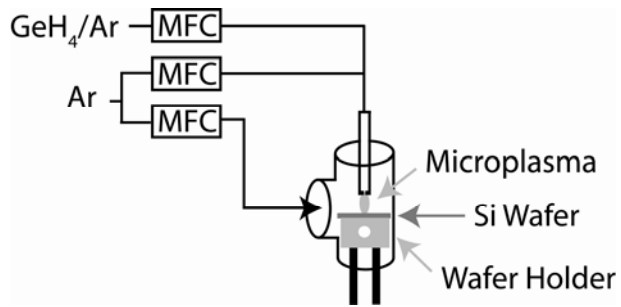


Figure 4.2. Schematic of Microplasma Deposition.

Schematic of experimental setup used to collect germanium nanoparticles. The silicon wafer was positioned on a holder constructed of aluminum.

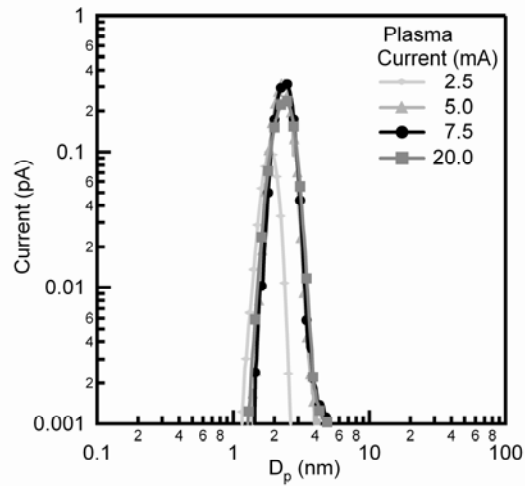


Figure 4.3. Size Distribution for Different Plasma Currents.

Silicon nanoparticle size distribution produced using the microplasma at different currents. The microplasma was operated with 3 ppm of silane and the total flow rate through the capillary was 150 sccm.

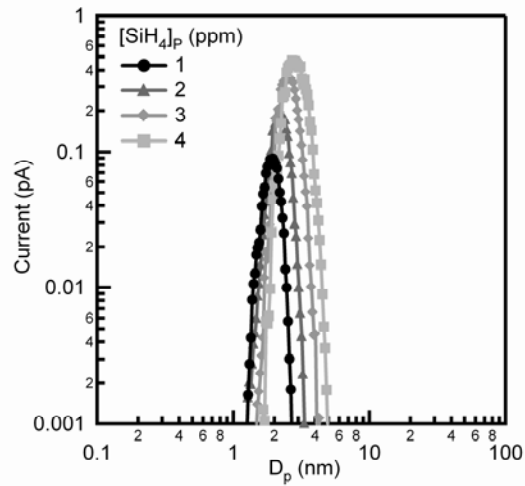


Figure 4.4. Size Distribution for Different Silane Concentrations.

Silicon nanoparticle size distribution produced from a single microplasma with different concentrations introduced into the microplasma. The plasma current was 7.5 mA and the total flow rate through the capillary was 150 sccm.

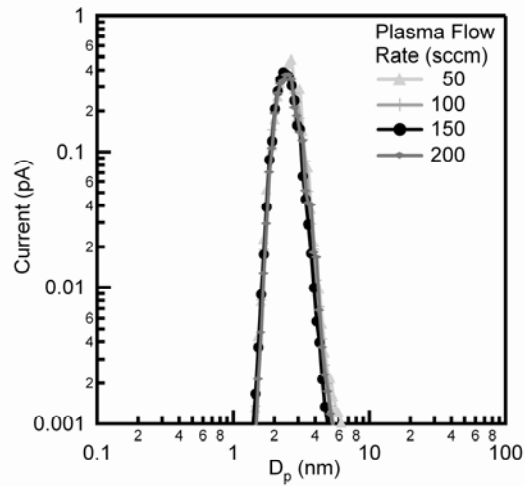


Figure 4.5. Size Distribution for Different Plasma Flow Rates.

Silicon nanoparticle size distribution produced using a microplasma with different flow rates through the capillary. The silane concentration was 3 ppm and the plasma current was 7.5 mA.

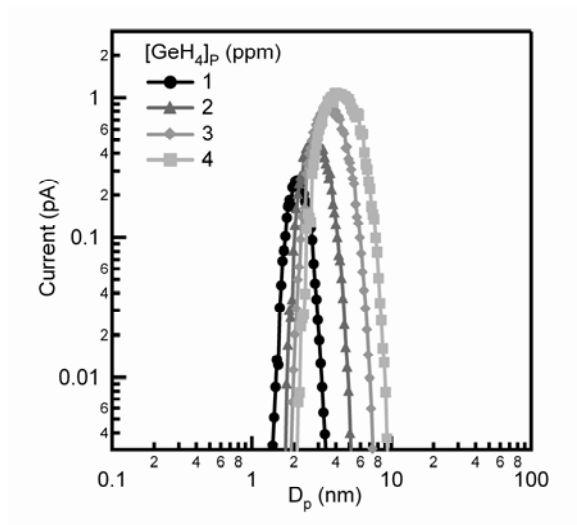


Figure 4.6. Size Distribution of Germanium Nanoparticles.

Germanium nanoparticle size distribution produced using a microplasma with different precursor concentrations flowing through the capillary. The total flow rate through the capillary was 150 sccm and the plasma was operated with a current of 7.5 mA.

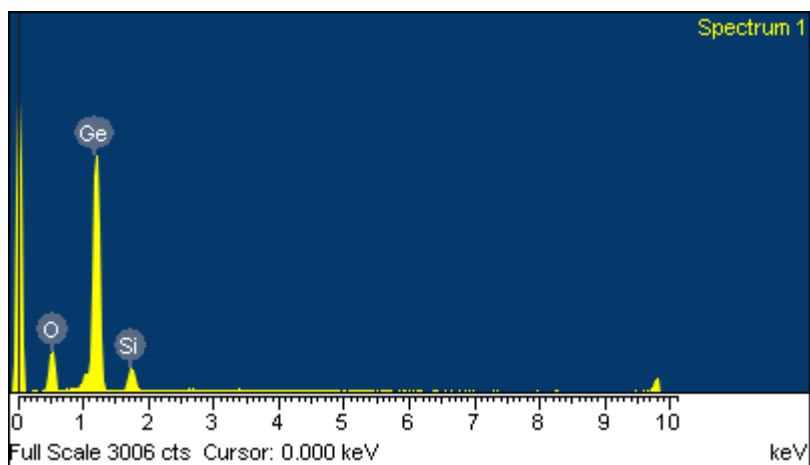


Figure 4.7. EDS of Germanium Nanoparticles.

EDS of germanium nanoparticles deposited on a silicon wafer. No evidence of iron was observed.

References

1. A. Bell, *Science*, **299**, 1688, 2003.
2. P. Winkler, G. Steiner, A. Vrtala, H. Vehkamäki, M. Noppel, K. Lehtinen, G. Reischl, P. Wagner, and M. Kulmala, *Science*, **319**, 1374, 2008.
3. W. Chan, and S. Nie, *Science*, **281**, 2016, 1998.
4. C. Murray, D. Norris, and M. Bawendi, *Journal of the American Chemical Society*, **115**, 8706, 1993.
5. H. Song, F. Kim, S. Connor, G. Somorjai, and P. Yang, *Journal of Physical Chemistry B-Condensed Phase*, **109**, 188, 2005.
6. Y. Liao, and J. Roberts, *Journal of the American Chemical Society*, **128**, 9061, 2006.
7. R. Sankaran, D. Holunga, R. Flagan, and K. Giapis, *Nano Letters*, **5**, 537, 2005.
8. R. Flagan, *Aerosol Science and Technology*, **30**, 556, 1999.
9. N. Brunelli, R. Flagan, and K. Giapis, *Aerosol Science and Technology*, **43**, 53, 2008.

Chapter 5: Nanoparticle Production from Cathode Sputtering in High-Pressure Microhollow Cathode and Arc Discharges

5.1. Introduction

Sputtering is a fundamental aspect of plasma operation and has been utilized to volatilize metal atoms for the purpose of manufacturing metallic interconnects, thin films, and patterned structures.[1-2] For many of these applications, the plasma is typically operated at low pressure with a well-defined sheath region above the cathode target. Positively charged ions are accelerated in this region, gaining sufficient translational energy[3] to induce sputtering when they strike the surface of the metal electrode. The ion energy gain in the sheath depends on the ion mean free path and, thus, the background neutral gas pressure. Numerous collisions at atmospheric pressure limit the ion energy gain and the ability to sputter the target material. Therefore, high-pressure plasmas are not very effective for sputtering.

Microhollow cathode (MHC) discharges[4] operating at atmospheric pressure have recently emerged as promising reactors for nanoparticle synthesis from gaseous precursors.[5][6] Since the cathode electrode confines the microdischarge, the ions are expected to sputter the cathode material. In this chapter, we demonstrate that cathode sputtering in the microdischarge produced extremely narrow size distributions of very small metal nanoparticles. We further compare the microdischarge sputtering results to those obtained from a high voltage arc discharge operated at atmospheric pressure at similar plasma power.

5.2. Experimental Method

The MHC discharge configuration[5] is shown in figure 5.1a. This is a short residence time reactor that permits the nucleation of particles but limits their growth as they are swept out of the small plasma volume. Rather than stainless steel electrodes that contain multiple elements, the setup consists of two oxygen-free high-conductivity (OFHC) copper electrodes, separated by a gap and enclosed in a glass tube and sealed with O-rings. The cathode is a single rod (O. D. \approx 38 mm) that has been machined to have a rodlike protrusion (O. D. \approx 4 mm) on one face through which a small hole (I. D. \approx 180 μ m) has been drilled on axis. This piece is biased negatively using a high-voltage DC power supply (Matsusada, Model AU-SR60) through a current limiting power resistor. The anode is a drilled (I. D. \approx 2 mm) OFHC copper piece, residing on a glass tube (O. D. \approx 3 mm) and connected to ground via a gold wire (O. D. \approx 130 μ m). The system is sealed on the anode side with an UltraTorr fitting, which helps align the glass tube with the hole in the cathode.

Argon flows through the cathode at 150 standard cubic centimeters per minute (scm) and, upon exiting the cathode, is mixed with a second argon flow at 450 scm to dilute the aerosol stream and limit agglomeration. The combined gas stream passes through the glass capillary and flows directly into the aerosol inlet of a nano-RDMA. This configuration allows particle size analysis *in situ* so that oxidation and other forms of contamination do not obfuscate particle size. The nano-RDMA instrument has been designed and calibrated to detect nanoparticles in the 1 nm size range.[7]

For comparison, an atmospheric pressure high-voltage arc discharge was constructed to interface with the nano-RDMA, as shown in figure 5.1b. Two OFHC

copper electrodes were inserted in a quartz cross (O. D. \approx 12.5 mm) and were sealed in place using O-rings. The cathode (grounded electrode) consisted of a flat surface while the anode (positively biased) was tapered to a point to reduce the electric field required to ignite the discharge. The arc was maintained with a high voltage power supply (Spellman X2094), connected to the electrodes in series with a current limiting power resistor (10 k Ω). The electrode gap spacing was fixed at 1 mm so that the voltage drop across the electrodes was approximately equal to the MHC discharge voltage drop. Comparisons between the two discharges were made at the same current and similar voltage drops across the plasma volume. A cross-flow of argon at 600 sccm was used to sweep the particles from the arc region into the nano-RDMA.

5.3. Results and Discussion

Both the microdischarge and the arc discharge produce neutral as well as charged nanoparticles of both charge polarities. The corresponding size distributions are presented in figures 5.2 and 5.3. These distributions are plotted in terms of absolute value of current measured with the faraday cup electrometer and the actual particle size and not in terms of mobility diameter.[8]

Fitting of the positively charged particle distributions with two log-normal distributions results in geometric mean mobility diameters of approximately 0.5 and 0.7 nm and geometric standard deviations of 1.1 and 1.2, respectively. The standard deviation value of the larger particle size is suggestive that the larger particle size is due to agglomeration of the smaller particles. Comparing the low and high current cases shown (and intermediate cases, not shown), the distributions remained similar in size, dispersity, and number concentration for a wide range of discharge currents (5 to 20 mA).

Consistent with the particle size regime, significantly fewer negatively charged particles were measured. Fitting of their distributions resulted in geometric means and geometric standard deviations identical to those for the positively charged particles produced at similar currents. Changes in the distributions and particle densities with discharge current were only slight. Unlike the positively charged particles, however, the second peak of the bimodal distribution was smaller than the first peak for all discharge currents. This observation may indicate that particle agglomeration occurs mainly in the discharge where charging dynamics can still influence particle polarity. In the absence of electric fields downstream from the microdischarge, we expect that the loss mechanisms are similar for both polarities.

It is important to note that these measured distributions represent a lower bound on particle concentration, as neutral particles are not counted. Furthermore, both charged and neutral particles may be lost to the walls by diffusion, electrophoresis, or thermophoresis, while in transit to the nano-RDMA. The exact concentration of particles produced in the microdischarge could not be measured.

The sputtered particles produced in the high-voltage arc discharge were different from those produced in the microdischarge, even when they both operate at atmospheric pressure and similar power and current. Interestingly, the particle size distributions for the arc discharge can be fit with a double lognormal distribution and the resulting geometric mean and geometric standard deviations are almost identical to the MHC discharge. Unlike in the MHC discharge distributions, however, the second peak grows significantly with current for both types of charged particles. While not shown, it was found that increasing the current beyond 30 mA produced particles significantly larger

than 1 nm and that the mean size continued to increase with current. The increase in particle size was attributed to a higher density of sputtered atoms produced in the arc discharge as the arc expands over the cathode surface. While not directly observable, a similar expansion in the plasma volume was believed not to occur in the microdischarge.

It was also observed that the arc produces a lower number of negatively charged particles than the microdischarge, although the positively charged particle numbers were similar for the two discharges operating under similar conditions. We speculate that this difference was indicative of the physical mechanism responsible for sustaining the microdischarge. As a result of the hollow cathode effect, the electrons in the microplasma were radially confined inside of the cathode where they undergo Pendel oscillations due to the radial electric field. The directional oscillation and a higher electron density due to confinement should increase the probability of electron attachment to clusters produced in the microdischarge. Alternatively, the larger number of negatively charged particles might indicate a lower neutral gas temperature in the MHC discharge as compared to the arc discharge. A higher gas temperature in the arc would increase thermionic emission of electrons from the particle, thereby reducing the fraction of the particles charged negatively. We have not attempted to measure neutral gas temperatures in these discharges.

Cathode sputtering in a microplasma is sufficiently generic that it should be applicable to different capillary materials. Though not shown in this section, high purity foils, fashioned into a capillary using a narrow diameter tungsten wire as a template, could be used for generic particle production. Sputtering was observed for gold, silver, platinum, zinc, palladium, vanadium, and molybdenum. Among all metals tried, a

significant increase in sputtered particle concentration was observed only for zinc with increasing discharge current.

5.4. Summary

Cathode sputtering in a microdischarge was shown to produce bimodal distributions of extremely small nanoparticles (diameters of ~ 0.5 and 0.7 nm). These distributions were distinct from those obtained using an atmospheric high-voltage arc discharge, with fewer negatively charged particles in the latter. Cathode sputtering in a microdischarge can be used for the production of generic nanoparticles by changing the cathode capillary.

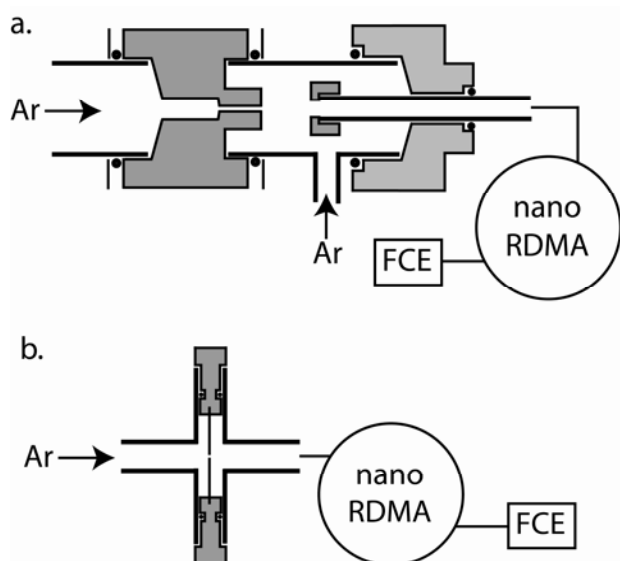


Figure 5.1. Schematic of Sputtering Discharges.

5.1a. Schematic of the MHC discharge and DMA set up used for *in situ* measurements of cathode sputtering. **5.1b.** Schematic of the arc discharge used for *in situ* measurements of sputtered particle size.

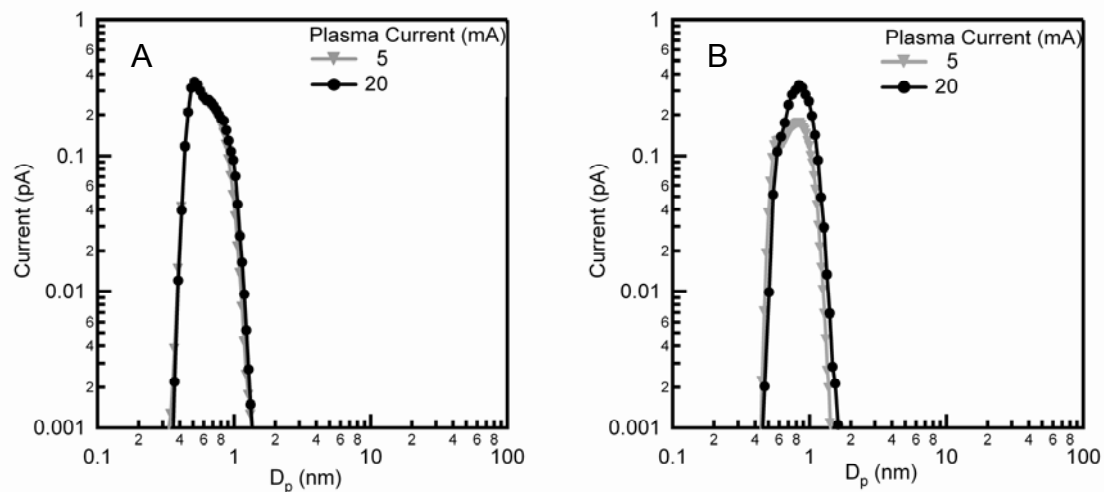


Figure 5.2. Size Distributions of Positively Charged Particles.

Size distributions of positively particles produced in (A) a microhollow cathode discharge (geometry 5.1a) and (B) an arc discharge (geometry 5.1b) operated at 1 atm in argon gas.

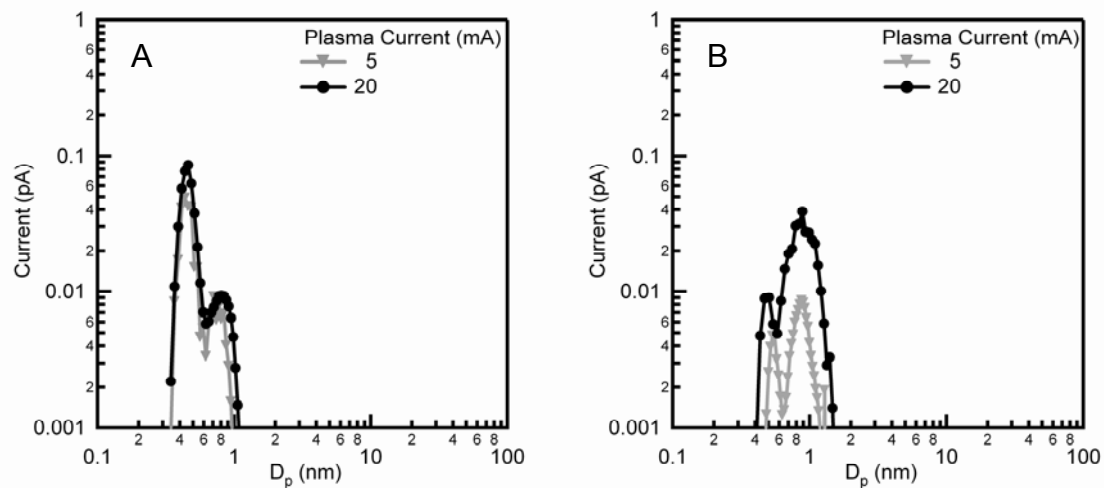


Figure 5.3. Distribution of Negative Charged Particles.

Size distributions of negatively charged particles produced in (A) a microhollow cathode discharge and (B) a high-voltage arc discharge operated at 1 atm in argon.

References

1. S. Rossnagel, and J. Hopwood, *Journal of Vacuum Science & Technology B: Microelectronics and Nanometer Structures*, **12**, 449, 1994.
2. J. J. Cole, E.-C. Lin, C. R. Barry, and H. O. Jacobs, *Applied Physics Letters*, **95**, 113101, 2009.
3. M. A. Lieberman, and A. J. Lichtenberg, *Principles of Plasma Discharges and Materials Processing*. (Wiley-Interscience, Hoboken, NJ, ed. Second, 2005).
4. R. M. Sankaran, and K. P. Giapis, *Journal of Applied Physics*, **92**, 2406, 2002.
5. R. Sankaran, D. Holunga, R. Flagan, and K. Giapis, *Nano Letters*, **5**, 537, 2005.
6. K. Becker, K. Schoenbach, and J. Eden, *Journal of Physics-London-D Applied Physics*, **39**, 55, 2006.
7. N. Brunelli, R. Flagan, and K. Giapis, *Aerosol Science and Technology*, **43**, 53, 2008.
8. H. Tammet, *Journal of Aerosol Science*, **26**, 459, 1995.

Chapter 6: Microdischarge Synthesis of Fe Nanoparticles for Diameter-Controlled Growth of Carbon Nanotubes

6.1. Introduction

Nanometer-sized materials represent the future building blocks of nanoscale structures and often exhibit novel properties. These novel properties often are size dependent due to quantum effects. In particular, these properties have been increasingly explored for carbon nanotubes (CNTs).[1-3] Tseng and co-workers have shown that the CNT diameter affects the on- and off-state currents in CNT transistors.[4] Theoretically, Kutana and Giapis demonstrated that the mechanical properties of CNTs are size dependent.[5] Accordingly, several studies have focused on the synthesis of CNTs with a narrow size distribution.[6-10]

Dai and co-workers reported CNT growth by chemical vapor deposition (CVD) from iron oxide nanoparticles derived from artificial ferritin.[9] Discrete iron oxide nanoparticles with an average diameter of 1.9 and 3.7 nm were obtained by placing a different number of iron atoms into the core of apoferritin. These particles were utilized subsequently to grow CNTs with mean diameters of 1.5 and 3.0 nm, respectively. Beyond establishing a correlation between particle and nanotube size, the size dispersity of the nanoparticle and nanotube were found to be similar as well. This correspondence between nanoparticle and nanotube size dispersity was confirmed using polyaminoamine dendrimers to limit the nanoparticle size dispersity. As hypothesized, the narrower

particle size distribution resulted in tighter control over the CNT diameter distribution.[7] Beyond this limited range, the size correlation between CNT and nanoparticle diameter was extended to the synthesis of CNTs in the range of 3 to 13 nm.[6]

In these studies, the nanotube diameter was measured with either AFM or TEM to be smaller than the average nanoparticle diameter from which they grow. While the correlation provides a practical criterion for controlling the nanotube size, the actual nanoparticle size before and during nanotube growth could be quite different. In a typical CNT growth, a strongly reducing environment is used and should reduce the oxidized nanoparticle size since above a temperature of 750 K, Fe_2O_3 is reduced to Fe in the presence of hydrogen.[11] While measuring the metal nanoparticle size without oxidation is difficult using AFM and TEM, we present preoxidation size measurements of iron nanoparticles produced in an atmospheric-pressure microdischarge. To provide a size correlation between the nanoparticle and the CNT, we further show the resulting nanotube diameter distribution and the nanoparticle size after growth.

6.2. Experimental Method

The iron nanoparticle synthesis strategy originates from a previous report^[12] in which silicon nanoparticles with an average diameter of 1.6 nm were synthesized using a hollow cathode microdischarge. Exchanging the argon stream containing the silane precursor with an ultra-high purity (UHP) argon stream that flows over ferrocene powder allowed the same experimental setup to be used to generate Fe nanoparticles, as depicted in figure 6.1. Ferrocene powder (>98% pure) was used as the Fe source since it sublimates at room temperature with a vapor pressure of 12 mTorr.[13] This vapor pressure is high enough to generate nanoparticles in the microdischarge yet sufficiently low to do so

without clogging the micro-hollow cathode (I. D. $\approx 180 \mu\text{m}$). The ferrocene concentration was controlled via dilution of the ferrocene-saturated UHP argon stream with a second UHP argon stream. The relative flow rates of these two streams were adjusted to vary the ferrocene concentration in the gas mixture, while maintaining a combined flow rate of 150 standard cubic centimeters per minute (scm). All ferrocene concentrations were calculated assuming that the gas stream flowing over the ferrocene was saturated.

This gas mixture was passed through a stainless steel capillary tube that served as the cathode of a direct current microdischarge. The discharge formed inside of the stainless steel capillary tube with an afterglow extending to a second grounded metal tube (anode, I. D. $\approx 2 \text{ mm}$). The electrodes were separated by a gap of 1.5 mm and were sealed inside a quartz tube using UltraTorr fittings (0.5 inch). A sheath flow of Ar was combined with the particle stream in the afterglow region of the microdischarge to prevent particle coagulation and to limit particle loss to the walls. The typical voltage and current used to sustain the discharge were -180 V and 7.5 mA , respectively. The microdischarge was operated at a pressure slightly above atmospheric averting the need for vacuum pumps. The spatially confined microdischarge served as a short residence time reactor, where the sublimed precursor was decomposed by electron impact collisions and rapid gas heating. Particle nucleation and growth in the discharge is believed to be abruptly terminated once the particles are swept out of the discharge region by the flow.

The continuous stream of Fe nanoparticles thus produced was monitored *in situ* for particle size distribution using a newly developed radial differential mobility analyzer (nano-RDMA), which was calibrated using electrospray of quaternary amines.[14] The

nano-RDMA was operated in stepping mode using a 10 standard liters per minute sheath flow, which were the same conditions used to calibrate the instrument.

Alternative to size measurement, nanoparticles were collected thermophoretically in a stagnation-point-flow geometry over a cleaned Si wafer (8 mm x 8 mm with 500 nm thermal SiO₂) for both *ex situ* particle sizing and nanotube growth. The thermophoretic collector consisted of a round upper plate heated to ~200°C and a lower substrate holder, cooled using a mixture of dry ice and acetone. Although some of the particles were charged and electrostatic collection was possible, thermophoretic deposition was chosen over electrostatic precipitation so that the fraction collected was not influenced by the charge distribution on the aerosol. Once collected, the substrates were stored under nitrogen in a dessicator until commencing CNT growth to limit oxidation and water absorption.

The nanoparticle-decorated Si substrates were used to grow CNTs through a chemical vapor deposition (CVD), as described previously.[15] The substrates were placed in a tube furnace and heated to 900°C while under a flow of argon (500 sccm) and allowed to equilibrate at the elevated temperature for 10 minutes. Hydrogen (100 sccm) was added to the argon flow for 10 minutes to reduce the nanoparticles that have oxidized. Subsequently, methane was added at 1000 sccm to the other two flows for 7 minutes to generate CNTs. To ensure few defects, the hydrogen and argon flow were continued for another 10 minutes. Finally, the furnace was cooled down under an argon flow to room temperature to prevent oxidative degradation of the nanotubes.

These substrates were imaged with an atomic force microscope (AFM) (Digital Instruments with a Nanoscope IV controller) before and after carbon nanotube growth. Multiple images ($2\ \mu\text{m} \times 2\ \mu\text{m}$ in size) of the wafers were captured in tapping mode to permit statistical analysis of the carbon nanotube diameters. As the width of features represents a convolution of the tip and the actual nanoparticle size, the measured height above the substrate was recorded as the diameter of the nanotube or particle.

6.3. Results and Discussion

The Fe nanoparticle size distributions measured with the nano-RDMA indicated that mean particle size and the breadth of the distribution increased with the ferrocene concentration, as shown in figure 6.2. Since these measurements are made *in situ*, these diameters pertain to the unoxidized nanoparticle. Fitting the obtained distributions to a log-normal function provided the geometric mean particle diameter (D_g) and standard geometric deviation (σ_g).

For the lower concentrations investigated, the particle size was narrowly distributed ($\sigma_g < 1.2$), as desired for tight control over the resulting nanotube diameters. Above 5 ppm, the large σ_g values ($\sigma_g > 1.3$) were indicative of particle agglomeration, which causes the measured particle size to appear larger than their actual size. Based on these values, it appears that the limited residence time of the microdischarge hindered nanoparticle growth beyond 3.5 nm. While increasing the cathode diameter would increase the residence time, the intense microdischarge would not fill the entire volume of the larger cathode,[16] resulting in a residence time distribution that would not be appropriate for correlating nanoparticle size to nanotube diameter.

The nano-RDMA data also demonstrated that the particle number density increased with ferrocene concentration. Accordingly, different nanoparticle densities were observed in the AFM images of the wafers after five minutes of thermophoretic deposition. While increasing the deposition time correspondingly increased the nanoparticle density, sparse nanoparticle coverage was desired to limit surface diffusion of particles, to avoid particle sintering during nanotube growth, and to ensure minimal overlap between nanotubes. In addition to observing nanoparticle density variation, the AFM images corroborated the size measured using the nano-RDMA, with the AFM measured average size appearing slightly larger than the nano-RDMA size likely due to environmental oxidation.

Using the nanoparticle coated samples, nanotubes were grown as the representative images in figure 6.3A,B demonstrate, where the ferrocene concentration used for nanoparticle synthesis was 1 and 5 ppm, respectively. The nanotubes shown in figure 6.3B exhibit more color contrast (i.e., topographical height variation) compared to those in figure 6.3A, which indicates that the diameters of the nanotubes are larger for the larger nanoparticles. Additionally, the inset in figure 6.3A appears to depict a nanoparticle at the end of the nanotube, confirming the catalytic nature of the particle.

To obtain statistical information, height measurements of more than 100 individual CNTs were made for each concentration. The distribution of nanotube heights for five different ferrocene concentrations are shown in figure 6.4 with the corresponding size distribution parameters listed in table 6.1. The average CNT diameter increases with the ferrocene concentration from 1 to 5 ppm with standard deviations around 0.77 to 0.85 (values comparable to other reports).[17-20] The average CNT

diameter was found to be larger than the Fe nanoparticle diameter measured using the nano-RDMA. While this correlation is different than previous reports, it has been observed when monitoring nanotube growth *in situ* in an Environmental TEM from a nickel nanoparticle that has been reduced.[21]

Beyond measuring the nanotube size, the nanoparticle size after carbon nanotube growth was recorded as well for particles growing CNTs as well as those that did not catalyze CNT growth for comparison. A compilation of all the size data is shown in figure 6.5 as a function of ferrocene concentration. The size of nanoparticles growing CNTs also increased with ferrocene concentration, but did not remain proportionally larger than the CNT diameter. It is important to note that despite collecting numerous images for the 1 ppm concentration, very few ends of the CNTs were observed in the AFM images and therefore an average size is not presented.

A more interesting trend is observed for those nanoparticles not catalyzing CNT growth. For low ferrocene concentrations (i.e., small nanoparticle size), the nanoparticles not growing CNTs are the same size as those that did. This indicates all nanoparticles experience a similar growth environment and that the methane supply is sufficient to decompose and enlarge all of the particles uniformly. For particles produced with high ferrocene concentrations (i.e., large nanoparticle size), the nanoparticle sizes after growth are more similar to the size of the pre-growth nanoparticle. The observed difference in average size is due to a few particles much larger than the average size. This indicates that methane primarily goes toward CNT growth once CNTs have nucleated on the larger nanoparticles. Also, it confirms that the CNT growth conditions do not result in particle sintering, but rather that a different mechanism is responsible for the observed size

increase. The most obvious route leading to the observed size increase would be the catalytic decomposition of methane on the nanoparticle surface and carbon uptake in the nanoparticle.[22]

While the nanoparticle size after CNT growth is not consistently proportional to the CNT diameter, a clear correlation between the CNT size and the pre-growth nanoparticle size is observed with the CNT size larger by a factor of two over the nano-RDMA measured size. We believe the difference in size between the CNT diameter and the pre-growth nanoparticle size can be explained through examining the growth mechanism. It appears that the reduced Fe nanoparticle initially enlarges due to carbon uptake.[22] After reaching carbon saturation, a nanotube nucleates from the surface.[23] The overall result is a nanotube that is larger than the initial Fe nanoparticle.

6.4. Summary

The use of a microdischarge for the synthesis of Fe nanoparticles with a very narrow size distribution has been demonstrated. Using these particles, we have catalytically grown CNTs and shown that these CNTs have a diameter larger than the unoxidized particle diameter through comparing AFM and nano-RDMA measurements. After CNT growth, we have shown that the particles growing nanotubes appear larger than the CNT diameter. Examining these size distributions, we have shown that the pre-growth particle size shows a clearer correspondence to the CNT average diameter than does the post-growth nanoparticle size.

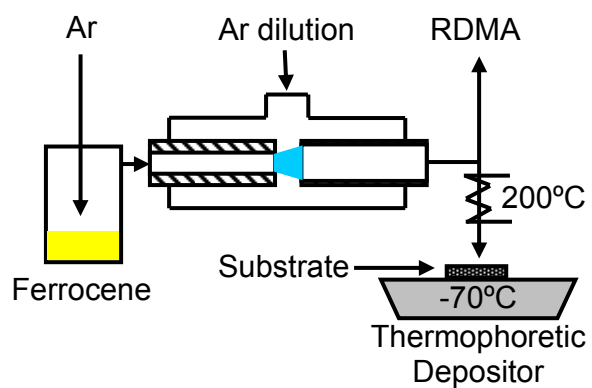


Figure 6.1 Schematic of Microplasma for Fe Nanoparticles.

Schematic of the microplasma and thermophoretic depositor used for Fe nanoparticle synthesis and collection. The heating was achieved with a feedback controlled heat rope whereas the cooling was achieved with a dry ice and acetone bath.

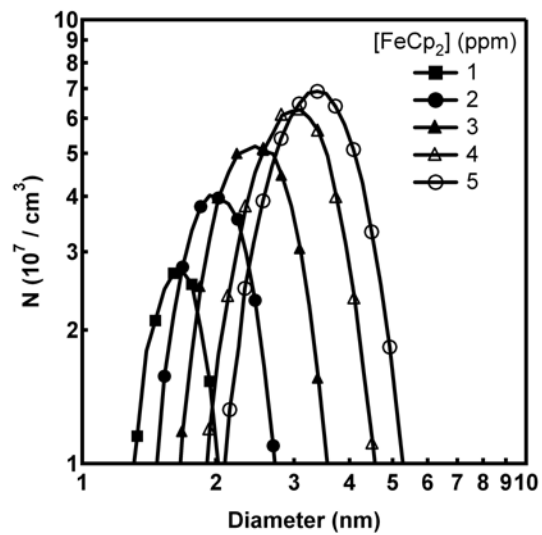


Figure 6.2. Size Distributions of Iron Nanoparticles.

Size distributions of Fe nanoparticles measured *in situ* using a nano-RDMA.

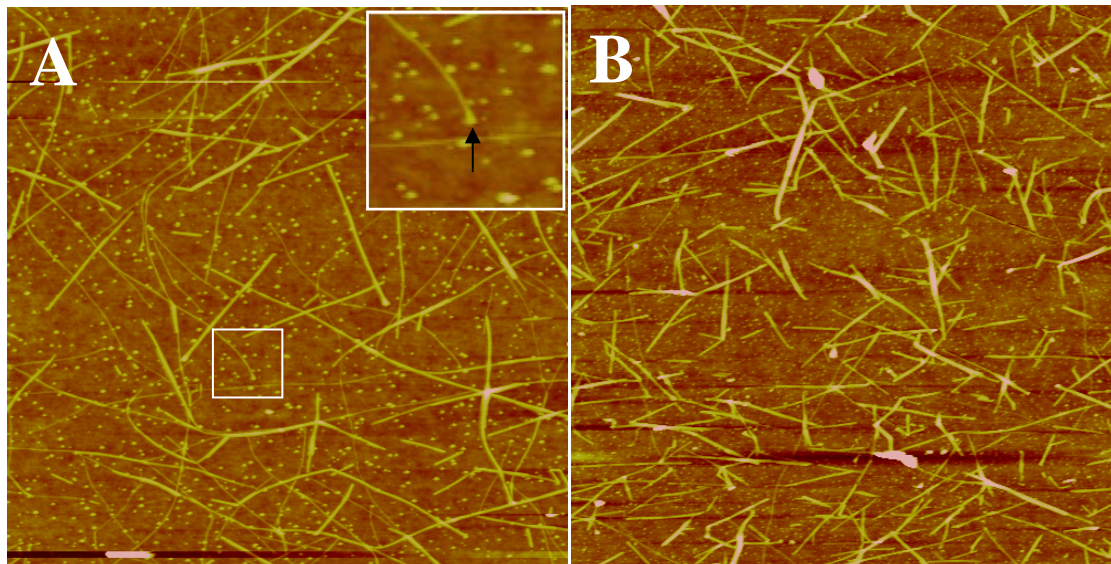


Figure 6.3. AFM Images of CNTs.

$2\ \mu\text{m} \times 2\ \mu\text{m}$ AFM images with ferrocene concentrations of (A) 2 ppm and (B) 5 ppm.

The inset of **3A** is a $300\ \text{nm} \times 300\ \text{nm}$ magnified image.

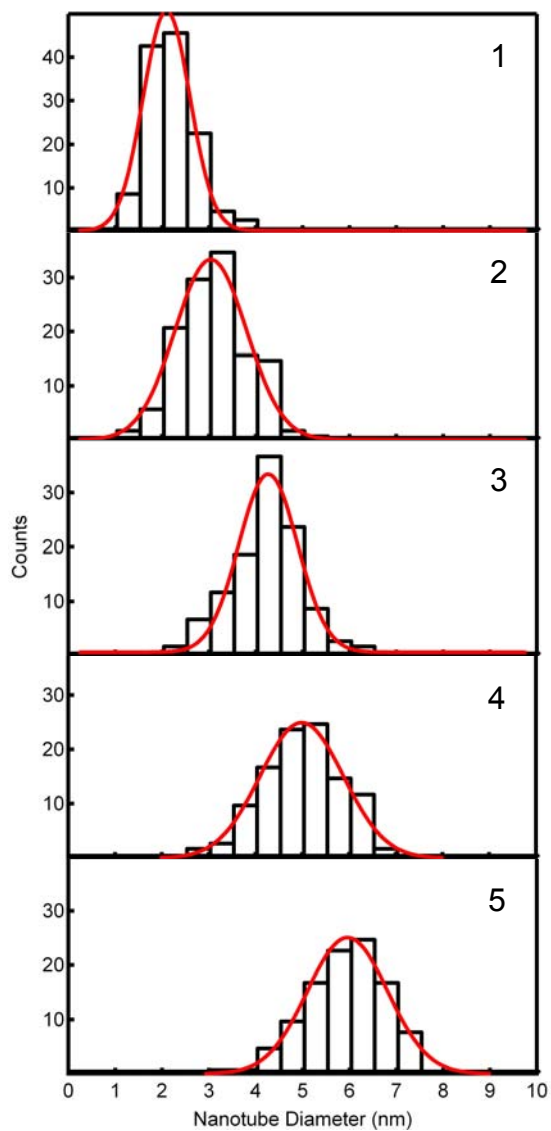


Figure 6.4. Size Distribution of Nanotube Diameters.

Diameter distribution of CNTs obtained from AFM height measurement. The Fe nanoparticles were produced from Ar/ferrocene stream at the indicated ferrocene concentrations in parts per million (ppm).

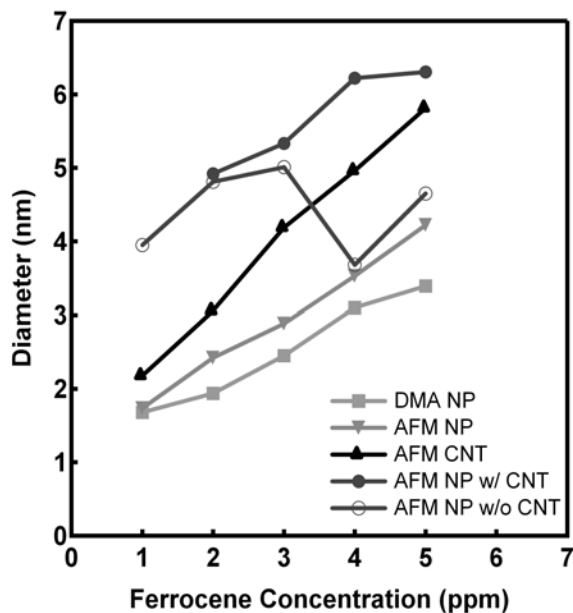


Figure 6.5. Size Variation of Nanotubes and Nanoparticles.

Effect of ferrocene concentration in the Ar/ferrocene stream used to synthesize Fe nanoparticles on the average nanoparticle size before (nano-RDMA and AFM) and after CNT growth. The average CNT diameter measured with AFM is included for reference.

Table 6.1 Measured Particle Size.

Average particle size measured before (with the nano-RDMA and AFM) and after CNT growth (with AFM). The average nanotube diameter is included for reference.

| [Ferrocene] (ppm) | Before | | AFM CNT Size (nm) | After | |
|----------------------|------------------------------|------------------------|-------------------------|-------------------------------|--------------------------------|
| | nano-RDMA NP Size (nm) | AFM NP Size (nm) | | AFM NP Size w/ CNT (nm) | AFM NP Size w/o CNT (nm) |
| 1 | 1.08 | 1.74 | 2.18 | - | 3.95 |
| 2 | 1.34 | 2.42 | 3.06 | 4.92 | 4.81 |
| 3 | 1.85 | 2.89 | 4.19 | 5.33 | 5.01 |
| 4 | 2.50 | 3.53 | 4.96 | 6.22 | 3.68 |
| 5 | 2.79 | 4.22 | 5.82 | 6.30 | 4.85 |

References

1. V. N. Popov, *Mat Sci Eng R*, **43**, 61, Jan 15, 2004.
2. C. N. R. Rao, B. C. Satishkumar, A. Govindaraj, and M. Nath, *Chemphyschem*, **2**, 78, Feb 16, 2001.
3. M. Terrones, *Int Mater Rev*, **49**, 325, Dec, 2004.
4. Y. C. Tseng, K. Phoa, D. Carlton, and J. Bokor, *Nano Lett*, **6**, 1364, 2006.
5. A. Kutana, and K. P. Giapis, *Physical Review Letters*, **97**, 245501, 2006.
6. C. L. Cheung, A. Kurtz, H. Park, and C. M. Lieber, *J. Phys. Chem. B*, **106**, 2429, 2002.
7. H. C. Choi, W. Kim, D. Wang, and H. Dai, *The Journal of Physical Chemistry B*, **106**, 12361, 2002.
8. S. Han, T. Yu, J. Park, B. Koo, J. Joo, T. Hyeon, S. Hong, and J. Im, *Journal of Physical Chemistry B*, **108**, 8091, 2004.
9. Y. Li, W. Kim, Y. Zhang, M. Rolandi, D. Wang, and H. Dai, *Journal of Physical Chemistry B*, **105**, 11424, 2001.
10. Q. Fu, S. Huang, and J. Liu, *J. Phys. Chem. B*, **108**, 6124, 2004.
11. O. J. Wimmers, P. Arnoldy, and J. A. Moulijn, *The Journal of Physical Chemistry*, **90**, 1331, 1986.
12. R. M. Sankaran, D. Holunga, R. C. Flagan, and K. P. Giapis, *Nano Lett*, **5**, 531, 2005.
13. L. A. Torres-Gomez, G. Barriero-Rodriguez, and F. Mendez-Ruiz, *Thermochimica Acta*, **124**, 179, 1988.

14. N. A. Brunelli, R. C. Flagan, and K. P. Giapis, *Submitted to Aerosol Science and Technology.*, 2008.
15. L. A. Wade, I. R. Shapiro, Z. Y. Ma, S. R. Quake, and C. P. Collier, *Nano Lett.*, **4**, 725, Apr, 2004.
16. R. M. Sankaran, *Journal of Applied Physics*, **92**, 2406, 2002.
17. H. C. Choi, W. Kim, D. W. Wang, and H. J. Dai, *J. Phys. Chem. B*, **106**, 12361, Dec, 2002.
18. C. L. Cheung, A. Kurtz, H. Park, and C. M. Lieber, *J. Phys. Chem. B*, **106**, 2429, Mar, 2002.
19. Y. M. Li, W. Kim, Y. G. Zhang, M. Rolandi, D. W. Wang, and H. J. Dai, *J. Phys. Chem. B*, **105**, 11424, Nov 22, 2001.
20. Q. Fu, S. M. Huang, and J. Liu, *J. Phys. Chem. B*, **108**, 6124, May, 2004.
21. R. Sharma, P. Rez, M. M. J. Treacy, and S. J. Stuart, *Journal of Electron Microscopy*, **54**, 231, 2005.
22. A. R. Harutyunyan, T. Tokune, E. Mora, J. W. Yoo, and A. J. Epstein, *Journal of Applied Physics*, **100**, 044321, 2006.
23. W. H. Chiang, and R. M. Sankaran, *Applied Physics Letters*, **91**, 121503, 2007.

Chapter 7: Instrument Calibration Using Tandem Differential Mobility Analysis with a Microplasma Source

“Measure what is measurable, and make measurable what is not so.” — Galileo

Galilei

7.1. Introduction

Measurements of ambient aerosols have demonstrated the abundance of nanoparticles in the atmosphere.^[1] Small particles accumulate to a critical concentration and begin to agglomerate, forming larger particles with a broad distribution of sizes.^[2] The particle size and concentration are important factors in determining the aerosol dynamics.^[3]

The primary instrument to measure particle size distributions is the differential mobility analyzer (DMA). The device classifies particles based on small differences in mobility (Z_P) of charged particles between two electrodes with a fixed spacing (b) in an electric field ($E = V/b$). A particle-laden stream (Q_a) enters the classifying region through one electrode where it is combined with a laminar sheath flow (Q_{sh}). The electric field forces the particles through the particle-free sheath flow toward the other electrode. After a fixed distance (l), the flow is divided unequally with a portion exiting (Q_s ; i.e., the sample flow) the electrode opposite of the aerosol entrance. This stream is directed to a particle counting device to measure concentration. The remaining flow is exhausted as the excess flow (Q_{ex}).

The applied voltage for a given device determines the mean mobility (Z_p^*) of the transmitted particles. Particles with a lower mobility than the mean will be removed with the excess flow whereas particles with a higher mobility will be deposited onto the electrode. This implies that a range of particle mobilities will be transmitted around the mean mobility selected.

The performance of the DMA is measured with two parameters: transmission efficiency (η) and resolution (R). Transmission efficiency is defined as the fraction of charged particles entering the device with a fixed mobility that emerge through the sample outlet with the appropriate voltage applied. A transmission lower than unity is caused by particle losses in the different regions of the device. Resolution is defined as

$$R = \frac{Z_p^*}{\Delta Z_{FWHM}}, \quad (7.1)$$

where ΔZ_{FWHM} is the full width at half maximum of the distribution. The theoretical maximum resolution is Q_{sh} / Q_a , but particle diffusion and axial asymmetry in the sizing region decrease the measurable resolution. Forehand knowledge of resolution and transmission allows data correction, enabling a more accurate assessment of aerosol particle size distribution.

A new DMA was recently reported that could measure particles in the 1 to 12.5 nm size range.^[4] The instrument resolution for the mobility diameter range of 1 to 2 nm through electrospray of molecular ions, as reported previously. The instrument achieved considerable resolution over this range, but additional calibration data is needed to determine the transmission and the resolution of the device for the remainder of the size range.

A standard method to calibrate a DMA involves using two instruments in series in a configuration known as the Tandem DMA (TDMA).^[5] A source produces particles that are passed to the first DMA. The first DMA is operated with a constant applied voltage, passing a narrow mobility distribution of particles to either a particle counter or a second DMA. The particle counter records the particle concentration (N_I) upstream of the second DMA before directing the flow through the second DMA. The second DMA is operated in voltage stepping mode, collecting a particle size distribution that reflects the combined resolutions of the two devices. As particle concentration (N_I) is not measured during the voltage scans of the second DMA, the source must be capable of producing a stable concentration of a fixed size distribution.

Calibration using the TDMA arrangement is difficult in the 2 to 4 nm size range due to the lack of a stable source. Electrospray of molecular ions have been successfully employed below 2 nm to determine instrument resolution,^[6] but becomes more difficult above 2 nm as the particles will tend to attain multiple charges. A source aerosolizing polystyrene beads work well above 10 nm, but a well-characterized sample is not currently available below 5 nm. In this section, a recently developed aerosol synthesis technique based on a microplasma is examined as a possible source. It has been demonstrated the microplasma can operate stably for extended periods of time and produce a high concentration of particles in the 1 to 5 nm size range, and therefore should be suitable as a particle source.

7.2. Experimental Method

The microplasma source was combined with two nano-RDMAs in the TDMA arrangement, as shown in figure 7.1. The operation of a single microplasma has been

discussed previously.^[7] Briefly, this system consisted of a stainless steel capillary (I. D. $\approx 180 \mu\text{m}$) and a stainless steel tube (O. D. $\approx 3 \text{ mm}$) between which the microplasma is maintained. Through the capillary, a stream is passed that contains an ultrahigh purity (UHP) argon stream and a silane (50 parts per million (ppm)) in argon mixture stream at a combined flow rate of 150 standard cubic centimeters per minute (sccm), as controlled with two mass flow controllers (MFCs). The electrode assembly is sealed inside a glass tube (O. D. $\approx 12 \text{ mm}$) using standard Swagelok and UltraTorr fittings. A third MFC flows a sheath gas of UHP argon at 450 sccm that is combined with the first stream in the afterglow portion of the microplasma. This combined flow (total of 600 sccm) is introduced into the aerosol inlet of the nano-RDMA.

As the particle size produced from the microplasma is sensitive to pressure variations, the flows in the system must be precisely matched. This means that the sheath (Q_{sh}) and excess (Q_{ex}) flow rates of each nano-RDMA are precisely matched using a Gillibrator. The aerosol inlet (Q_a) and sample flow (Q_s) rates are matched as well. Matching the inlet and sampling flow rate is accomplished using a leak valve backed with a diaphragm pump, permitting flow rate matching to within $\pm 1 \text{ sccm}$.

All particle size scans were made in the voltage stepping mode. This process involved setting the voltage across the DMA electrodes and measuring the current produced from the charged particles that were transmitted through the DMA. The current was measured with a home-built Faraday cup electrometer sensitive to $\pm 1 \text{ fA}$. To establish steady-state current, the voltage was set followed by a two second delay before the current was measured for one second. Rather than using a single electrometer, two

matched electrometers were used to minimize transmission lines and to allow fast switching between the first and second nano-RDMA.

A computer was used to scan the voltage applied to the first device and to record the current measured with the first electrometer. After three consecutive measurements, the size-selected particle-laden flow was directed toward the second nano-RDMA. A fixed voltage was applied to the first nano-RDMA while the computer scanned the voltage applied to the second nano-RDMA while the current measured with the second electrometer was recorded. The voltage on first device was systematically varied to cover the broadest range of voltages that could be spanned while maintaining adequate particle concentration delivered to the second electrometer. After scanning through the voltage range, the flow was re-directed to the first electrometer and the scans were recorded, allowing comparison of the size distributions before and after. If the before and after distributions did not agree, the sequence was repeated. Generally, the before and after distributions agreed except if size distributions were collected shortly after the microplasma was first struck. If the microplasma was allowed to equilibrate for 30 minutes after striking the microplasma, the size distributions were quite stable. This procedure was repeated for four different silane concentrations (i.e., 1, 2, 3, and 4 ppm). Changing the precursor concentration allowed probing of different voltage ranges with some overlap as well as different size distribution polydispersities.

The measured size distributions were analyzed to determine resolution and transmission. First, the concentration data were normalized (N_2/N_1) and plotted against the normalized mobility (Z_2/Z_1). The resulting data were analyzed using the MatLab function *nlinfit*.

7.3. Results and Discussion

The first calibration experiments used nano-RDMA 2 in the first position and nano-RDMA 1 in the second position. The mobility distribution was measured with the first nano-RDMA, as shown in figure 7.2. The mobility distribution before and after analysis with the second nano-RDMA agreed well with one another, and the measured distribution could be fit with a lognormal distribution.^[8] The parameters of the lognormal fits are listed in table 7.1. The mean inverse mobility increased (i.e., size increased) and the distribution broadened with increasing silane concentration, as described previously (chapter 4).

These parameters are not the actual characteristics of the mobility distribution produced with the microplasma. The data represents the convolution of the mobility distribution (f_{LN}) with the Stolzenburg transfer function of the nano-RDMA (Ω_{Stolz}):

$$N_1(Z_P) = \eta_1 f_{LN}(1/Z_P^*, N, 1/Z_{Pg}, \sigma_g) * \Omega_{Stolz,1}(Z_P, Z_p^*, \sigma_{Stolz}, \beta, \delta_{FR}), \quad (7.2)$$

where η_1 is the transmission efficiency, Z_p^* is the convolution variable, N is the concentration, Z_{Pg} is the geometric mean mobility, σ_g is the geometric standard deviation, Z_P is the mobility, σ_{Stolz} is the Stolzenburg broadening coefficient of the distribution, δ_{FR} is a parameter used to correct for unbalanced flows ($\delta_{FR} = 0$ in this report), and β is the ratio of aerosol to sheath flow (Q_a / Q_{sh}) when $\delta_{FR} = 0$. The lognormal distribution is defined as

$$f_{LN}(1/Z_P^*, N, 1/Z_{Pg}, \sigma_g) = \frac{dN}{d \ln Z_P^*} = \frac{N}{(2\pi)^{1/2} \ln \sigma_g} \exp \left(-\frac{1}{2} \left(\frac{\ln \left(\frac{1/Z_P^*}{1/Z_{Pg}} \right)}{\ln \sigma_g} \right)^2 \right), \quad (7.3)$$

and the transfer function is defined as

$$\Omega_{Stolz}(Z_P, Z_P^*, \sigma_{Stolz}, \beta, \delta_{FR}) = \frac{\sigma_{Stolz}}{\sqrt{2}\beta(1-\delta_{FR})} \left[\begin{array}{l} \varepsilon\left(\frac{Z_P^*/Z_P - (1+\beta)}{\sqrt{2}\sigma_{Stolz}}\right) + \varepsilon\left(\frac{Z_P^*/Z_P - (1-\beta)}{\sqrt{2}\sigma_{Stolz}}\right) \\ - \varepsilon\left(\frac{Z_P^*/Z_P - (1+\beta\delta_{FR})}{\sqrt{2}\sigma_{Stolz}}\right) - \varepsilon\left(\frac{Z_P^*/Z_P - (1-\beta\delta_{FR})}{\sqrt{2}\sigma_{Stolz}}\right) \end{array} \right], \quad (7.4)$$

where

$$\varepsilon(x) = x \cdot \text{erf}(x) + e^{-x^2} / \sqrt{\pi}, \quad (7.5)$$

where $\text{erf}(x)$ is the error function. The Stolzenburg transfer function can be modeled as a lognormal distribution when σ_{Stolz} is not too small:

$$f_{DMA}(Z_P^*, 1, Z_P, \sigma_{g,DMA}) = \frac{1}{(2\pi)^{1/2} \ln \sigma_{g,DMA}} \exp\left(-\frac{1}{2} \left(\frac{\ln(Z_P^*/Z_P)}{\ln \sigma_{g,DMA}}\right)^2\right), \quad (7.6)$$

where $\sigma_{g,DMA}$ is the geometric standard deviation of the distribution. The value of $\sigma_{g,DMA}$ is not the value of σ_{Stolz} .

The analysis to this point is similar to that presented previously.[9-10] One assumption made in this analysis was that the particle distribution was sufficiently broad that the concentration does not change appreciably over the width of Ω_{Stolz} . The microplasma produces a narrow size distribution that may not be sufficiently broad to justify this assumption. The assumption is not necessary provided that σ_{Stolz} is not small. The solution to the convolution for a single modal distribution takes the form:

$$N_1(Z_P) = \int_0^{\infty} f_{LN}(1/Z_P^*, N, 1/Z_{Pg}, \sigma_g) f_{DMA}(Z_P^*, \eta, Z_P, \sigma_{g,DMA}) dZ_P^*, \quad (7.7)$$

$$N_1(Z_P) = \frac{\eta N^*}{\sqrt{2\pi} \sqrt{\ln^2 \sigma_g + \ln^2 \sigma_{g,DMA}}} \exp\left(-\frac{1}{2} \left(\frac{\ln(1/Z_P) - \ln(1/Z_{Pg})}{\sqrt{\ln^2 \sigma_g + \ln^2 \sigma_{g,DMA}}}\right)^2\right), \quad (7.8)$$

$$N_1(Z_P) = f_{LN}\left(1/Z_P, N^*, 1/Z_{Pg}, \exp\left(\sqrt{\ln^2 \sigma_g + \ln^2 \sigma_{g,DMA}}\right)\right). \quad (7.9)$$

Using this formula, the actual parameters of the mobility distribution can be determined provided that $\sigma_{g,DMA}$ is known. The initial calibration (chapter 2) of the nano-RDMA did not extend into this mobility range, but the approximate value of $\sigma_{g,DMA}$ can be calculated based on the instrument calibration factor ($G = 17.3$).^[4] The extrapolated values of $\sigma_{g,DMA}$ are much smaller than the breadth of the measured mobility distribution. Therefore, the measured mobility distribution is approximately correct provided that the instrument resolution can be extrapolated.

The size distributions measured using the first nano-RDMA can be transmitted to the second nano-RDMA and measured for mobility distribution, as shown in figure 7.3. The mobility distributions represent the convolution of three log-normal distributions:

$$N_2(Z_P) = \int_0^{\infty} f_{LN}(1/Z_P^*, N, 1/Z_{Pg}, \sigma_g) f_{DMA}(Z_P^*, \eta_1, Z_{PDMA1}, \sigma_{g,DMA1}) f_{DMA}(Z_P^*, \eta_2, Z_P, \sigma_{g,DMA2}) dZ_P^*, \quad (7.10)$$

$$N_2(Z_P) = \frac{\eta_1 \eta_2 N^\#}{\sqrt{2\pi} \sqrt{\ln^2 \sigma_{DMA2} + \frac{\ln^2 \sigma_g \ln^2 \sigma_{DMA1}}{\ln^2 \sigma_g + \ln^2 \sigma_{DMA1}}}} \exp \left(-\frac{1}{2} \left(\frac{\left(\ln(Z_P) - \frac{(\ln Z_{Pg} \ln^2 \sigma_{DMA1} + \ln Z_{DMA1} \ln^2 \sigma_g)}{\ln^2 \sigma_g + \ln^2 \sigma_{DMA1}} \right)^2}{\ln^2 \sigma_{DMA2} + \frac{\ln^2 \sigma_g \ln^2 \sigma_{DMA1}}{\ln^2 \sigma_g + \ln^2 \sigma_{DMA1}}} \right) \right), \quad (7.11)$$

$$N_2(Z_P) = f_{LN} \left(Z_P, \eta_1 \eta_2 N^\#, \frac{(\ln Z_{Pg} \ln^2 \sigma_{DMA1} + \ln Z_{DMA1} \ln^2 \sigma_g)}{\ln^2 \sigma_g + \ln^2 \sigma_{DMA1}}, \exp \left(\sqrt{\ln^2 \sigma_{DMA2} + \frac{\ln^2 \sigma_g \ln^2 \sigma_{DMA1}}{\ln^2 \sigma_g + \ln^2 \sigma_{DMA1}}} \right) \right), \quad (7.12)$$

that is also found to be a lognormal distribution. In the limit of $\ln^2 \sigma_g \gg \ln^2 \sigma_{DMA1}$ with $Z_{Pg} \approx Z_{DMA1}$, this expression becomes

$$N_2(Z_P) = f_{LN} \left(Z_P, \eta_1 \eta_2 N^\#, \ln Z_{DMA1}, \exp \left(\sqrt{\ln^2 \sigma_{DMA2} + \ln^2 \sigma_{DMA1}} \right) \right). \quad (7.13)$$

The mobility distributions are narrower than the initial mobility distribution, and contain fewer particles. The decrease in number of particles is expected since particle loss occurs in the nano-RDMA, and can be accounted for with the parameter η_2 . Particle deposition can occur in a few locations due to diffusion to any of the walls or to electrophoresis in the aerosol inlet region.

The distributions measured in the second nano-RDMA are better visualized after normalizing the data, shown in figure 7.4 for silane concentrations of 1 to 4 ppm. The mobility is normalized with respect to mobility selected in the first DMA and the current is normalized with the current measured in the first nano-RDMA. The first observation is that all of the distributions are shifted to lower mobilities (i.e., larger particle sizes). The shift is captured by a parameter $\delta = Z_{DMA2}/Z_{DMA1}$, and is plotted in figure 7.5. It increases with voltage and levels off at a value of 0.96. This shift has been observed in many TDMA measurements, but is not well understood.[11]

The second observation from the normalized data concerns the transmission, and is shown in figure 7.6 for each of the concentrations tested. The fraction transmitted increased with voltage from 0.1 for the low voltage range tested to a value of 0.2 for the high voltage range. The increase in transmission with voltage most likely corresponds to less deposition due to diffusion since smaller particles (transmitted at lower voltages) will diffuse faster than larger particles.

The transmission was approximately constant for the higher voltage range and could correspond to the limiting transmission for this flow rate ratio. Electrophoretic deposition in the aerosol inlet extension region (see chapter 2 for description) most likely

reduces the transmission through the device. If higher transmissions were desired, the aerosol flow rate could be increased or the inlet extension could be lengthened.

The final observation from the normalized data is the resolution, and is shown in figure 7.7. The resolution was determined from fitting the measured distribution using a lognormal function. Assuming the resolution of the first and second nano-RDMA was approximately equal and using the relation found in equation (7.13), the resolution was determined as a function of voltage. The resolution increases with voltage to a maximum of ~ 7.5 . The increase in resolution was expected, but the resolution is lower than expected and observed previously (chapter 2). The resolution measured using molecular ions at a voltage of ~ 150 V was approximately 7. The resolution found using the microplasma at this voltage was ~ 4.2 .

The lower-than-expected resolution indicates that the microplasma is not an ideal calibration source in this configuration. A number of reasons could be responsible for the low resolution, including aspherical particles and space-charge distortion in the DMA.[12-14] Aspherical particles will be transmitted over a larger range of voltages as they are transmitted with a random orientation through the nano-RDMA. Since a DMA measures the average mobility in an electric field, the random orientation will affect the average drag force and consequently the range of voltages over which the particle is transmitted.

Broadening due to space-charge distortion of the electric field is the second possibility. Space-charge effects were determined theoretically to be important for values of $n_o Z \tau$ larger than $22,000 \text{ V}^{-1} \text{ cm}^{-1}$, [12] where n_o is the number concentration at the inlet, Z is the electrophoretic mobility, and τ is the residence time in the device. Given that the

residence time inside of the nano-RDMA (τ) is approximately 25 ms, the measured value of n_o is approximately 10^6 cm^{-3} , and Z is approximately $0.5 \text{ cm}^2 \text{ V}^{-1} \text{ s}^{-1}$, the value calculated for the instrument is $12,500 \text{ V}^{-1} \text{ cm}^{-1}$. Depending upon where the particle losses in the instrument occur, the measured value of n_o could be higher, resulting in space-charge distortion that would cause broadening of the mobility distribution. The calculated values do not indicate space-charge distortion, but the mobility distribution behaves as would be expected for such an effect (i.e., the mobility measured in the second DMA is higher than the mobility set with the first DMA and the distribution is broadened). The effect of space-charge distortion would not be expected in the second nano-RDMA because the lower concentration would limit these effects and not affect the measured size distribution.

7.4. Summary

A microplasma source was demonstrated to operate stably producing a high concentration of nanoparticles over a broad mobility range. The microplasma most likely could not be used as a calibration standard to use in the TDMA since the measured mobility distributions did not indicate a resolution as high as previously measured using molecular ions.

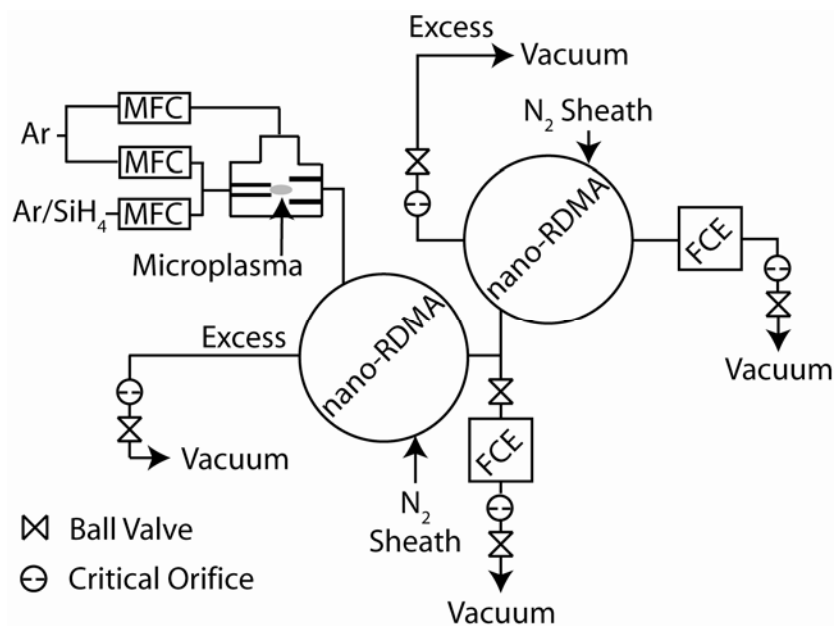


Figure 7.1 Schematic of Tandem DMA.

Schematic of the microplasma and tandem differential mobility analyzer arrangement used to calibrate the nano-RDMA.

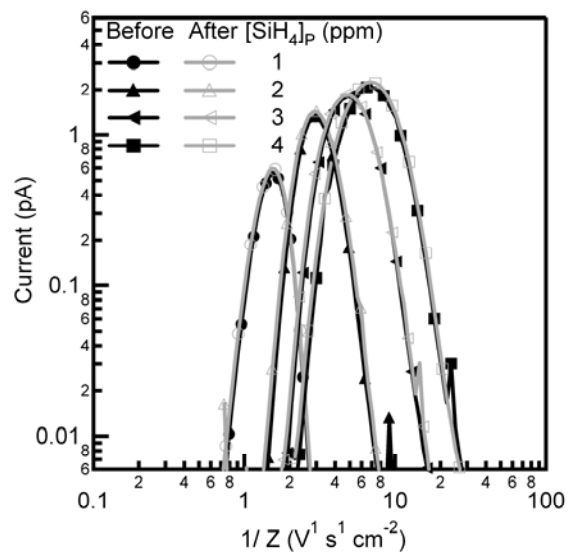


Figure 7.2. Mobility Distribution from First nano-RDMA.

Mobility distribution measured with the first nano-RDMA before and after the TDMA measurement. The microplasma was operated with a current of 7.5 mA and a total flow rate of 600 sccm.

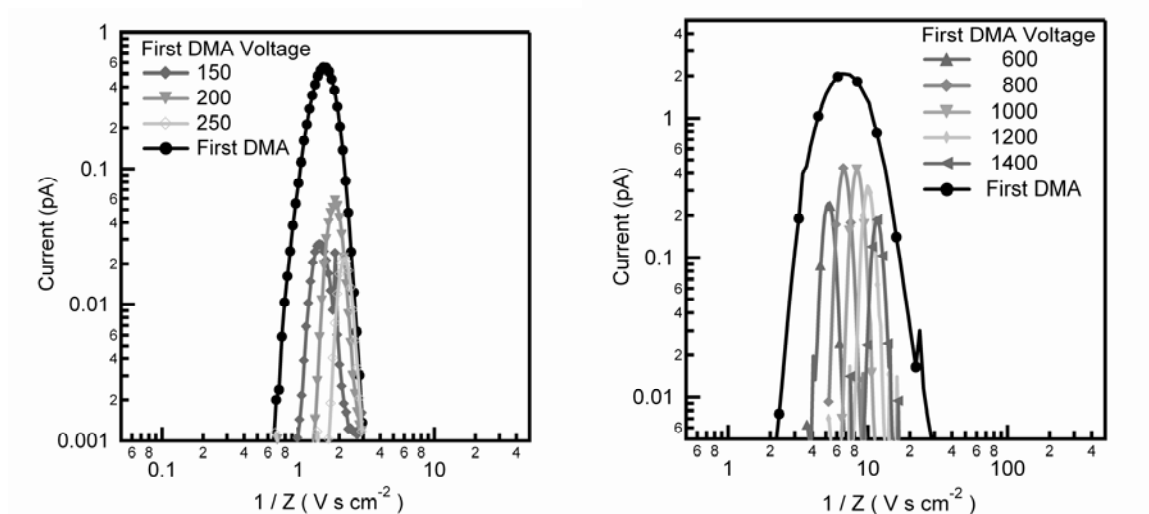


Figure 7.3. TDMA Mobility Distributions.

TDMA mobility distributions measured from the microplasma using silane concentrations of 1 (left) and 4 (right) ppm. The mobility distributions are labeled with the voltage applied to the first nano-RDMA. The mobility distribution from the first nano-RDMA (black circles) is indicated for reference.

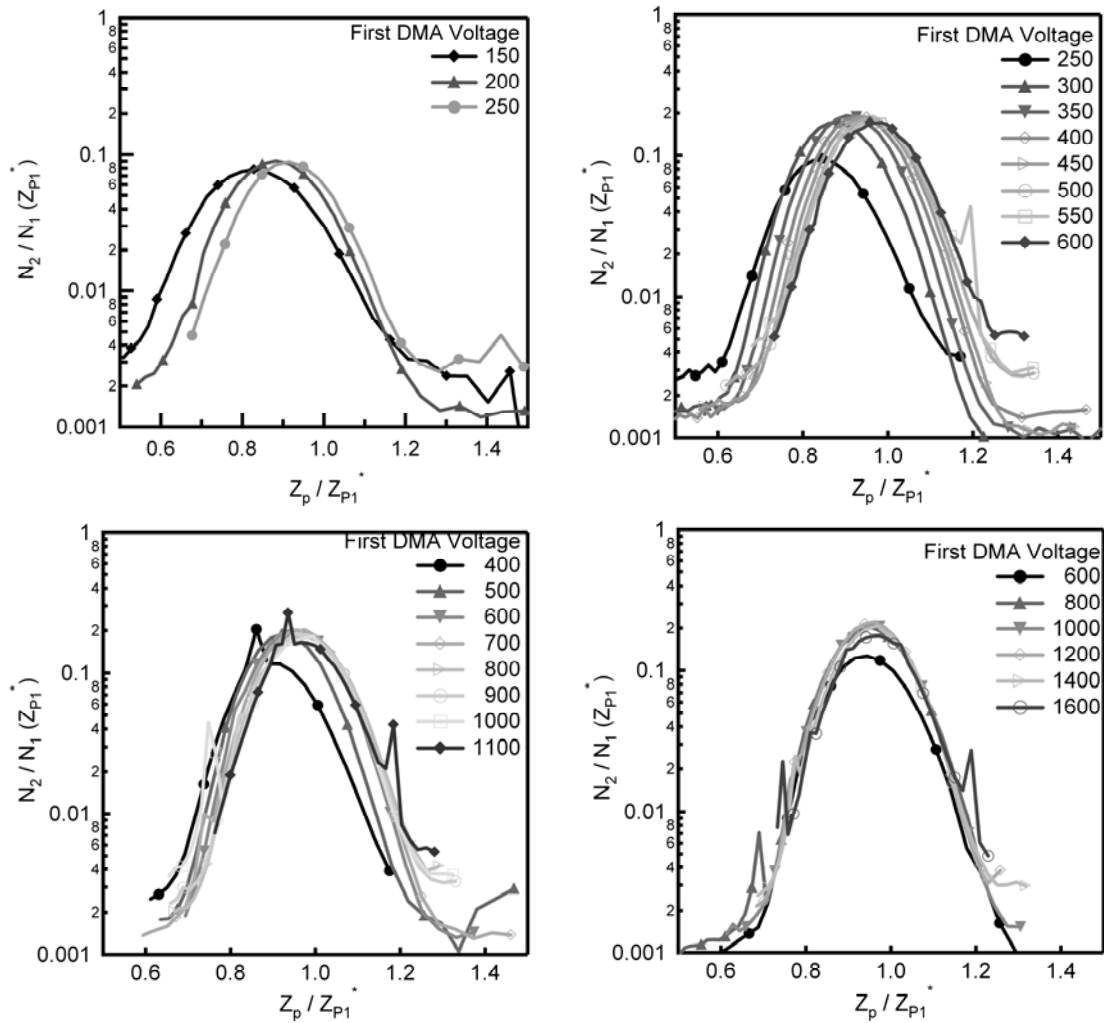


Figure 7.4. Normalized TDMA Mobility Distributions.

Normalized TDMA mobility distributions using silane concentrations of 1 (top left), 2 (top right), 3 (bottom left), and 4 (bottom right) ppm in the microplasma. The concentration data are normalized by the concentration measured with the first nano-RDMA at the set mobility. The mobility data are normalized by the mobility set on the first nano-RDMA.

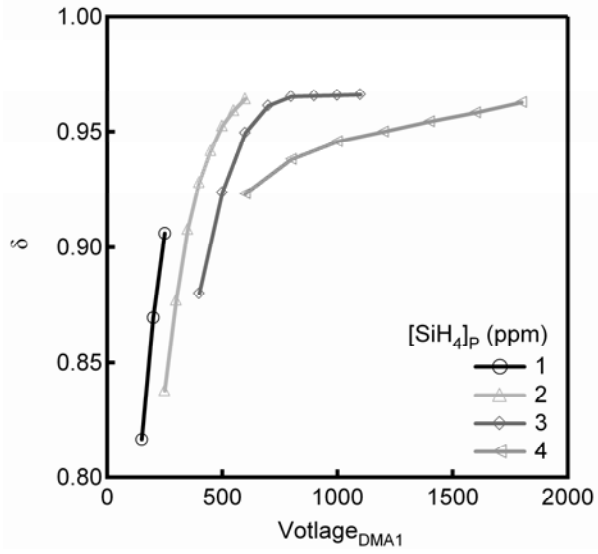


Figure 7.5. Shift of TDMA Mobility Distribution.

The measured shift in the mobility distribution from the expected mobility ($\delta = Z_{DMA2}/Z_{DMA1}$) as a function of voltage.

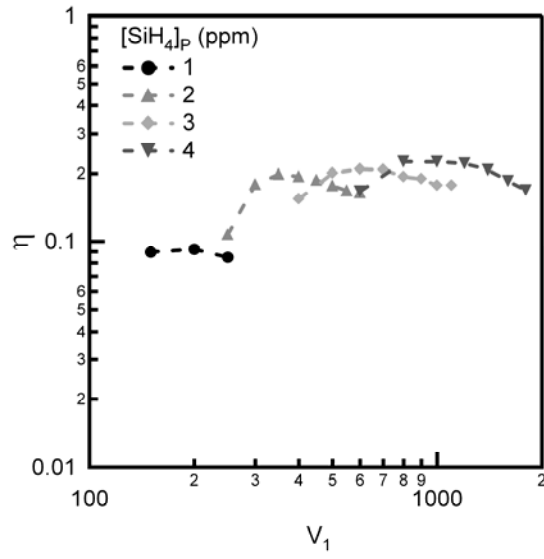


Figure 7.6. Transmission of the nano-RDMA.

The measured transmission (η) of the second nano-RDMA as a function of voltage.

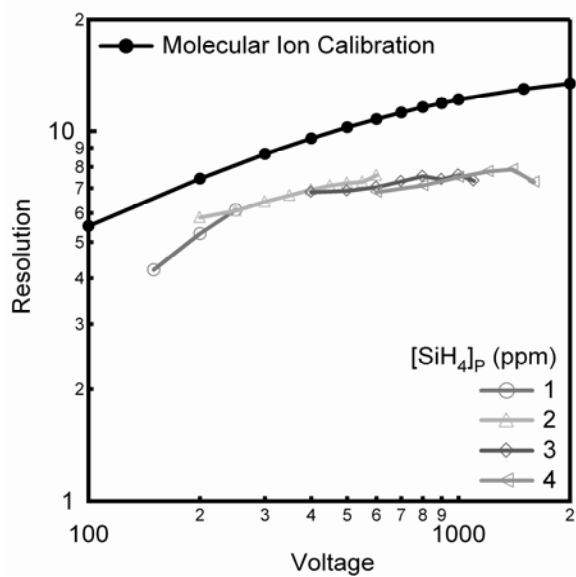


Figure 7.7. Resolution Measured with the Tandem DMA.

The measured resolution from the nano-RDMA as a function of voltage. The resolution measured with the molecular ion is extrapolated into this region.

Table 7.1. Fitting Parameters of First nano-RDMA Mobility Distributions

The fitting parameters of a log-normal distribution for the mobility distributions measured with the first nano-RDMA.

| [SiH ₄] (ppm) | <i>Current</i> (pA) | Z^1 (V s cm ⁻²) | $\ln \sigma$ - | σ_g |
|------------------------------|------------------------|----------------------------------|-------------------|------------|
| 1 | 0.295 ± 0.013 | 1.526 ± 0.009 | 0.204 ± 0.002 | 1.23 |
| 2 | 0.855 ± 0.036 | 2.995 ± 0.013 | 0.245 ± 0.006 | 1.28 |
| 3 | 1.456 ± 0.055 | 4.907 ± 0.030 | 0.321 ± 0.006 | 1.38 |
| 4 | 1.961 ± 0.098 | 6.884 ± 0.021 | 0.393 ± 0.003 | 1.44 |

References

1. P. Winkler, G. Steiner, A. Vrtala, H. Vehkamäki, M. Noppel, K. Lehtinen, G. Reischl, P. Wagner, and M. Kulmala, *Science*, **319**, 1374, 2008.
2. J. Heintzenberg, B. Wehner, and W. Birmili, *Tellus*, **59**, 273, 2007.
3. J. Seinfeld, and S. Pandis, *Atmospheric chemistry and physics*. (John Wiley and Sons, Inc., New York, 1998).
4. N. Brunelli, R. Flagan, and K. Giapis, *Aerosol Science and Technology*, **43**, 53, 2008.
5. W. Birmili, F. Stratmann, A. Wiedensohler, D. Covert, L. Russell, and O. Berg, *Aerosol Science and Technology*, **27**, 215, 1997.
6. S. Ude, and J. Fernandez de la Mora, *Journal of Aerosol Science*, **36**, 1224, 2005.
7. R. Sankaran, D. Holunga, R. Flagan, and K. Giapis, *Nano Letters*, **5**, 537, 2005.
8. L. Kiss, J. Söderlund, G. Niklasson, and C. Granqvist, *Nanostructured Materials*, **12**, 327, 1999.
9. M. Stolzenburg, and P. McMurry, *Aerosol Science and Technology*, **42**, 421, 2008.
10. M. Stolzenburg, University of Minnesota (1988).
11. Y. Kousaka, K. Okuyama, M. Adachi, and T. Mimura, *Journal of Chemical Engineering of Japan*, **19**, 401, 1986.
12. M. Alonso, F. Alguacil, and Y. Kousaka, *Journal of Aerosol Science*, **31**, 233, 2000.
13. M. Alonso, and Y. Kousaka, *Journal of Aerosol Science*, **27**, 1201, 1996.

14. R. P. Camata, H. A. Atwater, and R. C. Flagan, *Journal of Aerosol Science*, **32**, 583, 2001.

Chapter 8: Size Evolution of Annealed Silicon Nanoparticles

8.1. Introduction

Properties of nanoscale materials can differ vastly from the properties of the bulk.^[1] For silicon and other semiconductor materials, size reduction into the single nanometer range leads to novel optical properties as a result of quantum confinement of excitons.^[2] Decreasing the size of silicon nanoparticles to below 4 nm increases the band gap with a concomitant shift in excitonic emission to shorter wavelengths.

In addition to changes in the optical, magnetic, and physical properties, size reduction also affects the nature of the surface. Small particles cannot maintain the low energy surfaces found in the bulk; higher energy facets usually appear. The surface represents a greater fraction of the total particle and may influence some of the same properties that size affects.

For silicon, the surface can be either bare or, as is more typical, terminated with hydrogen or oxygen. Recently, a comparison between bare and hydrogen terminated particles indicated that the bare silicon nanoparticles with a diameter of 6 nm had a lower intensity of emission than hydrogen-terminated particles.^[3] Therefore, hydrogen termination appears to be important for excitonic emission from Si nanoparticles.

At larger surface curvature, hydrogen-terminated Si nanoparticles have been observed to have more silicon trihydride groups present.^[4] Hydrogen in this form is known to desorb at lower temperatures than the dihydride and monohydride form. Given the importance of hydrogen termination, the behavior of hydrogen desorption with particle size is of fundamental importance.

Holm and Roberts^[3] reported recently on hydrogen desorption from Si nanoparticles using an aerosol sizing method to compare particle size before and after thermal treatment of nanoparticles. The method utilized a low-pressure plasma to synthesize a broad distribution of nanoparticles starting with silane as a precursor. A differential mobility analyzer (DMA) was used subsequently to select a narrow slice of the distribution centered at 6 nm. The size-selected distribution was then passed through a furnace, and the resulting particle size distribution was measured in a second DMA. The measured particle size was observed to change a total of ~ 0.32 nm over three temperature ranges: low ($20^{\circ}\text{C} - 300^{\circ}\text{C}$), medium ($300^{\circ}\text{C} - 400^{\circ}\text{C}$), and high ($600^{\circ}\text{C} - 700^{\circ}\text{C}$). The largest diameter decreased in the medium temperature range (i.e., 0.21 nm) whereas smaller diameter decreases were observed for the low (i.e., 0.07 nm) and high (0.04 nm) temperature ranges. Comparing the size changes with IR and ToF-SIMS data revealed that these temperature ranges corresponded to hydrogen desorption from silicon trihydride, dihydride, and monohydride, respectively.

The temperature dependence of the observed size reduction should be different for smaller particles because of differences in hydrogen surface coverage due to curvature. In the present study, we focus on nanoparticles in the 1 to 4 nm range to investigate the size dependence of hydrogen desorption with a tandem arrangement of

two nano-RDMAs appropriate for the lower size regime. We adopted the tandem configuration because it offers several advantages: (1) it reduces significantly the number of particles thereby preventing agglomeration; (2) it narrows the size distribution so that the observed size change can be attributed to a particular particle size; and (3) it prevents any unreacted precursor from contributing to particle growth in the furnace.

8.2. Experimental Description

The dependence of hydrogen desorption on particle size was studied using an atmospheric-pressure direct current microdischarge (MHCD),^[5] shown schematically in figure. 8.1. The discharge is maintained between a cathode (stainless steel capillary tube, I. D. $\approx 180 \mu\text{m}$) and an anode (stainless steel tube, O. D. $\approx 3 \text{ mm}$). The electrode assembly is enclosed in a glass tube (O. D. $\approx 12 \text{ mm}$) using standard Swagelok and UltraTorr fittings. An ultrahigh purity (UHP) argon/silane gas mixture flows through the capillary at a flow rate of 150 standard cubic centimeters per minute (sccm). In the afterglow portion of the microplasma between the two metal electrodes, a second UHP argon stream is added at a flow rate of 450 sccm to dilute the particles. This combined stream enters the first nano-Radial DMA (nano-RDMA),^[6] which is used either to characterize the particle size distribution or to select a fraction of particles for subsequent annealing. For particle sizing, the aerosol outlet flow of the nano-RDMA is directed to a home-built faraday cup electrometer sensitive to $\pm 1 \text{ fA}$. This permits determination of the particle size distribution originating in the microdischarge. The nano-RDMA is operated in stepping mode using a computer to control the voltage applied to the device. A two-second delay is used to stabilize the voltage before recording the average electrometer reading over one second. Once the size distribution from the microplasma is

determined, a constant voltage is applied to the first nano-RDMA to select a portion of the distribution around the maximum of the initial distribution. The peak position of the size distribution could be varied by changing the silane concentration introduced into the microplasma. The aerosol outlet of the nano-RDMA is connected to a thermal processing stage, consisting of an Inconel tube in a temperature-controlled furnace. After the thermal processing stage, the aerosol flow is actively cooled and directed to a second nano-RDMA for postannealing size analysis that is performed as described for the first nano-RDMA.

Measured particle size distributions were fit with a lognormal distribution using MatLab with concentration, geometric mean mobility diameter, and geometric standard deviation as the fitting parameters. While theoretical calculations have shown different structures for the hydrogenated and dehydrogenated clusters,^[7] the mobility diameters calculated here are based on the assumption of a spherical particle.

8.3. Results and Discussion

The MHCD produces a particle size distribution that is well-fit by a log normal distribution. A representative particle scan is shown in figure 8.2, which was recorded after the MHCD with the first nano-RDMA. Although not shown, the geometric mean mobility diameter could be shifted to larger sizes by increasing precursor concentration. Average particle size increases were accompanied by broadening of the distribution. For all precursor concentrations, the standard geometric deviations measured were less than reported literature values given the higher resolution of our nano-RDMA as compared to device intended for larger size regimes.^[5] The narrow size distribution of the as produced

nanoparticles for silane concentrations of 1 and 2 ppm required selecting the peak of the distribution to complete further experimentation.

A size distribution selected by fixing the voltage in the first nano-RDMA could be measured with the second nano-RDMA. A comparison between the two distributions is also made in figure 8.2. It is important to note that the distribution measured in the second nano-RDMA indicates a lower particle density, consistent with expected diffusion losses inside the processing stage. Increasing the furnace temperature decreases further the measured particle concentrations due to thermophoretic losses upon cooling the aerosol prior to the second nano-RDMA. Such losses are particularly severe for smaller particles given the lower initial particle densities.

For the largest particle size studied (i.e., 3.1 nm), the mean mobility data are shown in figure 8.3 as a function of the annealing temperature. The observed overall size reduction (i.e., 0.35 nm) occurred over three temperature ranges. The size reduction was 0.13 nm between 25°C and 300°C, followed by a 0.16 nm decrease in size between 300°C and 400°C, and 0.06 nm over a third temperature range of 400°C and 600°C. The proportion of the measured size reduction for each temperature range is different for particles with a smaller initial size (i.e., 2.7 nm), as depicted in figure 8.4. A greater portion of the overall size change occurs below 300°C (i.e., 0.23 nm), yet the overall size change is approximately the same (i.e., 0.35 nm). Beyond 400°C, the measured particle size changes only in a minor way (i.e., 0.02 nm). The size reduction for even smaller particles (i.e., 1.7 and 1.3 nm) is found to be quite different (figures 8.5A and 8.5B). The overall size reduction (i.e., 0.25 and 0.11 nm) was less than what was observed for the

larger particles and occurred almost completely in the low temperature range (i.e., 20°C and 300°C).

To examine the observed size change due to thermal annealing on a more consistent basis requires converting the data to a slightly different format. The smallest measured diameter is assumed to be the bare silicon nanoparticle and is subtracted from each measured size, as shown in figure 8.6. In this format, the change in size reduction behavior for different initial diameter particles as a function of temperature is demonstrated directly. In addition to the data collected in this experiment, the previously reported data are plotted for comparison.^[3]

The size change for the two largest diameters studied (i.e., 3.1 and 2.7 nm) proceeded similar to that reported for 6 nm particles.^[3] The overall size reduction of 0.35 nm measured in this report is very similar to the 0.32 nm found. For the largest diameter measured (i.e., 3.1 nm), the overall size change proceeded over three similar temperature ranges.

Yet, the proportion of the change that was observed over each temperature range was different. The size reduction of 0.1 nm between 25°C and 300°C is larger than that reported for the 6 nm particle.^[3] As before, a second region is observed between 300°C and 400°C over which a decrease in size of 0.15 nm is observed, a size change that is smaller than reported for the 6 nm particle. The final size change occurs at a lower temperature than previously reported but is similar in magnitude. Similar behavior is observed for particles with an initial diameter of 2.7 nm, but a larger portion of the overall size decrease occurred in the low temperature range.

Based on similarities in synthesis, these results are interpreted in terms of hydrogen evolution. For the low temperature range, the observed changes in diameter would be due to hydrogen desorption from silicon trihydride species. As the surface curvature increases (i.e., decreasing particle size), more of the surface would be covered in silicon tri-hydride groups. Therefore, smaller particles would have a greater portion of the observed size change in the low temperature range.

In the medium temperature range, the size change is attributed to silicon dihydride evolution. The opposite trend would be expected in this range as more silicon trihydride termination would result in less silicon dihydride coverage. Correspondingly, the portion of the diameter change increases with increasing size in this temperature range.

The difference in size reduction behavior becomes more drastic for the two smallest initial sizes measured. The overall diameter change is less than that observed for the larger particles, indicating most likely incomplete hydrogen surface coverage. The incomplete surface coverage could be due to the conditions present in the MHCD or due to an increase in the surface energy at such high surface curvatures.

To determine whether the measurements were of a kinetically limited process, the furnaces were operated at different temperatures (data not shown). It was found that the measured particle size was identical when only one furnace is set to 400°C (i.e., second furnace at 20°C) and when both furnaces were at 400°C. Similar measurements at other combinations of furnace temperatures confirmed that the size measurements were not of kinetically limited process.

8.4. Summary

The size evolution of silicon nanoparticles due to thermal annealing depends on the initial particle size. Three different temperature ranges were observed over which the particle size changed that were consistent with hydrogen desorption found in previous studies. Smaller particles evolved to the bare particle size at lower temperatures than larger particles. The data are consistent with smaller particles containing more silicon trihydride than larger particles. These measurements were not kinetically limited as increasing the residence time in the furnace did not affect the resulting particle size.

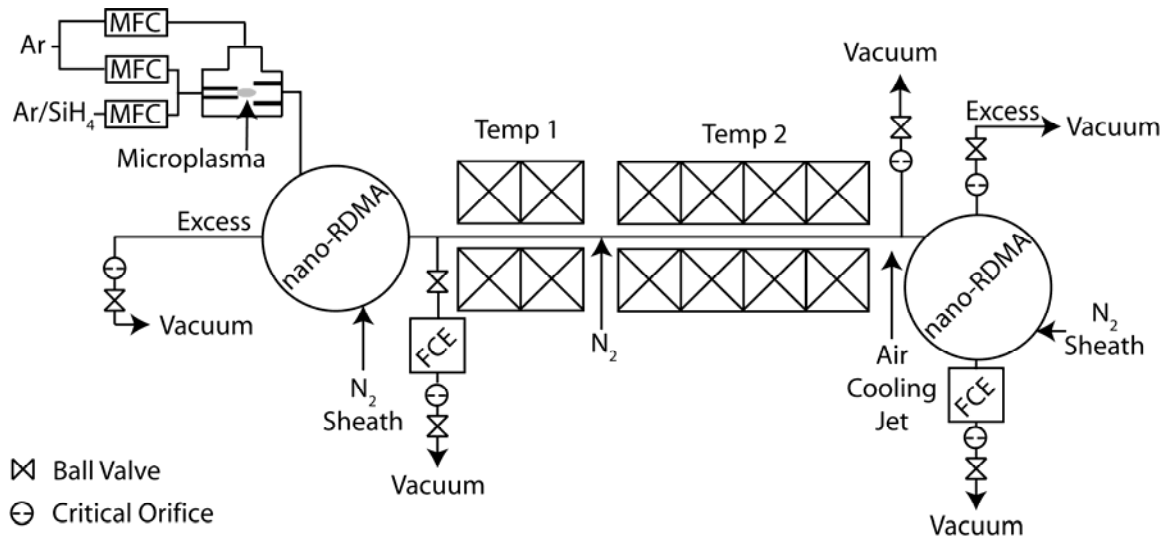


Figure 8.1. Schematic of Tandem DMA Sintering Arrangement.

Schematic of the microplasma and the tandem differential mobility analyzer arrangement used to sinter silicon nanoparticles. The furnace temperatures are independently controllable. The air cooling jet was used to maintain the temperature of the gas line at room temperature.

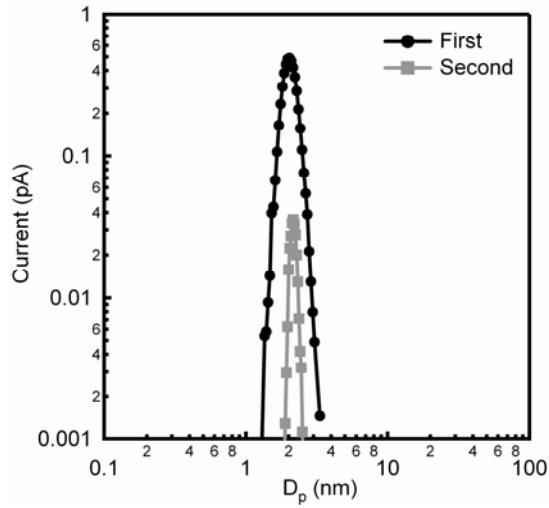


Figure 8.2. Size Distribution of First and Second nano-RDMA.

Comparison of the particle size distributions measured after the first and second nano-RDMA. The silane concentration introduced into the plasma was 2 ppm.

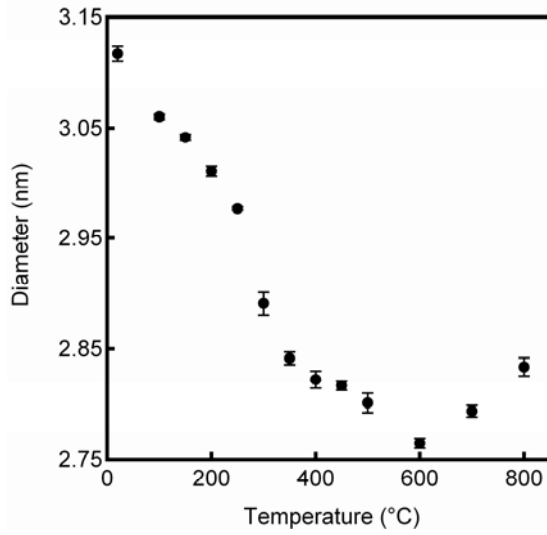


Figure 8.3. Size Variation of 3.1 nm Silicon Nanoparticles with Temperature.

Particle size measured at different temperatures for an initial silane concentration of 4 ppm in the microplasma.

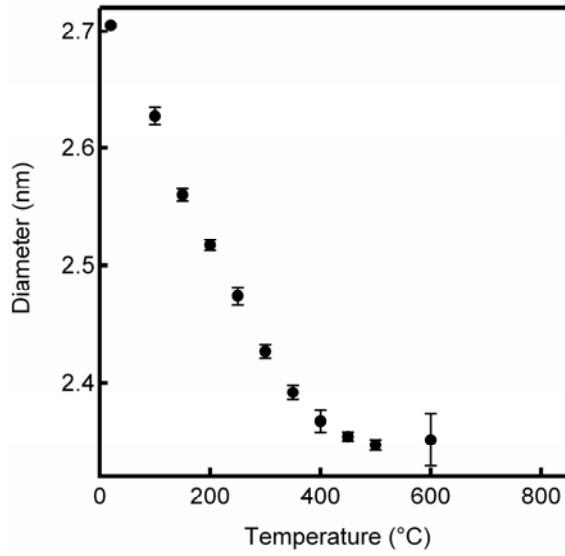


Figure 8.4. Size Variation of 2.7 nm Silicon Nanoparticles with Temperature.

Particle size measured at different temperatures for an initial silane concentration of 3 ppm in the microplasma.

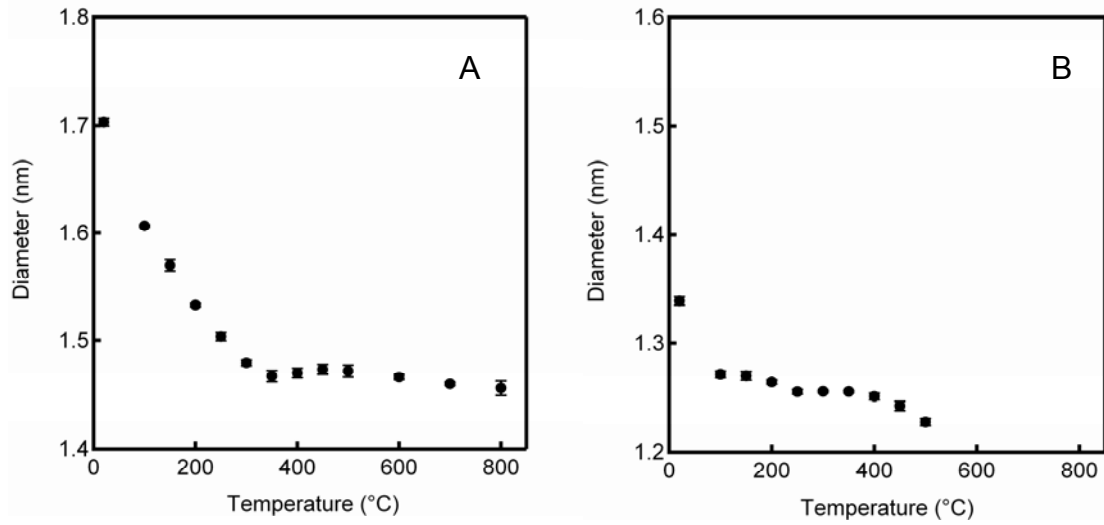


Figure 8.5. Size Variation of 1.7 and 1.3 nm Silicon Nanoparticles with Temperature.

Particle size measured at different temperatures for an initial silane concentration of 2 ppm (A) and 1 ppm (B) in the microplasma.

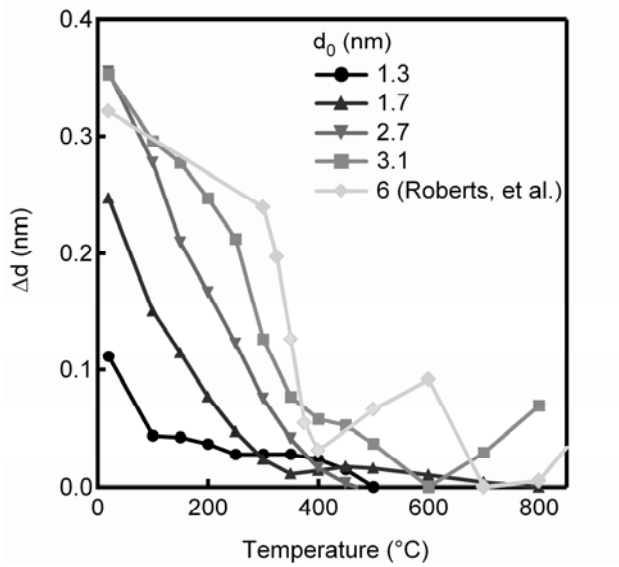


Figure 8.6. Comparison of Size Variation with Temperature.

Measured diameter difference with temperature between minimum particle size for silane precursor concentrations of 1, 2, 3, and 4 ppm. Data from a previous report is included for comparison.^[3]

References

1. G. Schmid, *Chemical Reviews*, **92**, 1709, 1992.
2. A. Cullis, and L. Canham, *Nature*, **353**, 335, 1991.
3. J. Holm, and J. Roberts, *Journal of the American Chemical Society*, **129**, 2496, 2007.
4. N. Salivati, and J. Ekerdt, *Surface Science*, **603**, 1121, 2009.
5. R. Sankaran, D. Holunga, R. Flagan, and K. Giapis, *Nano Letters*, **5**, 537, 2005.
6. N. Brunelli, R. Flagan, and K. Giapis, *Aerosol Science and Technology*, **43**, 53, 2009.
7. A. Barnard, and P. Zapol, *The Journal of Chemical Physics*, **121**, 4276, 2004.

Chapter 9: Particle Size and Surface Modification of Aerosol Silicon Nanoparticles

*The doubter is a true man of science; he doubts only himself and his interpretations,
but he believes in science. — Claude Bernard*

9.1. Introduction

Size, surface, and chemical composition are the most important factors in determining the optical, catalytic, and magnetic properties of a nanoparticle. Size has been shown to influence strongly the optical properties of semiconductor nanoparticles through the quantum confinement effect.[1-2] The energy spacing between the conduction and valence bands (i.e., the band gap) increases as particle size decreases beyond a certain limit, causing the optical emission to shift toward shorter wavelengths as compared to bulk emission.

The surface plays an increasingly important role as particles reach the one nanometer scale. For silicon nanoparticles, surface terminations of both oxygen and hydrogen can impact the optical emission.[3] Hydrogen termination can be achieved in gas[4] or liquid-phase[5] synthesis techniques. Exposing hydrogen-terminated Si

nanoparticles to air typically leads to the formation of a native oxide layer. The effect of oxidation on optical emission is complex. For large particles (i.e., >5 nm), surface oxidation creates a shell of silicon dioxide around a core of pure silicon. Reduction of the core size through oxidation may lead to manifestation of quantum confinement effects up to a point. When the core becomes smaller than 2 nm, the optical emission wavelength will not shift further to the blue as the surface oxidation introduces levels into the band gap.[3] Therefore, particle oxidation may be used to tune emission properties provided that the initial particle size is large enough.[6]

Surface termination is particularly important for Si nanoparticles produced by a recently developed atmospheric microplasma synthesis technique.[7] The microplasma was shown to produce concentrations greater than 10^8 nanoparticles per cubic centimeter with a mean size of 1.6 nm. This size is much smaller than that of nanoparticles produced by other aerosol methods.[8] While precursor concentration appeared to control particle diameter as determined from Radial Differential Mobility Analyzer (RDMA) measurements, the size distributions were broader than what would be expected for a monodisperse distribution of particles, indicating the measured size was that of agglomerates rather than the primary particles. It has been determined that the microplasma produces particles in the 1 to 5 nm size range (chapter 4). The small size makes the particle susceptible to oxidation that would degrade optical emission.

For increased versatility in applications and to overcome limitations of surface oxidation, it is desired to synthesize larger nanoparticles. The size control limitation of a single microplasma can be overcome using a secondary growth stage. For aerosol processes, both agglomeration and chemical vapor deposition (CVD) generate larger

particles. While larger, agglomerated particles tend to have a broad size distribution. Also, they do not exhibit a shift in PL emission since the particles remain discrete units, unless sufficient energy is provided for grain boundary diffusion and crystallization. In CVD, growth commences on the surface of previously generated particles. Thus, adjusting the reactant concentration and deposition time may permit control of the final particle size. An upper limit to the particle size may be reached when the CVD precursor causes new particles to nucleate. Unlike agglomerative growth, CVD does not broaden the size distribution, but rather tends to narrow the distribution since smaller particles tend to grow faster than large particles. Between these two particle growth techniques, CVD overgrowth seems to offer better final size control.

In this section, the results of several particle overgrowth schemes are presented. The first section describes an attempt to enlarge particles using two microplasmas operating in series, called the dual microplasma. Conceptually, the first discharge was used to nucleate particles while the second discharge served as the overgrowth stage. As an alternative, the second microdischarge was replaced by a sintering furnace. In both of these experiments, a single nano-RDMA (first version) was employed to characterize *in situ* and in real time the particle size evolution. Some additional work will be presented on using a tandem nano-RDMA arrangement.

9.2. Experimental Method

9.2.1. Dual Microplasma Setup

The experimental setup for the dual microplasma is shown in figure 9.1. The essential elements of the system were two microplasma reactors in series followed by a nano-RDMA. The operation of a single microplasma has been discussed previously.[7]

Briefly, a gas stream (150 sccm) consisting of argon and silane flows inside a small inner diameter microhollow cathode (MHC, I. D. $\approx 180 \mu\text{m}$) toward a larger tube serving as the anode (O. D. $\approx 3 \text{ mm}$). Between the two electrodes, a direct current microplasma is maintained enclosed within a glass tube through biasing the MHC negatively ($\sim 200 \text{ V}$) with respect to the anode. Once the aerosol stream leaves the MHC, it is diluted with an argon sheath stream ($\sim 450 \text{ sccm}$) in the afterglow region of the discharge.

The total flow from the first microplasma ($\sim 600 \text{ sccm}$ of plasma outflow and sheath dilution) plus any additional desired precursor were passed through the second MHC reactor. The cathode capillary of the second MHC was shortened to 10 mm and the inner diameter was expanded to 0.76 mm for a length of 9.5 mm. These modifications were required to maintain the pressure near atmospheric in the first microplasma, resulting in breakdown voltages ($\sim 800\text{--}1200 \text{ V}$) similar to those of a single microplasma. A separate argon sheath flow was introduced coaxially in the afterglow of the second microplasma.

The dual microplasma setup was linked to the nano-RDMA (version A) to observe the effect of different operating conditions on particle size. The flow rates were set as described above using a precursor concentration of 3 ppm in the first microplasma. With both microplasmas running, the particle size distribution was recorded; the nano-RDMA was operated in stepping mode using a computer to control the voltage applied with a sheath gas flow rate of 6 SLM. The sample outlet flow of the nano-RDMA was directed to a home-built Faraday cup electrometer sensitive to $\pm 1 \text{ fA}$. The total flow rate leaving the dual microplasma system was 1050 sccm, but the aerosol inlet flow to the

nano-RDMA was 600 sccm, requiring a portion of the particle stream to be diverted to a filter to maintain flow conditions in the nano-RDMA.

9.2.2. Overgrowth

The experimental set up used for overgrowth is shown schematically in figure 9.2. The essential elements were a microplasma source to generate nanoparticles, which were fed into a furnace for overgrowth and subsequent size analysis. The single microplasma source was assembled the same way as described above. The outlet was attached to a cross fitting where additional precursor (4% silane in argon diluted with an argon stream to vary concentration) could be added through two opposing connections of the fitting at a total flow rate of 50 sccm. Two mixing geometries were tested: diffusion and jet mixing. Jet mixing consisted of a cross fitting where the precursor stream was introduced through two opposing flow capillaries (I. D. $\approx 180 \mu\text{m}$) into the aerosol stream. The tip of the capillary was positioned to be in close proximity to the aerosol flow. Diffusion mixing did not utilize the flow constriction, introducing the additional precursor stream through standard sized tubing (O. D. $\approx 3 \text{ mm}$). The final connection of the mixing stage was attached to an Inconel tube (O. D. $\approx 6.3 \text{ mm}$, length 200 mm) that was placed inside a clam-shell-type furnace (Thermcraft RH 212, I. D. $\approx 32 \text{ mm}$, length 100 mm). The temperature of the furnace was set using a temperature controller (Omega CN9000; Type K thermocouple). After the furnace, the aerosol stream was split so that 600 sccm was sampled with the nano-RDMA and the remainder was passed through a filter before exhausting into the fume hood. The nano-RDMA was operated in voltage stepping mode using a 10 SLM flow of air as the sheath gas. The sample outlet flow of the nano-RDMA was directed to a home-built Faraday cup electrometer sensitive to $\pm 1 \text{ fA}$.

9.2.3. Size-Selected Overgrowth

Size-selected overgrowth was performed as shown schematically in figure 9.3. This is the same arrangement used to measure hydrogen desorption from the surface of a silicon nanoparticle (chapter 8). The essential elements are the microplasma source, two nano-RDMAs, and two thermal processing stages. The microplasma source was configured as described above. The aerosol stream emerging from the microplasma was directed to the aerosol inlet of the first nano-RDMA that was used either to analyze the particle size distribution or to select a narrow size distribution of the particles. For particle sizing, the sample outlet flow of the nano-RDMA was directed to a home-built Faraday cup electrometer sensitive to ± 1 fA. This permitted determination of the particle size distribution as produced in the microplasma. The device was operated in stepping mode using a computer to control the voltage applied to the nano-RDMA. A two-second delay was used to stabilize the voltage on the nano-RDMA and the signal of the electrometer before recording the average reading from the electrometer for one second. Once the size distribution from the microplasma was determined, a constant voltage was applied to the first nano-RDMA to select a fraction around the maximum of the initial distribution. The peak position of the size distribution could be varied by changing the silane concentration introduced into the microplasma. The aerosol outlet of the nano-RDMA was directed through two Inconel tubes in series (first tube, O. D. ≈ 6.3 mm, length 200 mm; second tube, O. D. ≈ 6.3 mm, length 400 mm). Each tube passes through a temperature-controlled (Omega CN9000, Type K thermocouple) furnace (first, Thermcraft RH 212, I. D. ≈ 32 mm, length 100 mm; second, Thermcraft Model 114-12-1ZV, I. D. ≈ 32 mm, length 300 mm). Two furnaces were used in this arrangement to

allow precise control of the surface. As seen previously, particle annealing in the first furnace resulted in a decrease in particle size. Selecting whether to heat the first furnace or not would permit study of particle overgrowth with different surface conditions.

Between the two furnaces, additional precursor (diluting from 4% silane in argon with an argon stream) can be added at up to a total flow rate of 300 sccm to the aerosol stream in a jet mixing configuration. The jet mixing stage consisted of a cross fitting where the precursor stream was introduced through two opposing flow constrictions into the aerosol stream. The different flow constrictions tested were capillaries (I. D. \approx 130 μ m and 180 μ m) and critical orifices (O'Keefe Controls Co.; size number 7, O. D. \approx 3 mm). The tip of the critical orifice and the capillary was positioned to be in close proximity to the aerosol flow.

After the second thermal processing stage, the aerosol flow is cooled and split between two streams. The first stream of 600 sccm is directed to a second nano-RDMA for post-processing size analysis that is performed as described for the first nano-RDMA while the second stream is exhausted through a filter.

9.3. Results and Discussion

9.3.1. Dual Microplasma

The measured particle size distribution for the dual microplasma arrangement is presented in figure 9.4. Interestingly, the measured distribution was bimodal and could be fit as the sum of two lognormal distributions with geometric mean diameter (D_{pg}) values of 1.6 nm ($\sigma_g = 1.18$) and 4.5 nm ($\sigma_g = 1.38$) with approximately five times more particles in the lognormal distribution with the larger D_{pg} . The origin of the bimodal distribution is intriguing. The smaller particle size (i.e., 1.6 nm) appeared to be due to the

second discharge. Operating the system with the first microplasma *OFF* and identical flow rates produced a size distribution with a D_{pg} of 1.8 nm ($\sigma_g = 1.22$). The larger particle size (i.e., 4.5 nm) appeared to be due to agglomerative growth of aerosol nanoparticles produced in the first discharge. The measured size could be compared to the distribution produced when operating only the second microplasma. This distribution had a D_{pg} of 3.5 nm ($\sigma_g = 1.25$). Given the residence time between the discharges, it is reasonable that particle agglomeration between the discharges could account for the difference in measured mobility diameter.

These measurements indicate that the dual microplasma configuration can increase the mobility diameter of the particles, generating particles that were larger than those produced in a single microplasma. Agglomeration appeared to be responsible for generating the larger particles as the geometric standard deviation for the dual microplasma configuration was larger than the value expected for CVD growth.

While agglomeration is not the preferred growth mechanism, it is possible that the microplasma can provide sufficient energy for crystallization, given that it has been shown theoretically^[9-10] that a temperature of 600 K is sufficient to coalesce two agglomerated particles containing 60 atoms in less than a nanosecond. To investigate whether the particles have crystallized or not would require photoluminescence (PL) characterization. Attempts to collect particles through bubbling into a liquid in order to obtain PL spectra were not successful. While it was also possible to measure PL spectra from particles on substrates, it would be necessary either to encapsulate the particles in an insulating matrix to prevent the effects of sample oxidation or to generate even larger particles so that the surface oxidation process would not quench the PL.

One way to achieve a further size increase via CVD was to add more reactant to the aerosol before the second microplasma. Size measurements shown in figure 9.5 indicated that additional reactant did not alter the size of the larger mobility diameter particles, but rather the additional silane increased the size and number of the smaller particles. Rather than achieving overgrowth, the microplasma reaction zone appeared to be sufficiently abrupt so as to nucleate new particles.

The final variable tested for the dual microplasma arrangement was gap length. Increasing the gap of the microplasma will increase the residence time in the afterglow portion of the discharge. The effect of gap length in the first microplasma is presented in figure 9.6. Increasing the gap produced fewer smaller particles and simultaneously increased the D_{pg} of the larger particles. The combined results indicated a more complete decomposition of the precursor in the first microplasma, which led to larger particles that agglomerate between the two microplasmas.

The gap of the second microplasma was also examined for an effect on the size distribution, as shown in figure 9.7. Increasing the gap of the second microplasma did not affect the size of the larger particles, but did increase the number of smaller diameter particles. This result provided further evidence that the smaller mobility diameter particles were generated in the second microdischarge.

It is important to note that although the smaller particles appear to be generated in the second discharge the composition of the particles is not known. The small mobility diameter particles could be due to unreacted silane or sputtered material from the cathode. While not conclusive, the key data were from the gap variation experiments. The gap of the second microplasma in the dual microplasma arrangement affected the

particle size and number concentration produced whereas the gap did not affect the particle size distributions produced from sputtering the cathode.

9.3.2. CVD Overgrowth

The results presented in figure 9.8 were from CVD overgrowth of silicon nanoparticles using diffusion mixing to combine the precursor and the aerosol with a furnace temperature of 400°C. The distribution produced from the microplasma was single modal with a D_{pg} of 2.92 nm ($\sigma_g = 1.16$). Adding silane to the aerosol stream increased the measured D_{pg} to 3.00 nm ($\sigma_g = 1.17$). The distribution remained single modal unlike in the dual microplasma arrangement, indicating that the furnace did not create the same degree of supersaturation that the microplasma does. The measured size increase and the approximately constant σ_g of the distribution indicated the growth mechanism could be CVD. Yet, the size increase was significantly less than expected based on concentration of the additional precursor added. Diffusion mixing was a limitation in the overgrowth process and resulted in a majority of the additional precursor not being used.

The mixing process can be improved through jet mixing, as demonstrated in figure 9.9. Introducing the same quantity of additional silane enlarged the distribution from a D_{pg} of 2.66 nm ($\sigma_g = 1.12$) to a D_{pg} of 4.27 nm ($\sigma_g = 1.18$). The size increased substantially with the better mixing, indicating a greater degree of utilization of the precursor. Unfortunately, the σ_g of the distribution also increased, indicating that the overall growth cannot be attributed solely to CVD. Interestingly, the particle number density also increased. The exact origin of the increase is not known, but it could be related to the transmission of the nano-RDMA (version A), a parameter that was not

characterized for this version and should increase with particle size. Alternatively, the larger particles could be more easily transmitted through the processing furnace, resulting in increased transmission.

The major drawback to these experiments is the unknown composition of the particle surface. The residence time inside the furnace and the high concentration of particles resulted in significant agglomeration, as shown in figure 9.10. Passing the aerosol through the furnace at room temperature resulted in a D_{pg} of 5.83 nm ($\sigma_g = 1.29$) whereas the size measured immediately after the microplasma was D_{pg} of 2.49 nm ($\sigma_g = 1.13$). Heating of the furnace to 400°C altered the residence time in the furnace, resulting in a D_{pg} of 2.51 nm ($\sigma_g = 1.15$). This broadening suggests that the particles have undergone a small degree of agglomeration. The net result was that the effects of particle overgrowth and agglomeration cannot be isolated in this arrangement.

9.3.3 Size-Selected Overgrowth

Selecting a narrow distribution of particles immediately after the microplasma source reduces the number concentration and the size distribution that is passed through the furnace, as shown in figure 9.12. The reduced concentration of particles can pass through the furnace without agglomeration. A size decrease was observed upon heating the furnaces, as seen previously (chapter 8). Mixing silane with the aerosol stream resulted in a small degree of particle overgrowth from an initial D_{pg} of 1.85 nm ($\sigma_g = 1.08$) to a D_{pg} of 2.26 nm ($\sigma_g = 1.12$) with the addition of silane to the size-selected aerosol stream. The overgrowth does not occur for the lowest concentration of silane added indicating that the process was diffusion-limited or required a threshold concentration to achieve overgrowth. The enlarged particle size distribution contained

fewer particles and was slightly broadened with respect to the initial distribution. The broadening is unexpected, and indicates that the particles are not uniformly reacting with the additional precursor possibly due to uneven mixing. The lower concentration is unexpected as well. The lower peak current can be caused by broadening, but could occur if the reaction causes the particles to lose their charge. These results represent a good starting point for additional experimentation.

9.4. Summary

CVD overgrowth could not be achieved using a second microplasma as an aerosol processing stage. The discharge produces an environment that causes nucleation of new particles homogeneously rather than overgrowing seed particles when additional silane was added to the aerosol stream before the second discharge. A furnace can be used to enlarge nanoparticles, but the high number concentration produced in the microplasma caused agglomeration and prevented characterization of the overgrowth as due to CVD. A greater degree of control over the overgrowth process can be achieved with the TDMA arrangement. The initial size-selection reduced the number concentration produced in the MHCD and prevented agglomeration.

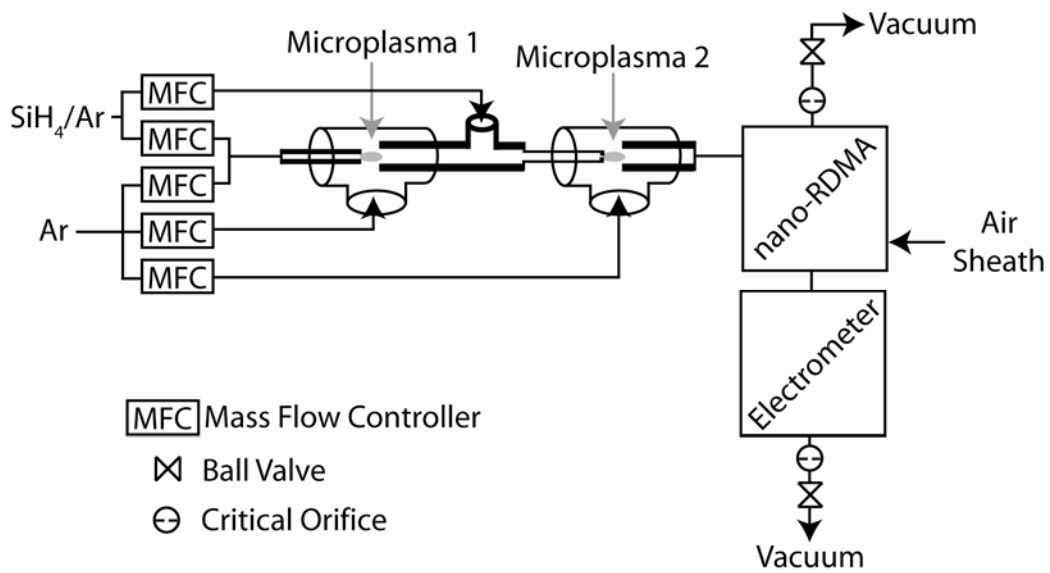


Figure 9.1. Schematic of Dual Microplasma.

Schematic of the dual microplasma arrangement.

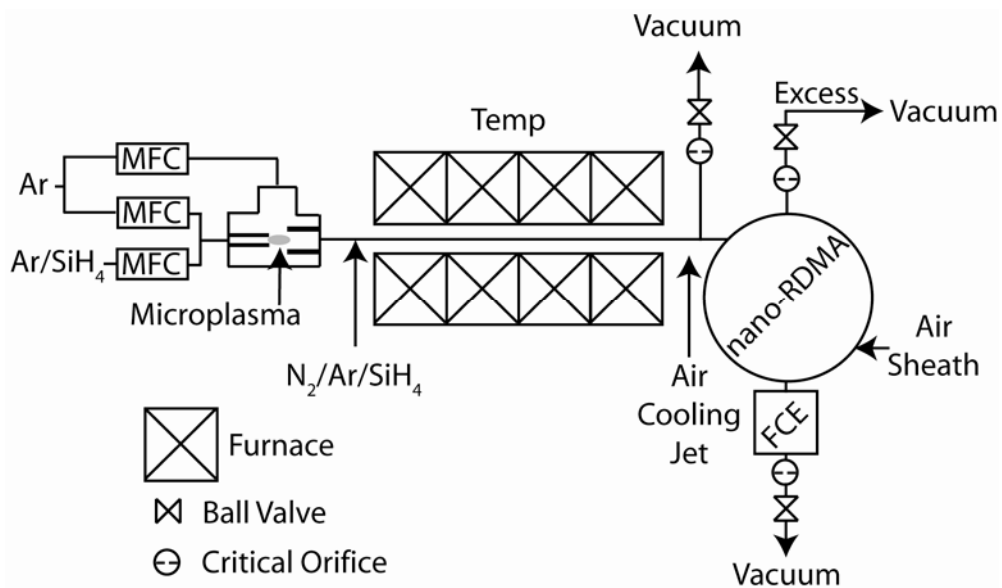


Figure 9.2. Schematic of the Overgrowth Arrangement.

Schematic of the overgrowth set up using only a single microplasma and introducing the entire particle size distribution produced in the microplasma into the furnace.

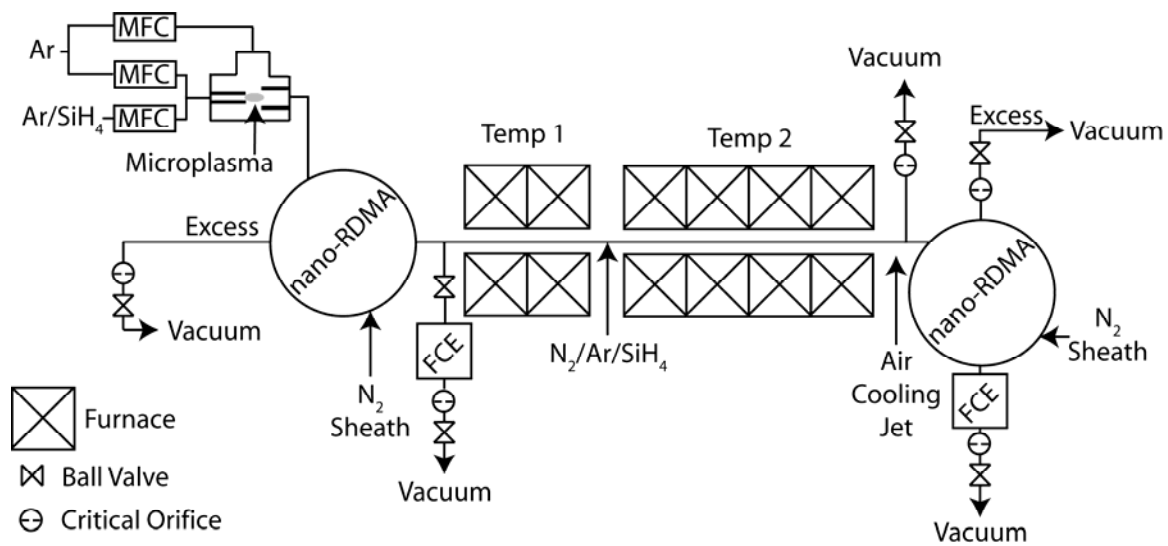


Figure 9.3. Schematic of the Tandem DMA Overgrowth Arrangement.

Schematic of the tandem DMA arrangement used for size-selected overgrowth.

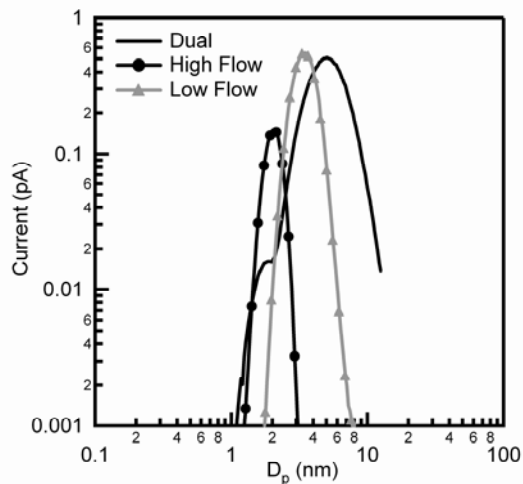


Figure 9.4. Size Distribution of the Dual Microplasma.

Comparison of the distribution produced using dual microplasmas (figure 9.1) and a single microplasma. The single microplasma (second discharge) was operated at low (flow rate of Ar_{plasma} of 150 sccm) and high (flow rate of Ar_{plasma} of 600 sccm) flow conditions. The silane concentration in first discharge was 3 ppm and no additional silane was added between the discharges. The electrode spacings were 1.5 and 1.0 mm for the first and second discharge, respectively.

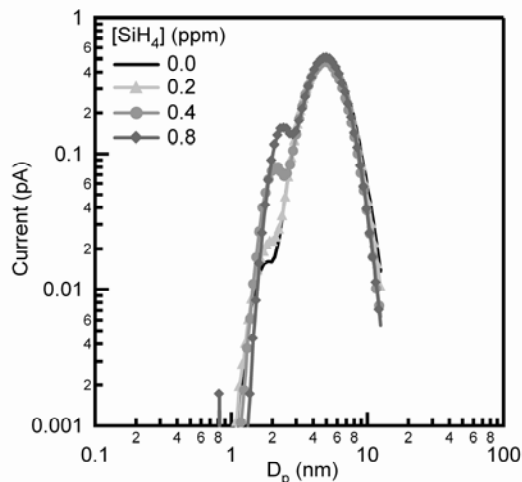


Figure 9.5. Size Distribution of Dual Microplasma with Additional Silane.

Comparison of the particle size distribution produced using the dual microplasma arrangement (figure 9.1) with additional silane added to the aerosol flow between the microplasmas. The silane concentration in the first discharge was 3 ppm and the indicated amount of silane was added between the two discharges. The electrode spacings were 1.5 and 1.0 mm for the first and second discharge, respectively.

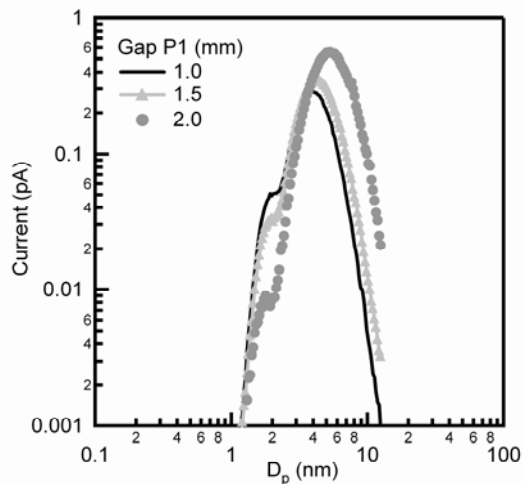


Figure 9.6. Size Distribution Produced with Dual Microplasma Varying First Gap.

Comparison of the particle size distribution produced using the dual microplasma arrangement (figure 9.1) by varying the gap of the first microplasma. The silane concentration in the first discharge was 3 ppm and no silane was added between the two discharges. The electrode spacing of the second discharge was 1.0 mm.

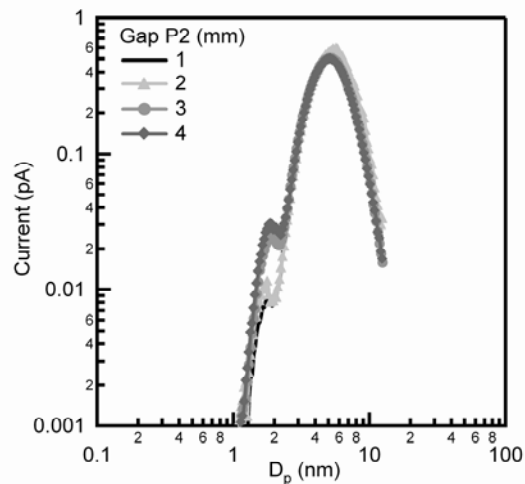


Figure 9.7. Size Distribution Produced with Dual Microplasma Varying Second Gap.

Comparison of the particle size distribution produced using the dual microplasma arrangement (figure 9.1) by varying the gap of the second microplasma. The silane concentration in the first discharge was 3 ppm and no silane was added between the two discharges. The electrode spacing of the first discharge was 2.0 mm.

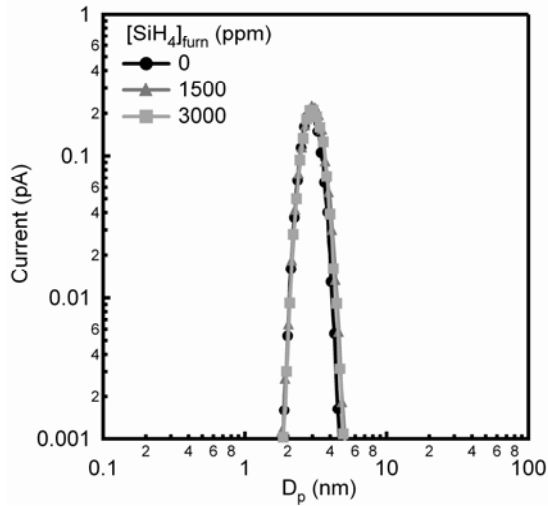


Figure 9.8. Size Distribution with Overgrowth with Diffusion Mixing.

Comparison of the particle size distribution measured with overgrowth in a furnace (figure 9.2; single nano-RDMA after the furnace) using diffusion to mix the precursor. The silane concentration in the discharge was 2 ppm and the concentration of silane added to the aerosol is indicated. The furnace temperature was 400°C.

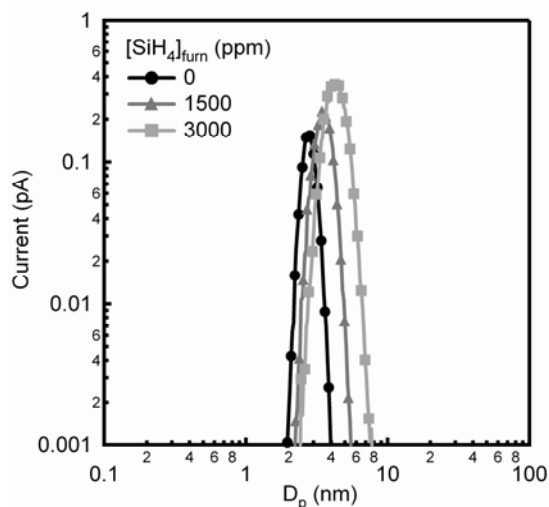


Figure 9.9. Size Distribution with Overgrowth with Jet Mixing.

Comparison of the particle size distribution with overgrowth in a furnace (figure 9.2; single nano-RDMA after the furnace) using jet mixing to combine the precursor with the aerosol stream. The silane concentration in the discharge was 2 ppm and the concentration of silane added to the aerosol is indicated. The furnace temperature was 400°C.

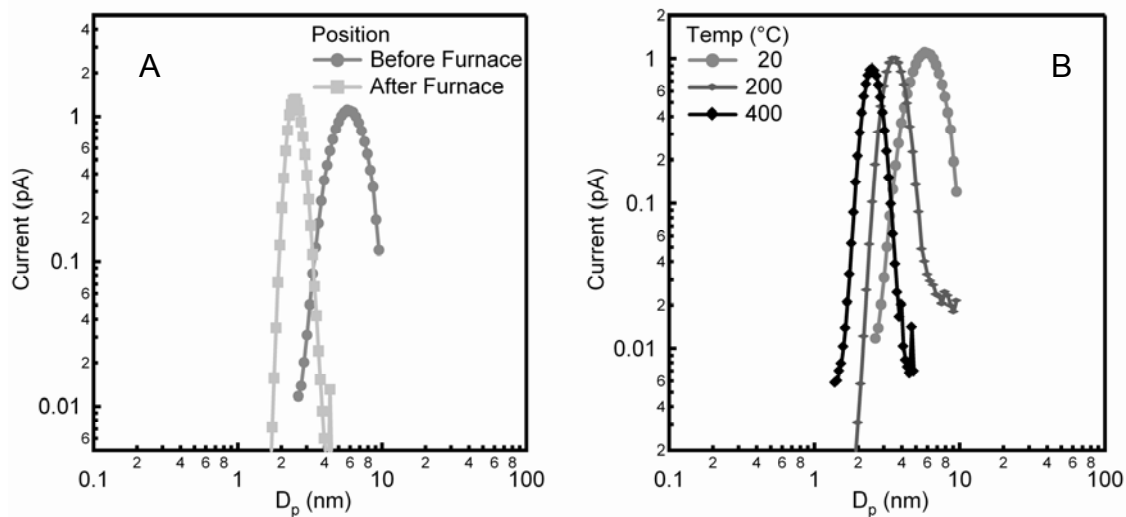


Figure 9.10. Size Distribution without Overgrowth from Single Microplasma.

(A) Comparison of the particle size distribution before and after the furnace (figure 9.2).

(B) Comparison of the particle size distribution after the furnace (figure 9.2) as the furnace temperature is increased. For all distributions, the silane concentration in the plasma was 2 ppm and no silane was added to the aerosol after the discharge.

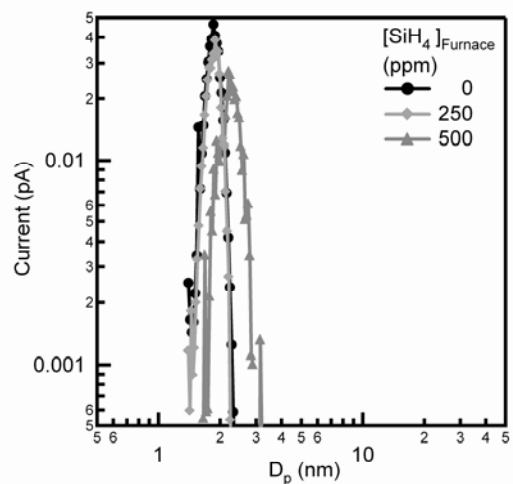


Figure 9.11. Size Distribution with Overgrowth in the Tandem DMA Arrangement.

Comparison of the particle size distribution measured with the second nano-RDMA of the TDMA arrangement (figure 9.3). The silane is added using jet mixing to the aerosol stream. The silane concentration in the discharge was 2 ppm. The furnace temperature was 400°C.

References

1. L. Canham, *Applied Physics Letters*, **57**, 1046, 1990.
2. M. Bawendi, W. Wilson, L. Rothberg, P. Carroll, T. Jedju, M. Steigerwald, and L. Brus, *Physical Review Letters*, **65**, 1623, 1990.
3. A. Puzder, A. Williamson, J. Grossman, and G. Galli, *Physical Review Letters*, **88**, 97401, 2002.
4. J. Holm, and J. Roberts, *Journal of the American Chemical Society*, **129**, 2496, 2007.
5. D. Neiner, H. Chiu, and S. Kauzlarich, *Journal of the American Chemical Society*, **128**, 11016, 2006.
6. A. Seraphin, S. Ngiam, and K. Kolenbrander, *Journal of Applied Physics*, **80**, 6429, 1996.
7. R. Sankaran, D. Holunga, R. Flagan, and K. Giapis, *Nano Lett*, **5**, 537, 2005.
8. D. Holunga, R. Flagan, and H. Atwater, *Industrial and Engineering Chemical Research*, **44**, 6332, 2005.
9. T. Hawa, and M. Zachariah, *Physical Review B*, **71**, 165434, 2005.
10. T. Hawa, and M. Zachariah, *Physical Review B*, **69**, 35417, 2004.

Chapter 10: Future Work

The most exciting phrase to hear in science, the one that heralds the most discoveries, is not "Eureka!" (I found it!) but "That's funny..." — Isaac Asimov

Research is the process of going up alleys to see if they are blind. — Marston Bates

10.0. Introduction

I am unsure of the exact details of the work that I will do next, but I have several ideas about what future directions students should take that are along the lines of what I have accomplished so far. If I did have more time, I would evaluate each of these ideas more thoroughly experimentally. It should also be noted that a few of these ideas are topics that I have discussed with others, but at this point have not been implemented and therefore are being recorded in this tome to ensure that they are known. A few of the ideas are currently being pursued.

10.1. Improved Electrospray Apparatus

The first suggestion is for the improvement of the electrospray source being used for the deposition of nano-structured fuel cell material. Currently, the gas flow for the electrospray is introduced into the chamber through two ports located on the external radius and exits through four ports located beneath the substrate holder (see appendix I for more details). The primary responsibility of the gas flow is solvent evaporation with the secondary purpose of ion scavenging. With the gas flow entering and exiting the

chamber away from the actual electrospray source, the gas flow may not be utilized as effectively as possible.

To improve the gas introduction method, a minor change in geometry can be made. The gas should be introduced closer to the electrospray source to generate as high of a superficial velocity near the electrospray tip as possible. The construction of a piece so that the gas flow is coaxial with the electrospray capillary should improve the evaporation. An unexpected benefit may be that the resultant electrospray of particles are smaller for a reason unrelated to evaporation. As the gas flow is heated before flowing into the chamber, introducing it closer to the electrospray capillary could convectively warm the capillary that would conductively warm the electrospray solution. Increasing the liquid temperature would decrease the surface tension of the solution. The decreased surface tension has been shown previously to decrease the particle size produced.

This idea is not without a few uncertainties that would need to be solved. Primarily, what should the characteristics of the gas flow be to ensure superior operation. The relevant parameters necessary to evaluate should be gas flow rate and gas temperature. These would have to be optimized to produce the desired structure.

10.2. Conductivity of Nanoscale Solid Acid Fuel Cell

The second suggested project is an alternative method to fabricate nano-structured materials for a more fundamental study of fuel cell conductivity. Currently, the electrospray is being utilized to decrease the feature size of the fuel cell material so that it matches the catalyst size. The electrospray has reduced the electrolyte size to 100 nm, but the effect of reducing the feature size is not clearly demonstrated with this study. The

particles agglomerate on the surface, resulting in structures with nanoscale features and larger overall structures.

An alternative approach to fabricate fuel cell material with uniform size is through using a template with uniform pore size. A material such as aluminum oxide can be fabricated so that it has uniform pores with defined sizes. While aluminum oxide is not appropriate due to reactivity with CDP, other materials can be used. The membrane would need to be electronically insulating and semirigid so that it could withstand some mechanical manipulation. The idea would be to fill the pores of the porous membrane with the fuel cell material. A few simple procedures could be successful such as spin coating a saturated solution into the porous material or solvent evaporation from a membrane using the incipient wetness method to fill the pores. Once filled, thin layers of catalytic material could be evaporated or thermally deposited onto the electrode surface. Varying the pore size and the catalytic material would permit study of a few important aspects of fuel cell conductivity. Both fuel cell performance measurements as well as symmetric cell impedance testing could be performed to ascertain these effects.

Beyond examining conductivity mechanism as a function of catalyst material and pore size, the porous membrane could be used as a template for electrode manufacture. Catalytic material could be deposited into the pores first, covering the walls with a thin film. The remaining pore could be filled with fuel cell material. After placing the filled porous material onto a pressed fuel cell pellet, the porous membrane could be removed, exposing the catalytic surface area. The resultant fuel cell electrode triple phase contact area could be maximized with judicious choice of pore size, pore length, and catalyst thickness.

10.3. Tandem Differential Mobility Analyzer Growth of Carbon Nanotubes

While these suggestions have been focused on ideas for fuel cell related applications, my work has been primarily focused on other areas. One of the interesting extensions of the current work would involve the combination of the tandem differential mobility analyzer (TDMA) and carbon nanotube growth experiments. Much work has been completed on *in situ* growth of carbon nanotubes from catalyst particles formed in the microplasma.[1-3] In these studies, the measurements had two limitations. First, they were performed using a nano-DMA. While designed to measure particle size in the 3 to 30 nanometer range,[4] this instrument does not have a resolution as high as would be desired in the 1–5 nm range to distinguish between agglomeration and monodisperse particle size distributions. The second issue is that the entire particle size distribution is subjected to the carbon nanotube growth conditions. With the high particle concentration and the length inside the growth furnace between microplasma reactor and measurement site, the particles should consist mostly of agglomerates rather than individual particles. The agglomerates would have a complicated surface structure that may allow multiple nanotube growth from a “single” particle.

Using the TDMA configuration with the nano-RDMA would most likely solve these issues.[5] The first nano-RDMA would reduce the number concentration so that additional residence time in the nanotube growth section would not lead to particle agglomeration. The first nano-RDMA would significantly narrow the particle size distribution as well, permitting data analysis to determine how a narrower distribution of catalyst size affects nanotube growth rate and type of nanotube produced. Without the

initial size selection, the average growth rate is attributed to the average size change of the original distribution.

The reduced particle number concentration will permit the carbon nanotube growth precursor to be varied over a few orders of magnitude. Higher precursor concentration should enable growth kinetics to be measured for nanotubes of substantial length without the complicating effects of agglomeration. The longer nanotubes will have a very large aspect ratio that will be interesting to study from a mobility perspective.[6] At some length, the mobility should deviate from the model prolate spheroid that has been previously used to describe the particle.

10.4. Sensitive Faraday Cup Electrometer

One of the biggest limitations in scientific measurements is low signal detection and amplification. For the field of aerosol science, low signals typically imply particle concentration below 10^4 per cubic centimeter. A faraday cup electrometer (FCE) is not appropriate below this concentration range as the noise level of these instruments is ± 0.1 fA due to thermal noise in the shunt resistor of the operational amplifier. To measure particle concentrations below this threshold requires usage of a condensation particle counter (CPC) or similar technology. This detector takes submicron particles and condenses vapor on the surface so that the particle size grows substantially, resulting in a particle larger than a micron. The enlarged particle scatters sufficient intensity so as to make low concentrations detectable. Below a critical size ($D_{p,50}$), the efficiency of particle enlargement is less than 50 percent. While improvements are being made on this style of detector, the presently reported size limit for detection is 1.3 nm.[7] The reason for this limit is that particles below this size cannot be activated for enlargement to

sufficient sizes in order that scattered light can be detected from the enlarged particle. Changing the working fluid improved the detection limit, but the progress has resulted in incremental improvements.

The size detection limit of the CPC is not present in the FCE. Rather than completely discounting the FCE, an alternative circuit design could be used and is being currently pursued. The shunt resistor is responsible for the Johnson noise that limits the lower detection current to greater than 0.1 fA.[8] A better strategy is to use a different feedback element: a capacitor with a capacitance on the order of 10 fF. The resulting circuit is an integrating operational amplifier that has a detection limit in the attoAmps range. The major obstacle is designing the circuit so that the integration can be reset, but this has been demonstrated by others.[9] The detection capabilities can be further improved through cooling this circuit with a thermoelectric element, to reduce thermal noise. Using this detector could eliminate the need for CPCs and the requisite working fluids that are a considerable hazard when operating in a reduced pressure environment aboard an airplane.

10.5. Nanoparticle Calibration Source for Differential Mobility Analyzers

The calibration of a Differential Mobility Analyzer (DMA) has been performed in two ways. The first method utilized an aerosol source to generate a broad range of diameters and two DMAs. The DMAs are assembled in the Tandem DMA arrangement with the first DMA providing a narrow distribution of the particles to the second DMA that was used to measure the distribution. It is often difficult to obtain broad distributions smaller than 5 nm.

The second method utilized an electrospray source to aerosolize molecular ions or polystyrene beads that are measured in a single DMA. The particles used as the size standard must have well-defined median size and a size distribution that is narrow or monodisperse so that the measured resolution will be that of the DMA. Molecular ions typically have a mobility diameter below 2 nm.[10] Larger molecules can have multiple charge states that must be identified using a mass spectroscopy, but do not usually conform to the shape of a spherical particle. Polystyrene spheres are typically used only for diameters larger than 10 nm, as smaller spheres are not well characterized for size, not as narrowly dispersed as would be desired, and not widely available.[11]

An interesting calibration standard in the 2–6 nm size range would be quantum dots. Quantum dots are semiconducting nanoparticles comprised of II-VI materials that have photoluminescent properties. The photoluminescence emission wavelength depends on particle size, and could be used to characterize the mean particle diameter and particle size distribution with an independent non-destructive method. These small particles are also spherical in nature and widely available in very narrow size distributions. These particles could be electrosprayed as was attempted with the molecular ions. It will be important to use a radioactive source to reduce the charge state to a single charge. A minor difficulty could be the surfactant layer that caps the particles, but this should lead to an easily correctable diameter offset.

10.6. Nanoparticle Synthesis Using a Water Plasma Electrospray

The primary application of electrospray has been to aerosolize molecules for the purposes of analysis with mass spectroscopy. The electrospray produces highly charged liquid droplets containing the analyte that evaporate until only the analyte remains in the

droplet. The parameters of the electrospray will determine the amount of analyte remaining after the droplet has evaporated. Evaporation of low volatility liquids can be expedited through heating the ambient gas.

Recently, the combination of an electrospray and a furnace has been reported to produce nanoparticles.[12] The analyte was replaced with a soluble but low volatility organometallic precursor. The droplets produced with the electrospray were passed through a furnace with the assistance of a gas flow.

The furnace is necessary to decompose the precursor to form nanoparticles, but the residence time in the furnace will limit the maximum concentration of monodisperse particles that can be produced. An alternative to the furnace may be capable of producing nanoparticles. It is well-known phenomena that at high applied voltage a plasma will form at the tip of the Taylor cone, as shown in figure 10.1. This phenomena has recently been examined in more detail.[13] The electric field at the tip of the Taylor cone is sufficient to cause breakdown, forming a plasma glow. This plasma could produce nanoparticle provided the glow has energetic electrons that can decompose the organometallic precursor or creates a reductive environment.

The choice of precursor will be critical to the success of this idea. An initial attempt used auric acid (i.e., HAuCl_4) in an attempt to form gold nanoparticles. Nanoparticles did form with the glow, but formed in its absence as well. It was determined that the stainless steel capillary reacted with the acid, reducing the gold salt to its zero-valent state and forming nanoparticles. Selecting an organometallic precursor that will not react with the capillary should permit investigation of whether the plasma can form nanoparticles.

The formation of nanoparticles can be monitored using standard aerosol techniques such as size analysis with a differential mobility analyzer with careful attention being paid to the charge state of the particle. The particles can then be collected electrophoretically for *ex situ* size and composition analysis. Nanoparticles of multiple compositions could be formed through changing the precursor in the solution. In general, the plasma glow of the electrospray could be an ideal source to produce nanoparticles.

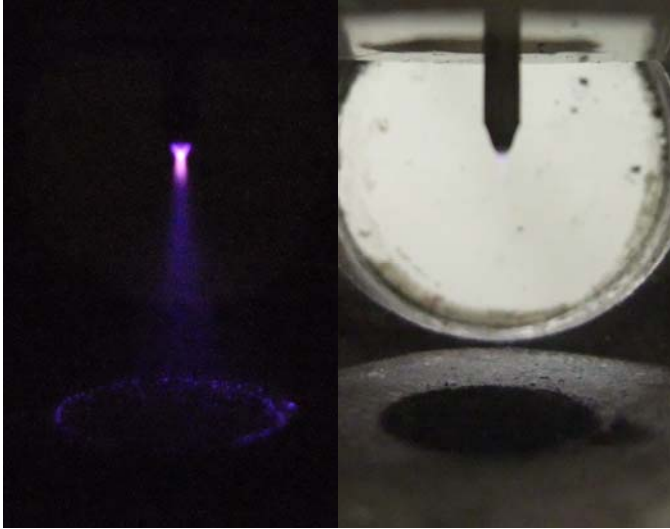


Figure 10.1. Electro spray Plasma

Image of the plasma that develops at the tip of the Taylor cone of an electro spray taken in the dark to highlight the plasma glow that develops. The second image portrays the electro spray apparatus in the light. A faint glow still appears at the tip of the capillary.

References

1. W. Chiang, and R. Sankaran, *Applied Physics Letters*, **91**, 121503, 2007.
2. W. Chiang, and R. Sankaran, *The Journal of Physical Chemistry C*, **112**, 17920, 2008.
3. W. Chiang, and R. Sankaran, *Nature Materials*, **8**, 882, 2009.
4. D. Chen, D. Pui, D. Hummes, H. Fissan, F. Quant, and G. Sem, *Journal of Aerosol Science*, **29**, 497, 1998.
5. D. Rader, and P. McMurry, *Journal of Aerosol Science*, **17**, 771, 1986.
6. D. Song, I. Lenggoro, Y. Hayashi, K. Okuyama, and S. Kim, *Langmuir: The ACS Journal of Surfaces and Colloids*, **21**, 10375, 2005.
7. K. Iida, M. Stolzenburg, and P. McMurry, *Aerosol Science and Technology*, **43**, 81, 2009.
8. P. Horowitz, and W. Hill, *The Art of Electronics*. (Cambridge University Press, Cambridge, 1989).
9. A. Knight, R. Sperline, G. Hieftje, E. Young, C. Barinaga, D. Koppelaar, and M. Denton, *International Journal of Mass Spectrometry*, **215**, 131, 2002.
10. S. Ude, and J. Fernandez de la Mora, *Journal of Aerosol Science*, **36**, 1224, 2005.
11. S. Ude, J. Fernandez de la Mora, J. Alexander, and D. Saucy, *Journal of Colloid and Interface Science*, **293**, 384, 2006.
12. I. Lenggoro, K. Okuyama, J. Fernandez de la Mora, and N. Tohge, *Journal of Aerosol Science*, **31**, 121, 2000.
13. J. Lopez-Herrera, A. Barrero, A. Boucard, I. Loscertales, and M. Marquez, *Journal of the American Society for Mass Spectrometry*, **15**, 253, 2004.

Appendix I: Electrospray Sources

A1.1 Introduction

Electrospray has been used to aerosolize low volatility materials such as proteins, molecular ions, and inorganic salts. Depending on the nature of the application and the type of the material to be volatilized, the characteristics of the electrospray will be different. Regardless of the actual configuration, the essential element of the electrospray is the formation of a stable Taylor cone. The Taylor cone forms when the surface tension of the liquid, the force due to the applied electric field, and the pressure balance, causing the liquid to form a conical protrusion with a half angle of 45.3° that is typically formed at the end of a capillary. At the tip of the cone, the liquid emits a fine dispersion of charged droplets containing dissolved species. The relatively high volatility liquid will evaporate, resulting in progressively smaller droplets. If the droplet becomes highly charged to the point of the Rayleigh limit, the droplet will emit daughter ions that are significantly smaller to reduce the amount of charge on the droplet. At the daughter ion formation and liquid evaporation process, the insoluble material is the only element remaining. To control the amount of material in the final product, many parameters can be varied including the solvent, the solute concentration, and the evaporation rate (through temperature and gas dilution), among other variables. As the two applications of electrospray described in this work are very different in nature, two very different electrospray units were constructed and are described in the following sections.

A1.2 Electrospray Apparatus: Detailed Assembly

While electrospray sources come in a variety of forms, the electrospray units built for the research described in this report have three basic components: (1) the electrospray unit, (2) the liquid delivery system, and (3) the gas delivery system. While these basic elements are similar for both of the electrospray units constructed, the actual details of the design are different. For instance, the liquid delivery system is identical for the two electrospray sources. A key difference is that the electrospray unit used for thin film deposition requires a holder for the substrate to collect electrosprayed material. To completely describe the two electrospray units, the common liquid delivery system will be described first and the details of the individual electrospray units will follow.

A1.2.1 The Liquid Delivery System

The liquid delivery system selected for both electrospray apparatuses utilizes the gas pressure above the liquid to force the liquid through the electrospray capillary. A regulator is used to reduce the pressure of the compressed air available in the lab to lower pressures. The output of the regulator is attached to a Swagelok “cross” fitting. The first connection of the “cross” has a series of one-way valves (not shown) that will maintain 3 psi of pressure on the regulated line before triggering to release excessive pressure. The second connection is attached to a pressure gauge (range; 0–20 psi). The final connection is attached to a three-way valve (not the common connection of the valve). The common connection of the three way valve is connected with a plastic tube that is inserted through a rubber stopper to the headspace of the liquid reservoir (100 mL round-bottom flask). The third connection of the three way valve is open to ambient pressure. Depending on the direction of the valve, the headspace above the liquid is

either pressurized (open to regulator) or not (open to ambient). The rubber stopper has a second piece of plastic tubing protruding through it that is connected to the electrospray capillary. The end of this plastic tube inside the reservoir is immersed in the liquid so that once the reservoir is pressurized the liquid will flow through the tubing. With this configuration, the liquid flow rate can be controlled to a limited extent through adjusting the pressure on the output of the regulator.

To stop the flow of liquid to the electrospray capillary, the three way valve is first opened to the ambient. This will only stop the flow of liquid and the liquid in the immersed plastic tubing will remain stagnant. To empty this liquid back into the reservoir, the drying gas must be flowing through the electrospray chamber and a valve downstream of the electrospray chamber must be closed. Closing this valve will pressure the electrospray system until the gas flows through the capillary, pushing the liquid in the plastic tubing back into the reservoir.

A1.2.2 Electrospray for Volatilization of Molecular Ions

The electrospray unit used to volatilize molecular ions is schematically pictured in figure A1.1. For this system, the electrospray is generated at the tip of stainless steel (SS) capillary (O. D. \approx 1 mm, I. D. \approx 130 μ m, length 50 mm). The tip of the capillary is carefully machined to a fine point (\sim 200–300 μ m) and subsequently sanded (grit 2000) to produce a smooth finish where the tip is perfectly flat.

The capillary is positioned inside an NPT cross (1/4" Stainless Steel) using a custom-machined plastic (Delrin) part with the tip pointing vertically downward. The plastic part is threaded on one end so that it can seal with the NPT fitting. The other end of the plastic part seals against the capillary using an O-ring and a plastic cap to compress

the O-ring. This plastic part serves to electrically isolate the capillary from the remaining parts of the electrospray assembly and to hold the capillary so that the sharpened tip is in the center of the cross fitting.

The capillary is biased using a positive high voltage power supply (Acopian 10 kV) while the NPT cross is grounded. The NPT connection opposite the capillary is used for the aerosol outlet. When an NPT to Swagelok fitting was placed on this connection, the gap between the capillary and the grounding point was non-uniform. A piece (I. D. \approx 1 mm) was machined to fit inside the cross. This piece created a more uniform electric field and decreased the gap between the capillary and the ground, increasing the electric field.

The two remaining connections of the cross adjacent to the capillary are used to introduce the aerosol carrier gas into the electrospray unit and to visualize the Taylor cone of the electrospray. Attached to these connections on both sides is a “tee” fitting where one connection is an NPT type and the other two are Swagelok. The NPT connections are attached to the female NPT connection of the cross in such a manner that an optical path is maintained through the center of the NPT cross. The Swagelok connection not along the optical path is connected to a nitrogen stream that is controlled using a mass flow controller.

To seal the electrospray unit while maintaining the optical path required two identical window assemblies. A small window (5 mm O. D.) is epoxied in place on the inside of a Swagelok nut. Once the epoxy dries, Teflon ferrules are inserted into the nut with the appropriate orientation. A short length (\sim 4 mm; O. D. 6 mm) of stainless steel

tubing whose bore has been enlarged is inserted into the ferrules. Without this short section of tubing, the ferrules will not seal and will impede the optical path.

For this assembly using 1-propanol as the electro spray solvent, a positive bias of approximately 3.5 kV is required to maintain the Taylor cone. The Taylor cone could be monitored using a web camera positioned along the optical path. A representative image of the stable Taylor cone is provided in figure A1.2.

A1.2.3 Electro spray for Nano-structured Electrodes

The electro spray unit used to form nano-structured electrodes is schematically pictured in figure A1.3. For this system, the stainless steel capillary (O. D. \approx 1 mm, I. D. \approx 130 μ m, length 50 mm) used to generate the electro spray was carefully machined to a fine point (\sim 200–300 μ m) and subsequently sanded (grit 2000) to produce a smooth finish where the tip is perfectly flat. To generate the electro spray, the capillary is biased using a positive high voltage power supply (Acopian 10 kV) while the aluminum body and the sample holding pedestal are grounded.

The body of the electro spray unit is aluminum (O. D \approx 50 mm, I. D. \approx 40 mm, length \approx 80 mm). On one end, a plastic (Delrin) part is used to position the electro spray capillary so that the tip points vertically upward. The plastic part holds the capillary in place using an O-ring and a plastic cap to compress the O-ring against the capillary. This plastic part serves to electrically isolate the capillary from the remaining parts. An upward geometry was preferable as this prevented any liquid dripping from the capillary onto the substrate holder. Dripping was a major problem as the liquid would re-dissolve the material that had been electro sprayed, resulting in a coarser structure.

On the other end of the aluminum body is a second plastic piece that holds an aluminum pedestal that is used to hold a substrate for material collection. As the sample rests upside down during material collection, a press-fit ring is used to hold the sample on the pedestal. The portion of the pedestal inside the chamber is heated via conduction from the portion outside of the chamber.

In the side of the aluminum body, four ports have been made. Connected to two of the ports are the gas inlet streams on opposing sides of the chamber. The drying gas exits through four holes drilled radially into the side of the pedestal behind the sample. The remaining two ports have windows epoxied into place. One window admits light into the chamber so that observation of the Taylor cones can be made through the other window.

To facilitate drying of the electrosprayed material, the inlet gas lines (T_1), the chamber (T_2), and the pedestal for deposition (T_3) can be heated. Each of these sections is independently heated with heat ropes. The temperature of each section is maintained constant with a temperature controller.

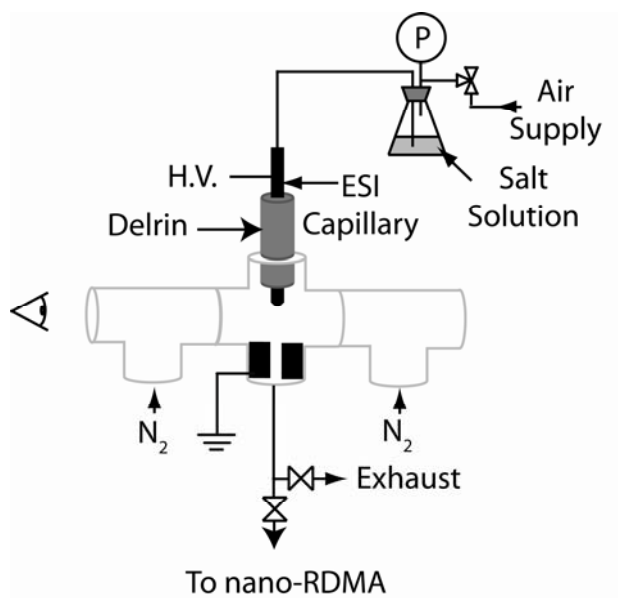


Figure A1.1. Schematic of the Electrospray Source.

Schematic of the electrospray source used to volatilize molecular ions.

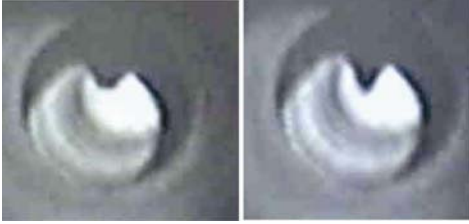


Figure A1.2. Electro spray.

Image captured of the electro spray unit before introducing fluid and after introducing fluid when operating with a Taylor cone.

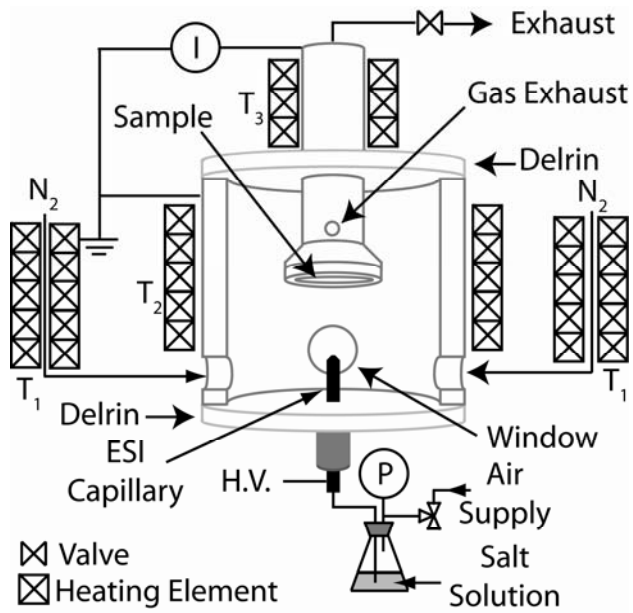


Figure A1.3. Schematic of Electro spray.

Schematic illustration of the electro spray source used to form nano-structured thin films.

Appendix II: Composite Nano-structured Solid Acid Fuel Cell Electrodes via Electrospray Deposition¹

A2.1. Introduction

Due to their high efficiency, the possibility of cheap interconnects, and fuel flexibility, intermediate temperature fuel cells are attractive alternatives to combustion engines and could contribute significantly toward alleviating the energy crisis. Not only do solid acid fuel cell operating temperatures fall into the intermediate range, the true solid state proton conducting electrolyte provides many practical simplifications compared to existing technologies such as phosphoric acid or alkaline fuel cells.¹

It is well known that most low and intermediate temperature fuel cells are performance limited by the rate of oxygen reduction at the cathode. In order to catalyze the reactions, precious metals, such as platinum are most often used. Current platinum utilization at 10 mg cm^{-2} is not cost-effective when considering large-scale commercial applications.² Therefore, significant research efforts are needed for the discovery of non-precious metal catalysts and/or for a more efficient utilization of costly platinum. In the case of platinum, the oxygen reduction is a multistep reaction, occurring at the boundary between the electrolyte, catalyst and the gas phase—the triple phase boundary, where the simultaneous and coordinated transport of electrons, ions, and gas molecules can occur.² An increase of triple phase boundary per unit area of electrode could increase the number density of catalytically active sites and therefore fuel cell performance. The aim of the

¹ This work was completed in collaboration with Áron Varga

presented work is to fabricate an interconnected, porous, three dimensional composite nanostructure of the electrolyte and catalyst, potentially reducing the amount of platinum necessary for a given performance.

In order to increase the number density of the triple phase boundary at the electrode, it is thought to be necessary to match the feature size of the electrolyte to that of the catalyst,² which is already commercially available in the form of 10 nm diameter nanoparticles see figure A2.1. Here, a given Pt nanoparticle can be in contact with multiple electrolyte particles, hence significantly increasing the triple phase boundary sites per Pt nanoparticle, which in turn increases their utilization or reduces the amount by weight necessary for a given performance level.

In order to reduce the size of CsH_2PO_4 to match the Pt nanoparticle size, we have utilized electrospray. Electrospray is a widely used tool for aerosolizing a liquid.³ It relies on electrostatic forces to expel micrometer sized droplets from a charged liquid. Here, a solution is pumped through a capillary, forming a cone at the capillary tip, called the Taylor cone.⁴ The high electric field at the tip of the cone induces the emission of a fine spray of charged droplets. It is thought that as the droplets are accelerated toward the grounded substrate, evaporation of the solvent leads to charge concentration, inducing breakup of the droplet and ultimately forming submicron to nanoscale particles that can be deposited on the substrate. As a fuel cell fabrication tool, electrospray has been employed to produce dense, thin-film electrolytes for SOFCs^{5,6} and PEMFC electrodes.⁷ A wide range of chemical and physical parameters can be varied to tune the characteristics of the resultant structure that can range from dense thin films to porous electrodes. These parameters include solvent concentration, solution composition,

(affecting solution conductivity, surface tension, viscosity), spraying temperature, drying gas flow rate, and spray geometry (e.g., tip-to-substrate path length, spraying direction).

A2.2. Experimental Method

A2.2.1. Deposition

The electro spray apparatus used for these experiments is shown in figure A.2.2. It consists of a stainless steel capillary (I. D. 127 μm , O. D. 1.6 mm, L 50 mm) that has been machined to a point with a half angle less than the Taylor cone half angle. The sharpened end of the capillary opposes an aluminum pedestal (O. D. 25.4 mm) where the substrate is mounted. The pedestal temperature was controlled with a feedback controlled system using a heat rope. Between the capillary and the pedestal, a positive bias in the 4 to 6 kV range is applied so as to maintain a stable Taylor cone. The substrate-capillary distance can be varied between 25 to 40 mm by sliding the capillary in or out the chamber. These parts are enclosed in an aluminum housing with two plastic end caps made of Delrin (polyoxymethylene) to electrically isolate the capillary and the pedestal (the end caps limit the upper operating temperature of the system to the plastic melting point of 175°C). The housing is independently heated in a manner similar to the pedestal. Visualization of the Taylor cone was achieved with two glass windows (diameter \sim 12 mm) epoxied into the side of the housing at opposite sides. The light from one window provided sufficient contrast to observe the Taylor cone directly through the second window. Two additional ports were made in the housing so that nitrogen gas could be introduced into the chamber at a fixed flow rate controlled with a mass flow controller. Nitrogen was chosen as the drying gas as it is less susceptible to electrical breakdown than a noble gas. A flow rate of 1000 sccm was chosen to aid evaporation.

The nitrogen is exhausted through a hole in the pedestal behind where the substrate rests. Before entering the housing, the nitrogen is independently heated with a third temperature controller to the same temperature as the housing. The pedestal was used to avoid dripping of excess solution onto the substrate due to common instabilities during the spraying process. It was found, that any dripping resulted in re-dissolution of the electrolyte and coarsening of the nanostructure (not presented in this paper). Holding the substrate on the pedestal was accomplished with a press-fit aluminum ring. Here, carbon paper (Toray TGP-H-120) was utilized as the substrate. It is cheap, inert with respect to CsH_2PO_4 , and can serve as a current collector due to its high electrical conductivity. The solution was pumped via a sealed and pressurized container in order to avoid ratcheting effects present in syringe pumps. The air pressure was controlled between 0.1 and 0.2 psig obtain a flow rate of 5 and 15 $\mu\text{L min}^{-1}$, measured by weighing the sealed container before and after the spraying process. The current carried by the flux of charged particles to the substrate was measured by a picoammeter (Keithley 480 Digital 3.5 Digit Bench Picoammeter) connected in series between the ground wire and the pedestal. The critical parameters are summarized in table A2.1.

A2.2.2. Solution Properties

A series of solutions was prepared with a composition ranging from 10 to 50 mol% methanol in water. CsH_2PO_4 is soluble in water and also readily dissolves in all water-methanol solutions investigated at a concentration of 10 g L^{-1} . In separate experiments, platinum black (Alfa Aesar, Ward Hill, MA; nominal $\sim 30 \text{ m}^2 \text{ g}^{-1}$) and platinum, nominally 40% on carbon black (Alfa Aesar Ward Hill, MA), and multiwalled carbon nanotubes (MWCNTs) were added each to the water methanol mixture.

Concentrations of 5 g L⁻¹ of platinum black and platinum on carbon nanoparticles, and of <1 mg L⁻¹ of MWCNTs were used. A stable colloidal suspension was obtained via the addition of the commonly used surfactant, polyvinylpyrrolidone (PVP; Alfa Aesar, MW 8000),¹¹ at a concentration of 20 g L⁻¹.

A2.2.3. Oxygen Plasma Treatment

The surfactant polyvinylpyrrolidone (PVP) was subsequently removed from the surface of the structure with an oxygen plasma treatment to ensure active surface sites were not blocked. The radio frequency (13.56 MHz) plasma was generated by inductively ionizing an argon-oxygen gas mixture (Ar flow: 7.5 sccm, O₂ flow: 2.5 sccm) with a copper wire coil wound around a quartz chamber. The electrospayed carbon paper substrate was placed on a pedestal in the afterglow portion of the plasma and treated for 4 minutes using a plasma power of 150 W with a chamber pressure of 136 mTorr. PVP removal was confirmed using infrared spectroscopy (Nicolet 860 Magna series FTIR).

A2.2.4. AC Impedance Measurements

Symmetric electrochemical cells have been fabricated using dense CsH₂PO₄ electrolyte and two identical, electrospayed carbon paper pellets as the electrode. The electrolyte was obtained by cold-pressing CsH₂PO₄ powder for 20 minutes under a uniaxial pressure of 34 MPa.¹ The electrospayed electrodes were lightly pressed onto the electrolyte by a compression holder, tightening screws via a torque wrench to avoid excessive damage of the microstructure and obtain good ionic conductivity across the interface. Two stainless steel porous plates were placed on either side of the symmetric

cell in order to give uniform gas diffusion to the surface of the electrode as depicted in figure A2.3. Impedance data was collected in a symmetric humidified hydrogen environment at 240°C with a Solartron impedance analyzer operating at a voltage amplitude of 10 mV over frequencies ranging from 10 mHz to 1 MHz. Hydrogen was supplied at a rate of 25 sccm and humidified flowing through a water bubbler held at 80°C.

A2.3. Results and Discussion

Initially, a three dimensional, interconnected, porous structure of CsH_2PO_4 was obtained (figure A2.4.), by electro spraying an aqueous solution of CsH_2PO_4 . The critical parameters are summarized in table A2.2. The average feature size was directly measured on the SEM micrograph to be circa 300 nm. The X-ray diffraction pattern of the nanostructure (figure A2.5.) confirmed no change in the CsH_2PO_4 structure after the spraying process. A typical deposition rate of 5 mg hr^{-1} and deposition efficiency of 50%-70% was measured by weighing the sample and solution before and after deposition with a precision balance. The sample surface coverage was complete but non-uniform. The thickness of the nanostructure ranged from 20 μm at the center of the sample to 10 μm at the edge. It is thought that the non-uniformity of the deposition results from statistical variations of the charge carried by each droplet and the radial decrease of the electric field strength. The dominant force acting on the charged droplets and particles is thought to be electrostatic in nature. Their flight path follows electric field lines and the number density of deposited particles correlates with the strength of the electric field. Experiments that varied the substrate temperature over a range from 65°C to 140°C with all parameters constant, resulted in no dramatic change of the morphology of the

nanostructure. Hence, it is thought that the fractal nature of the nanostructure is created by complete evaporation of the solvent before CsH_2PO_4 particles are deposited, with deposition preferentially onto protrusions created by already deposited structures, rather than vigorous evaporation of the solvent when the droplets arrive on the substrate, creating voids.

Certain combinations of electrospray and solution parameters, see table A2.2, leads to non-complete evaporation of the solvent, and the deposition of CsH_2PO_4 splats onto the substrate. A dense thin film of the electrolyte can form as shown in figure A2.6.

With exposure to atmosphere, CsH_2PO_4 readily absorbs water from air as it is highly hydrophilic. Its mechanical properties deteriorate,⁸ leading to agglomeration of the nanostructure and the complete loss of its fractal nature. figure A2.7A,B show the start of agglomeration after two days in ambient conditions and the subsequent full collapse of the nanostructure with complete loss of porosity and high surface area after seven days in ambient conditions.

It has been found that cospraying with certain additives stabilizes the nanostructure. Electrospraying the colloidal suspensions of platinum on carbon, platinum black, and carbon nanotubes, stabilized with PVP resulted in similarly porous, interconnected, three-dimensional nanostructures as in the case of pure CsH_2PO_4 solution, with the added benefit of even smaller feature size of 100 nm. Figure A2.8A-C show the stabilized nanostructures. Figure A2.8A,B depicts the platinum black and PVP stabilized structure after two days in ambient conditions and 12 hour dwell time at fuel cell operating conditions, i.e., 30% humidity and 240°C. From AC impedance measurements, we have some indication that the removal of surface PVP, deposited during the

electrospraying, enhances the electrodes' performance. On three separate samples, the impedance of electrodes with surface PVP present was ca. twice as large as of electrodes with surface PVP removed. Oxygen plasma treatment was identified to remove surface PVP but leave the morphology of the nanostructure intact. figure A2.9 shows the IR signal before and after plasma treatment. The main absorption peak of PVP at around 1600 cm^{-1} is not present in the plasma treated sample, while the extra peaks around 2300 cm^{-1} are most likely due to CO_2 adsorption on the sample surface.

A key finding of the presented work is the confirmation of structural stability of the nanocomposite electrodes, during normal fuel cell operating conditions. AC impedance measurements utilizing oxygen plasma treated platinum-black/ CsH_2PO_4 composite electrodes in a symmetric cell configuration over a 10 hour period show no significant electrode degradation. An electrode resistance of $4\ \Omega\ \text{cm}^2$ was observed with a platinum loading of $0.1\ \text{mg}\ \text{cm}^{-2}$, figure A2.10. A similar result is routinely observed for conventionally fabricated composite electrodes but with a platinum loading of $10\ \text{mg}\ \text{cm}^{-2}$.⁹

A2.4. Summary

The viability of the cheap and scalable, hence technologically relevant fabrication method of electrospray deposition as a solid acid fuel cell electrode fabrication tool has been demonstrated. A three dimensional, porous, interconnected CsH_2PO_4 nanostructure has been created with an average feature size of 100 nm. The stability of the nanostructure at fuel cell operating conditions (240°C and 30% humidity) over a time period of 10 hour has been shown. An electrode impedance of $4\ \Omega\ \text{cm}^2$ has been achieved with a platinum loading of $0.1\ \text{mg}\ \text{cm}^{-2}$. Further reduction of the electrolyte

feature size in order to match the size of the catalyst nanoparticles and increase the density of triple phase boundary sites, and an optimization of the electrode composition will be necessary to reach the state of the art electrode resistance reported in 2007.¹

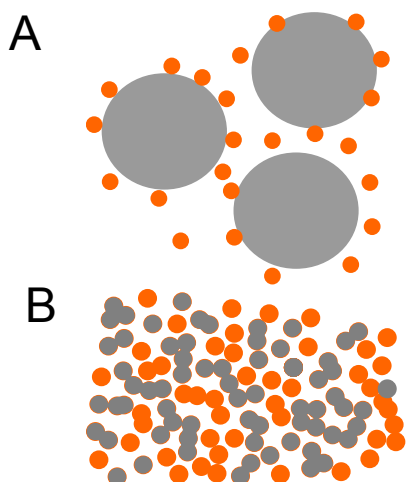


Figure A2.1. Fuel Cell Electrode Particle Size Comparison.

1A. Current state of the art solid acid fuel cell electrode: platinum nanoparticles with micron size electrolyte particles. **1B.** Composite electrode with equal catalyst and electrolyte particles size resulting in more catalytically active triple phase boundary sites.

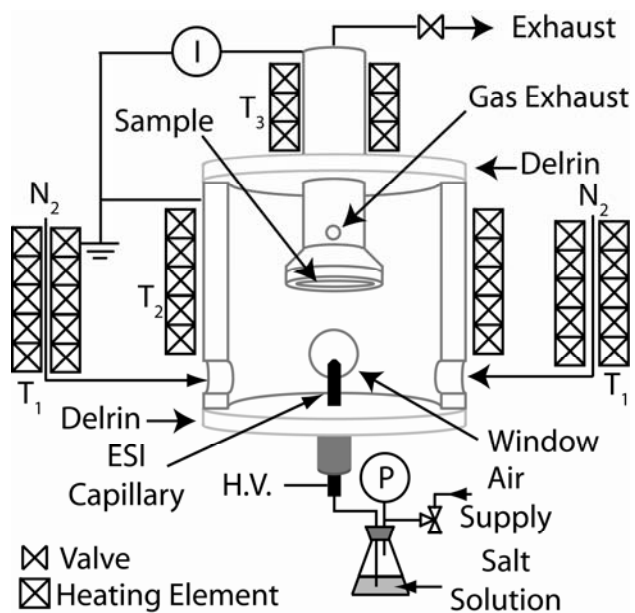


Figure A2.2. Schematic of the Electro spray.

Electrospray setup using inverted geometry.

Table A2.1. Critical Electrospray Parameters.

Critical electrospray parameters to be optimized for smaller feature size.

| Solution Properties | Electrospray Properties |
|--------------------------|---------------------------------|
| methanol concentration | solution flow rate |
| CDP concentration | nitrogen flow rate |
| solution surface tension | capillary to substrate distance |
| solution conductivity | temperature |

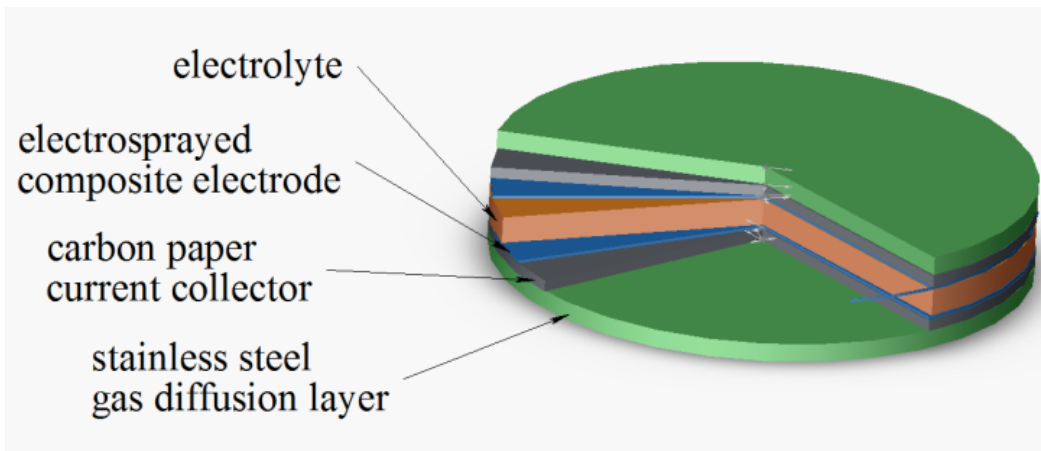


Figure A2.3. Fuel Cell Assembly.

Symmetric cell assembly.

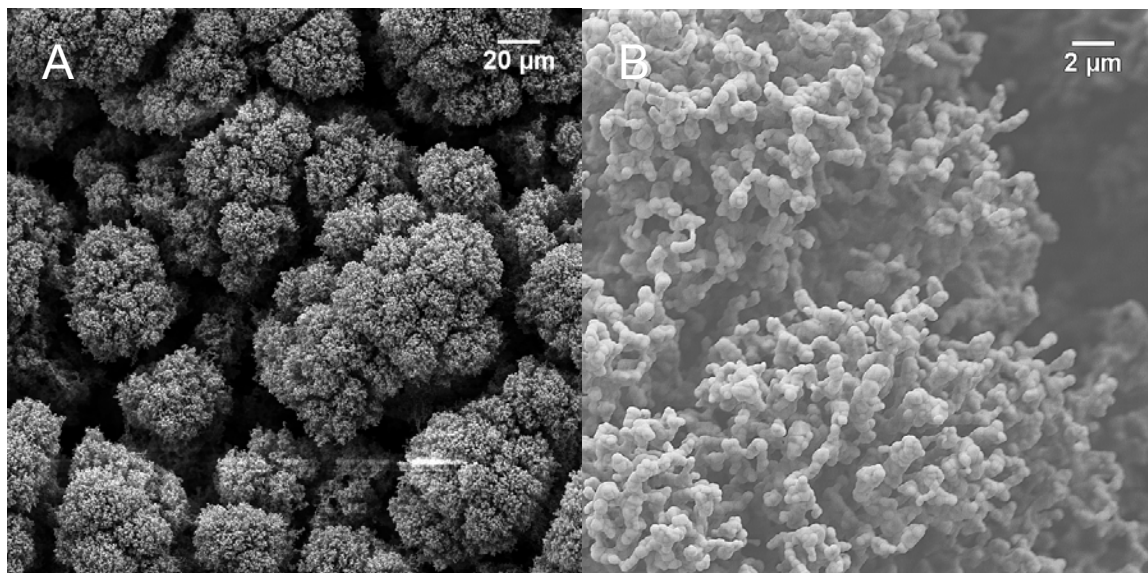


Figure A2.4. Nano-structured CDP.

4A. Porous interconnected three-dimensional CsH₂PO₄ structure obtained via electrospaying. **4B.** Electrospayed CsH₂PO₄ structure with average feature size of 300 nm.

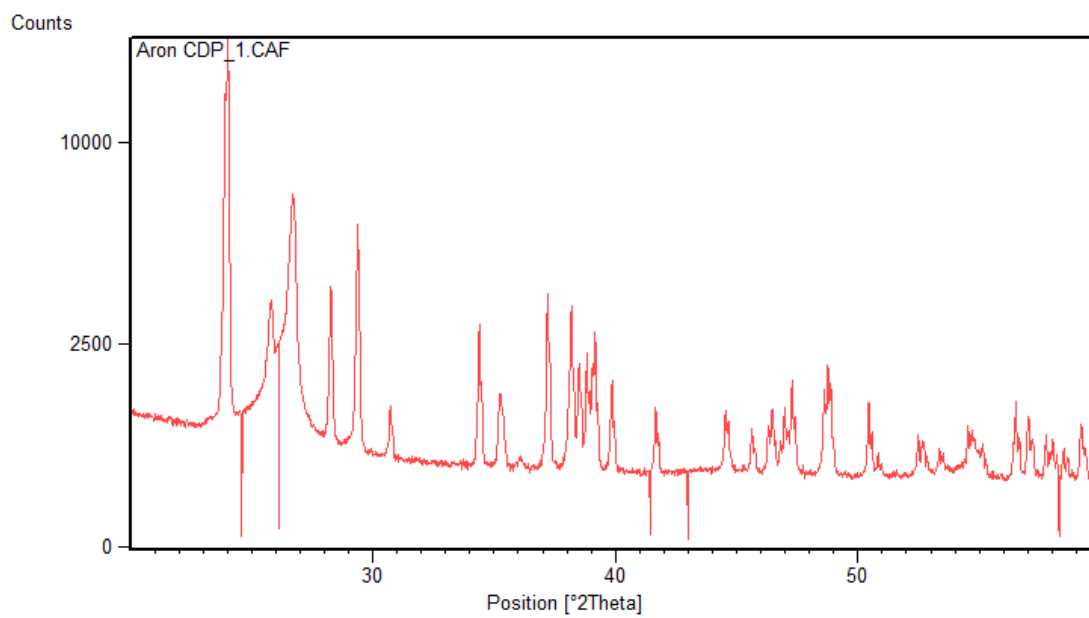


Figure A2.5. X-ray Diffraction of CDP.

X-ray diffraction pattern of electrosprayed CsH_2PO_4 .

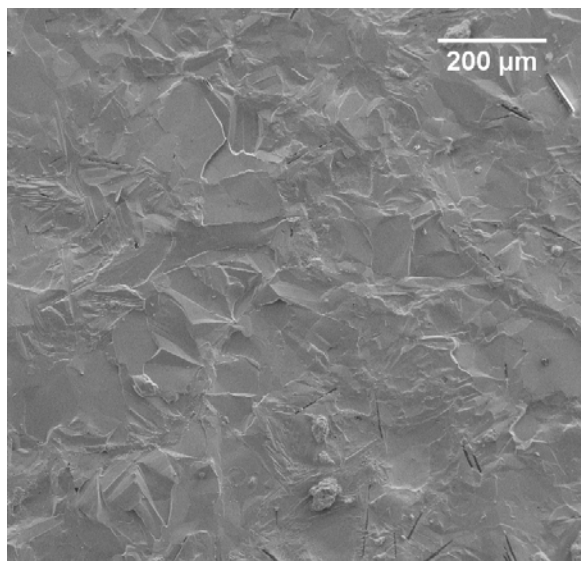


Figure A2.6. Dense CsH₂PO₄ Film.

Dense thin film of CsH₂PO₄ obtained via electrospray deposition.

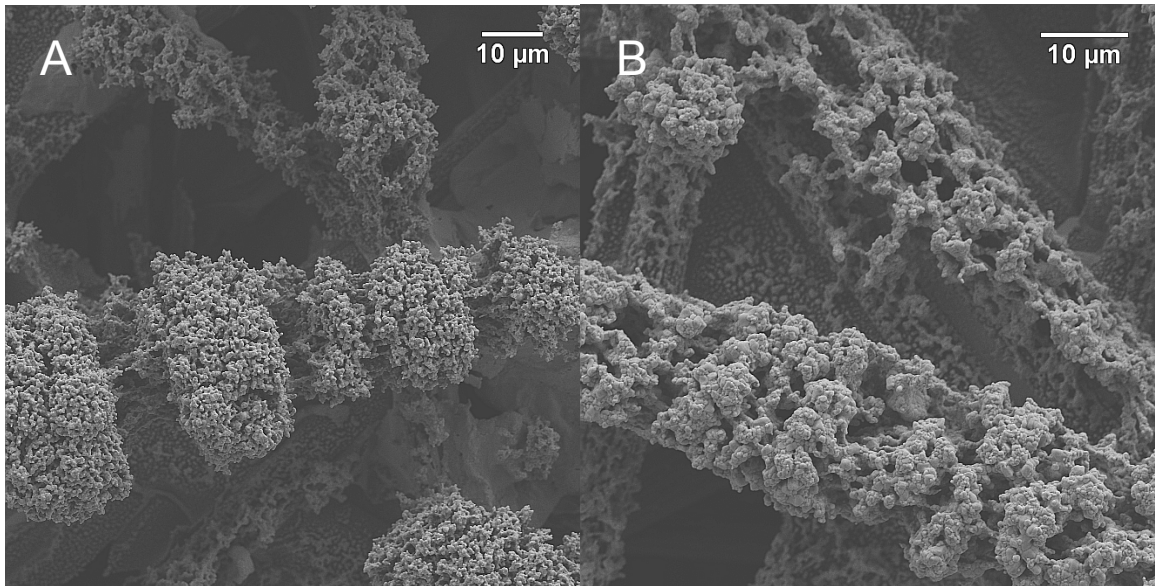


Figure A2.7. Effect of Aging on Nano-structure.

7A. Agglomeration of nanostructure after two days in ambient conditions. **7B.** Fully-collapsed CDP nano-structure after 7 days in ambient conditions.

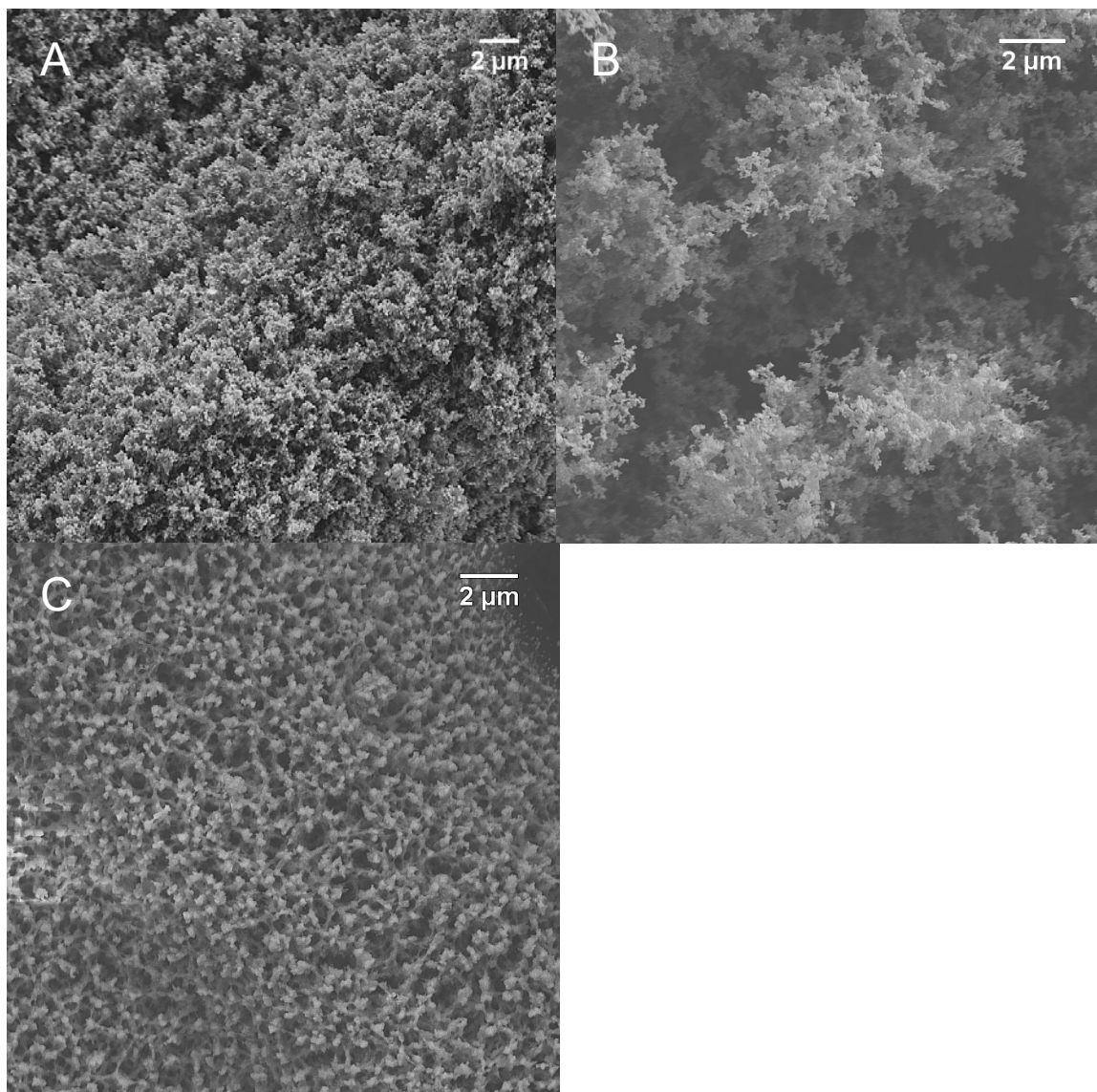


Figure A2.8. Stabilized Electrode Nano-structure.

8A. Platinum-black and PVP stabilized composite electrode nano-structure. **8B.**

Platinum on carbon and PVP stabilized composite electrode nano-structure. **8C.**

Multiwalled carbon nanotube and PVP stabilized composite electrode nano-structure.

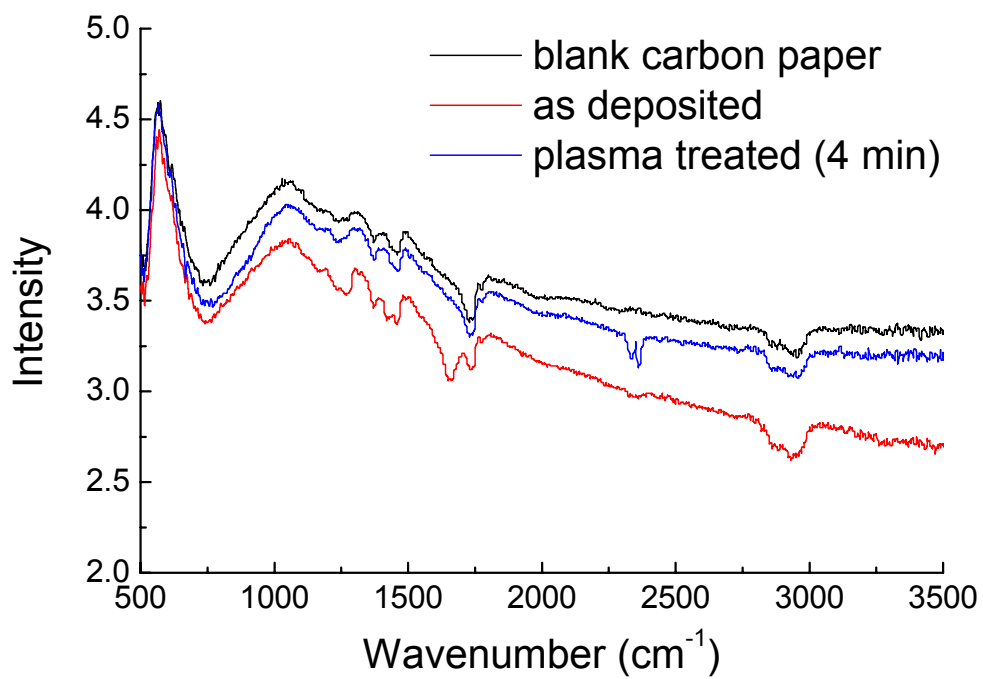


Figure A2.9. FTIR of Electro sprayed Electrode.

FTIR spectra of electro sprayed sampled before and after oxygen plasma treatment, confirming the removal of PVP.

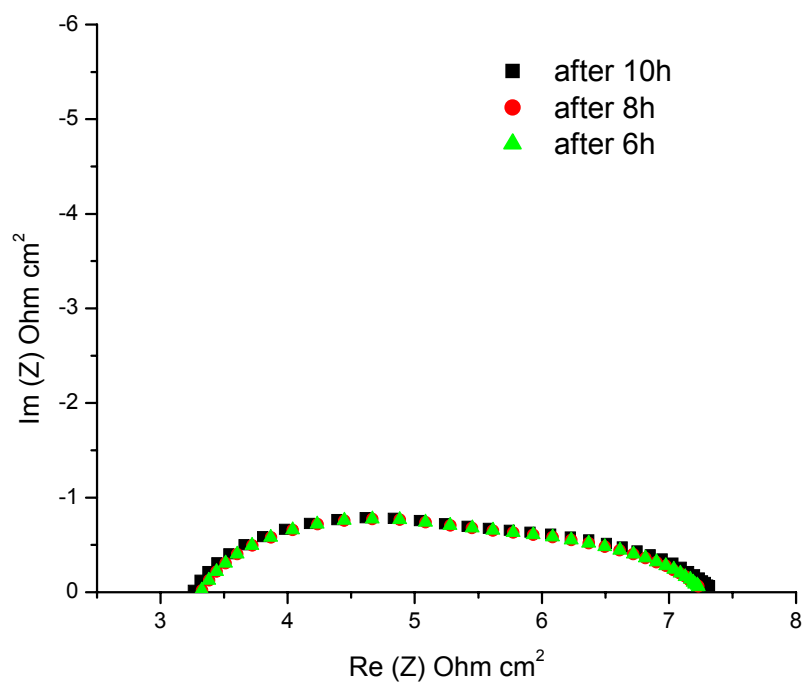


Figure A2.10. Impedance Plot

AC impedance spectra for electro sprayed nano-structured electrodes in a symmetric hydrogen gas and symmetric geometry configuration and a platinum loading of 0.1 mg cm^{-1} .

References

- 1 S. M. Haile, C. R. I. Chisolm, K. A. Sasaki, D. A. Boysen, T. Uda, *Faraday Discussions*, 2007, **134**, 17-39.
- 2 C. R. I. Chisolm, D. A. Boysen, A. B. Papandrew, S. Zecevic, S. Y. Cha, K. A. Sasaki, Á. Varga, K. P. Giapis, S. M. Haile, *Interface Magazine*, 2009, **3**, 53-59.
- 3 Adrian G. Bailey, *Electrospraying of Liquids*, New York, Wiley, 1988
- 4 G. Taylor, *Proceedings of the Royal Society of London, Series A, Mathematical Sciences*, 1964, **280**, 383-397
- 5 D. Perednis, L. J. Gauckler, *Journal of Electroceramics*, 2005, **14**, 103-111
- 6 I. Taniguchi, R. C. Van Landschoot, J. Schoonman, *Solid State Ionics*, 2003, **160**, 271-279
- 7 R. Benitez, J. Soler, L. Daza, *Journal of Power Sources*, 2005, **151**, 108-113
- 8 T. Uda, S. M. Haile, *Electrochemical and Solid State Letters*, 2005, **8**, A245-A246
- 9 K. A. Sasaki, Y. Hao, S. M. Haile, *in press*.

Appendix III: A Tool for Uniform Coating of 300 mm Wafers with Nanoparticles*

A3.1. Introduction

Semiconductor nanoparticles have attracted interest for a wide range of applications that take advantage of the special features that these materials acquire when fabricated into nanoscale structures. At sizes from subnanometer to a few tens of nanometers, quantum mechanical effects alter the optical and electronic properties of the semiconductor, producing quantized energy levels that make them behave as “artificial atoms”[1] or quantum dots whose properties can be tailored by tuning the nanocrystal size. Semiconductor nanocrystals have been used as fluorescent probes in biological imaging and analysis.[2-4] Metal and metal oxide nanoparticles have properties to exploit as catalysts[5-11] and photocatalysts.[12-14] Other proposed applications that take advantage of those special properties of semiconductor nanocrystals include light emitting diodes,[15-18] optical amplifiers[19] and lasers,[20] optically addressed memory,[21] and single-electron transistors.[22]

While applications of nanocrystals that take advantage of quantum size effects have received considerable attention, device fabrication remains a significant challenge

* This work was completed with Dean Holunga, who is a co-author.

due to difficulties of controlling nanocrystal size and placement, particularly with materials that are compatible with today's device fabrication infrastructure. Preventing process and tool contamination remains a major challenge when exotic materials or colloidal synthesis are considered, even though colloidal nanoparticles have been synthesized with precise control of size and optical properties for a wide range of materials, including silicon.[23-26]

Nevertheless, nanoparticle-based microelectronic devices have been fabricated without adverse effects on processing tools, albeit for less exotic applications. Tiwari and co-workers[27] proposed a silicon nanocrystal based memory to overcome the charge leakage that plagues conventional floating gate devices as they are scaled into the sub-100 nm size regime. Both devices are metal oxide semiconductor field effect transistor (MOSFET) structures that incorporate a floating gate to store charge. In the conventional device, the floating gate is a continuous semiconductor layer that is separated from the silicon substrate by a thin barrier tunnel oxide. To store or erase information, charge is induced to tunnel through an oxide layer into the floating gate. Unfortunately, any leakage path between the floating gate and the underlying channel will eventually dissipate all the stored charge. Tiwari's floating gate of isolated nanocrystals reduces the probability of complete information (charge) loss by separating the floating gate into a number of isolated storage elements within each transistor. The devices were fabricated by spontaneous decomposition during chemical vapor deposition. Feng, et al.[28] have produced nanocrystals in the floating gate by thermal annealing after ion implantation. Neither method affords direct control over the particle size distribution. Moreover, at least in the case of ion implantation, *in situ* nucleation leads to a distribution of

nanocrystals through the depth of the gate oxide.[29] The resulting variability in the nanocrystal-to-channel spacing leads to a distribution in leakage current over the area of the transistor. Ion implantation leads to a distribution of nanoparticle sizes at different depths,[29] presenting a challenge in obtaining a uniform tunneling distance between the gate and the nanocrystal.

Ostraat[30] demonstrated an alternate approach to creating a nanocrystal floating gate MOSFET. Silicon nanoparticles were produced as an aerosol by gas-phase thermal decomposition of silane. The silicon nanoparticles were then oxide passivated while still suspended in the carrier gas. The oxide layer was created on the aerosol nanoparticles in two ways: (1) by chemical vapor deposition of tetraethylorthosilicate (TEOS), or (2) by high temperature oxidation (HTO) of the surface of the aerosol silicon nanoparticles. After oxide passivation, the core/shell nanoparticles were deposited by thermophoretic diffusion onto a previously prepared tunnel-barrier oxide on 200 mm diameter silicon wafers. The HTO-passivated nanoparticles met the stringent contaminant limits and were processed to produce high performance devices through an industrial fabrication facility.[31]

Although the devices produced by Ostraat, et al. showed excellent performance characteristics and demonstrated that aerosol-synthesized silicon nanocrystals can safely be taken through conventional device lithography and etching processes, many aspects of the synthesis require further development before such processes see commercial applications. Foremost is discomfort of tool owners with taking particle laden wafers into the fabrication facilities, a problem that will require addressing a number of real and imagined hazards to the process equipment. Questions about the entrainment of

nanoparticles from wafer surfaces[32-36] and, especially, about the existence of agglomerates that might more easily detach can only be addressed once suitable nanoparticle-coated wafer samples can routinely be processed for testing.

The original nanoparticle synthesis employed a low-throughput, multistage laminar flow aerosol reactor that enabled precise control of the size and structures of the product nanoparticles, but that produced relatively low number concentrations, $1 * 10^6$ to $3 * 10^6 \text{ cm}^{-3}$, in 1500 sccm carrier gas flow rates. Nanoparticle coverage of a 200 mm wafer, dense at the center and sparse near the edge, required from 4 to 12 hours for each wafer, far too long for a production process. Extension to similar coverage of the 300 mm wafers would, at a minimum, double this deposition time.

Numerous groups have demonstrated much higher nanoparticle synthesis rates than that of Ostraat. Flame synthesis[37-40] reactors produce hundreds of grams per hour in the laboratory, and kilograms or more in industrial reactors, but are not suitable for the materials of interest here. Laser-induced decomposition[41-43] and plasma synthesis[44-45] can produce large quantities of silicon or other non-oxide nanoparticles, but the precise control of the state of agglomeration achieved by Ostraat, et al. remains a challenge. Recently, Holunga[46] et al. demonstrated a higher throughput multistage reactor that employs turbulent mixing and short residence times to improve on the particle properties achieved in the laminar flow aerosol reactor. The short residence time allows number concentrations as high as 10^9 cm^{-3} to be processed with minimal agglomeration. The resulting heterogeneous core/shell Si-SiO₂ aerosol nanoparticles provide an enabling technology for accelerated nanoparticle device processing.

While the deposition chamber used in early aerosol nanoparticle device synthesis demonstrated the potential of the approach, the areal density of deposited nanoparticles varied significantly over the surface of the wafers. While this proved useful in initial studies of device properties by enabling a range of devices to be produced in a single experiment, production tools will have to produce deposits that are uniform over the entire surface of larger (300 mm) production wafers.

The present chapter focuses on the latter challenge. The discussion that follows reports on the design and characterization of a nanoparticle deposition tool for coating of 300 mm silicon wafers with aerosol synthesized core/shell nanoparticles produced using the multistage turbulent mixing aerosol reactor.

A3.2. Design

The deposition chamber, illustrated schematically in figure A3.1, consists of two radially mounted parallel plate heating and cooling surfaces. The aerosol is introduced and removed orthogonally through 1/2" OD SS tubing at the center of the wafer. Three concentric heat sources provide a nearly uniform heat flux to the top plate. The bottom plate is cooled using a heat transfer fluid.

For radially outward, isothermal flow of a Newtonian fluid between flat plates, and in the creeping flow limit, the velocity profile as a function of z (height) and r (radius) is[47]

$$v_r(r, z) = \frac{3Q}{4\pi r Z} \left(1 - \left(\frac{z}{Z} \right)^2 \right), \quad (\text{A3.1})$$

where Q is the volumetric flow rate, z is the normal distance from the midplane between the plates, and Z is half the distance between the plates. This profile remains only

approximately valid if a small temperature gradient exists between surfaces; however, for a small ΔT at relatively large absolute T , the important characteristic remains that the velocity in the radial direction decreases as r^{-1} .

The thermophoretic velocity for ultrafine particles, v_{th} , can be described as[48]

$$v_{th} = -Th \frac{\mu}{\rho T} \frac{\partial T}{\partial z}, \quad (A3.2)$$

where ρ is the density, μ is the viscosity of the effluent gas, T is the absolute temperature, and z is the coordinate of directional movement. The dimensionless number, Th , has been experimentally determined to be about 0.5.[49] If the absolute temperature is relatively high enough and the temperature gradient remains similar between the plates at all radial positions, then the z-axis thermophoretic velocity is nearly constant throughout the chamber.

The surface area being covered increases as the flow expands radially outward from the center of the wafer.

$$\frac{\partial A}{\partial r} = 2\pi r = C(r). \quad (A3.3)$$

Since the deposition rate needed is proportional to both $v_{avg}(r)$ and $C(r)$, while the velocity of the feed particles is decreasing with r^{-1} , any r dependency in deposition can be eliminated using radial geometry. Ignoring Brownian diffusion, a constant deposition velocity from the z direction should yield a homogeneous deposition flux at all locations on the wafer. With a robust design allowing flexibility in adjusting flow rates and temperature gradient, a suitable operating condition can be reached that would yield uniform deposition.

The critical feature for this deposition chamber is ensuring non-separating laminar flow through the nozzle and preventing re-circulating flow. Aerosol in recirculation zones may agglomerate and either deposit on the chamber walls or re-enter the deposition flow and be driven to the collection surface in a non-desired size and configuration.

The nozzle shape was determined using a potential flow argument, in rectilinear coordinates, for stagnation flow around a corner. This approximation is locally valid as the nozzle begins to bend since the boundary layer is developing through the radius of the bend and also outward from the stagnation point above the wafer, approximating open channel non-viscous flow. In physical terms, the combination of a larger diameter inlet tubing, a small power-law hyperbolic nozzle (small change in r) and a narrow gap allowed the flow field to be approximated in rectilinear coordinates. The classical fluid flow field for an open channel incompressible laminar flow field around an L-shaped corner can be described by the vector equation,

$$\hat{v} = Ax\hat{i} - Ay\hat{j}, \quad (\text{A3.4})$$

where x and z are the coordinates and A is an arbitrary constant dependent on the volumetric flow rate within the dimensions of the structure. The flow field solution is a hyperbolic family of streamlines, $\varphi = xy$, wherein the channel width w (from the y -axis) is identical to channel height h from the x -axis. By symmetry, a point on a curve at $\varphi(a, b)$ is also on the same streamline at $\varphi(b, a)$. Each streamline acts as a "pressure" wall to the fluid on either side of the streamline. A physical wall could be inserted without altering the stream function. The stream function for non-equal channels, $w \neq h$, is such that a fluid element entering at (wx_0, hy_0) might be constrained to find the point (wy_0, hx_0) on the way out. If so, the vector flow field above is transformed,

$$\hat{v} = Awxi\hat{i} - Ahyj\hat{j} . \quad (\text{A3.5})$$

Using the stream function approach with,

$$-\frac{\partial\varphi}{\partial x} = v_y = -Awy , \quad (\text{A3.6})$$

$$\frac{\partial\varphi}{\partial y} = v_x = -Ahx , \quad (\text{A3.7})$$

yields the separable differential equation,

$$\frac{\partial y}{\partial x} = \frac{wy}{hx} , \quad (\text{A3.8})$$

and a solution of the form,

$$xy^{-\frac{h}{w}} = Constant , \quad (\text{A3.9})$$

which describes a family of power law hyperbolic-type streamlines. A properly chosen streamline can be used to form the equation for the nozzle curve, with the nozzle shape described as

$$\varphi = \varphi_0 = (x - x_0)(y - y_0)^{-\frac{h}{w}} , \quad (10)$$

provided that dynamical pressure inequalities do not lead to flow separation. This stipulation simply requires that the maximum flow velocity be essentially unchanged through the bend as the fluid leaves the nozzle and begins to traverse the deposition surface.

In two-dimension axisymmetric flow, i.e., cylindrical coordinates, the stream function solution to stagnation flow[49] from a jet is $Constant = r^2z$. In the chamber, the actual ratio of w/h is 2.65. Applying the offset, (x_0, y_0) to the rectilinear solution,

effectively chose a streamline very close to the axes (small r) in which the error in the exponent became negligible.

This curve chosen should also smoothly join with the inlet tubing wall and the top plate of the chamber and be symmetric in the azimuthal. When the maximum flow velocity through the nozzle is similar to the maximum flow velocity of the gas in the inlet tubing, the dynamical pressure varies little, and streamlines remain intact. Acceleration or deceleration of gas through this region would give rise to pressure boundaries beyond which recirculation zones could appear. Particles trapped in recirculation pockets will agglomerate and eventually settle out, preventing homogenous coverage of a surface with particles of equivalent size.

The heater/chamber was modeled in Fluent using a laminar flow two dimension axisymmetric solver. The dimensions of an actual MDC flange were used in creating the model chamber. Incoming aerosol flow, 1500 sccm, was provided an entrance length sufficient to develop a parabolic velocity profile. The top flange was heated with ring-heaters that were assumed to be able to provide a constant heat flux, figure A3.1, or constant temperature, and the water coolant (which would have turbulent flow) was assumed to have heat removal capacity such that the metal in contact with the coolant was only 5–10 K above the incoming water temperature. A 3D $\kappa - \epsilon$ turbulent model for the cooling water limits was also modeled, figure A3.2, wherein 30 LPM of water at 300 K is diverted into two opposing tangentially outward jets to cool 1800 W of energy transferred to the outer surface. The heat transfer coefficient for the top surface included conduction through a zone corresponding to the stainless steel MDC flanges as well as

convection into a laminar flow gas. The modeled temperature rise of the coolant is less than 10 K.

With a working nozzle geometry determined, the Fluent model was run using a constant flux (power) source for the heaters rather than a constant temperature boundary condition. The necessary conditions of nearly uniform temperature gradient and adequate heat removal were also met in this scenario.

At a concentration of 10^9 cm^{-3} monodisperse 10 nm aerosol nanoparticles have a characteristic agglomeration time constant of $\tau_a \sim 1 \text{ s}$. The chamber operation must be robust enough to allow for higher flow rates of diluted nanoparticles should agglomeration need to be suppressed during the deposition process. Figures A3.3–A3.4 shows modeled velocity profiles of 1500 sccm, 15,000 sccm, 30,000 sccm, and 60,000 sccm. The modeling indicates that flow rates up to 15,000 sccm are possible when employing a 2 mm gap between the wafer and heated top plate.

Wafer curvature is commonly seen in large wafers exposed to thermal gradients such as those found in plasma etch processes. The potential of having wafer curvature arising from the axial variation in thermal expansion was briefly investigated. Assuming isotropic expansion, a constant thermal expansion coefficient of $\sim 4 * 10^{-6} \text{ K}^{-1}$, an axial temperature change of 1 K (about 5 times larger than modeled predictions) through a 50 μm wafer, the predicted radius of curvature of in a 300 mm wafer is $\sim 125 \text{ m}$. The predicted variation in height from center to edge is less than 0.1 mm. Although the curvature is minimal in this apparatus, the variation in height scales linearly with the temperature drop. Thus, wafer curvature may have a significant effect on deposition

patterns at larger temperature gradients. Greater deposition nearer the edges would be expected as the flow slows at a rate greater than r^{-1} .

A3.3. Experimental Apparatus and Methods

Oxide-coated silicon nanocrystals are produced in a turbulent mixing aerosol reactor described previously.[46, 50] A fraction of the stream is monitored continuously by a radial differential mobility analyzer[51-55] (RDMA) and a fA-resolution electrometer. The remainder of the 8–12 nm particle stream, with a concentration of $\sim 10^8 \text{ cm}^{-3}$ and $\sigma_g \approx 1.1$, is sent via 1/4" stainless steel tubing to the deposition chamber inlet.

The deposition chamber consists of two modified MDC 18" stainless steel vacuum flanges that serve as radially mounted parallel plate heating and cooling surfaces. The aerosol is introduced orthogonally through 1/2" O. D. stainless steel tubing above the top plate at the wafer center and removed orthogonally at the wafer center from below through the bottom plate. Two concentric ring heaters and a third side-mounted band heater with a concentric ring-connected mount provide a nearly uniform heat flux to the top plate. A hollowed annulus in the bottom plate allows for heat transfer through the flange to a cooling fluid. Re-circulated cooled water at 293 K at a flow rate of 30 LPM cools the bottom flange. The coolant is sealed using a stainless steel covering plate with a Viton O-ring gasket. A small bi-directional nozzle is employed to provide equal coolant fluid flow around either perimeter of the water jacket. A single drain is located radially opposite the coolant source. A flat Viton gasket separates the two flanges, serving as a thermal resistor to provide a more uniform temperature profile between the flanges.

The top plate is supported by three stainless steel legs. The bottom plate rests on a stainless steel jack that is manually raised and lowered during loading/unloading operations. All stainless steel surfaces are electropolished.

To maintain a uniform top plate temperature, each heating element is powered through a Eurotherm 7100A thyristor monitored with thermocouples and PID controllers. The temperature profile and streamlines from a two-dimension axisymmetric solver in Fluent are shown in figures A3.5–A3.6. A flow rate of 1500 sccm was used. The temperature drop from top plate to the wafer remains relatively uniform across the entire deposition region from the center, figure A3.5A, to the edge of the wafer, figure A3.5B. However, to avoid a region of sparse deposition from a reverse temperature gradient, observed in the modeling, when the aerosol is introduced relatively cold, a heating tape, thermocouple, and PID assembly are used to preheat the inlet aerosol.

Figure 6 shows the corresponding streamlines for 1500 sccm flow to the modeled temperature profiles shown previously. Streamlines are parallel through the nozzle bend, figure A3.6A, and over the wafer surface. Beyond the edge of the wafer, from the geometry imposed using this particular size of MDC flanges, figure A3.6B, a recirculation pocket exists. However, this should have no effect on particle deposition over the wafer substrate.

Wafers are loaded using quartz-sleeved stainless steel forks and rest upon three quartz or Teflon pegs in the chamber, providing a uniform wafer to plate distance and preventing contact with metal surfaces. The wafer is physically situated 2 mm below the heated top plate. With the absolute temperature relatively high, and the temperature gradient relatively large and uniform, small radial variations in temperature have little

effect on thermophoretic transport. The quartz/Teflon pegs sit in machined depressions and the pegs are removable and replaceable. The adjustable height of the wafer adds another degree of freedom in determining thermophoretic velocity.

AFM samples were drawn from a center strip of a 150 mm [100] Si wafer that was tiled into 14 squares sized 1 cm x 1 cm using a wafer saw or cut into similar sized pieces using a diamond-tipped scribe. Before deposition, the tiled pieces were cleaned by sonication in methanol, rinsed in deionized water, and dried using a jet flow of nitrogen. The tiled wafer was reconstructed on an intact wafer in the chamber, with the two “halfmoon” pieces secured using stainless steel clips.

All stainless steel surfaces were electropolished and cleaned with methanol prior to use within the cleanroom environment.

Non-contact AFM images were acquired over 512 x 512 resolution from a 5 μm x 5 μm grid. The AFM tip was estimated to be ~30 nm in diameter. Particle counts over the entire grid to determine coverage are reported in figure A3.12B and represent ~2000 particles per image.

A3.4. Results

Additional modeling of particle transport was conducted using Femlab. The results are shown in figures A3.7–A3.10. The model used was a laminar flow, two-dimension axisymmetric representation of the deposition chamber. Temperature boundary conditions were imposed based on the results obtained earlier using Fluent, creating a temperature drop of ~30 K between the heated chamber top and the wafer. For simplicity, the particles are treated as a continuum species with uniform inlet concentration and temperature. The particles are subject to convection and

thermophoresis as they travel through the chamber. Brownian diffusion is imposed for a single mode particle size, 10 nm, but particle loss to walls other than the wafer surface is neglected.

Figure A3.7 shows the particle distribution in the chamber with uniform top and bottom temperature, $\Delta T = 165$ K, and the incoming aerosol-laden N_2 15 K cooler than the chamber top. Figures A3.8–A3.10 show results for increasing flow ratios. A flow rate of 1600 sccm leads to insufficient deposition on the outer edge of a 300 mm wafer, but would be sufficient for a 150 mm wafer. The arrows in the figures indicate thermophoretic flux, $v_{th}c$, and that uniform deposition is predicted over the central portion of the wafer. Increasing the flow rate to 3600 sccm results in uniform deposition on a 300 mm wafer, figure A3.10, but is only achieved when some particles bypass deposition. At intermediate flow rates, uniform deposition coverage extends outward with increasing flow rate, while deposition rate decreases for similar aerosol inlet concentration. figure A3.11 summarizes these model observations. Near $r = 1$ mm, each trace predicts some inconsistency in the deposition uniformity. This perturbation could be reduced in the model, similar to that observed in the 3600 sccm trace, by adjusting the inlet temperature a few degrees lower, depending on the flow rate.

To examine the deposition uniformity attained by the deposition tool, silicon nanoparticles were deposited on a 150 mm wafer for 80 min with an aerosol flow rate of 1600 sccm and an aerosol concentration of $2 * 10^8 \text{ cm}^{-3}$. As seen in the images in figure A3.13, the coverage was kept well below the monolayer than would be sought in device fabrication to facilitate quantitative areal density measurements. The particle size distribution of this test aerosol is shown in figure A3.12A. The major mode in the

distribution was 8.5 nm. The minor second mode at ~11 nm reveals that limited (~10%) aggregation occurred between the outlet of the synthesis reactor and the RDMA. The areal density of the deposited particles, shown in figure A3.12B, is quite uniform, varying less than $\pm 5.5\%$ over the radial and azimuthal by distributed samples probed.

Modeling in Fluent indicated that the particle stream needed to be preheated to a temperature within ~ 20 K of the hot plate temperature to achieve deposition uniformity at the wafer center. A temperature too high produced a correspondingly larger thermal gradient near the center and the modeled deposition rate exceeded that of the outer surface. If too cool, figure A3.14, then the model predicts insufficient or no deposition at the center. Heat transfer within the silicon wafer is faster than through the aerosol-containing N_2 , raising the temperature of the wafer center above that of the heated inlet stream, and driving particles away from the wafer.

The reversed temperature gradient was also predicted with modeling in Femlab, as seen in figures A3.15–A3.16. The magnitude of the thermophoretic flux away from the wafer is several times that of the flux toward the surface, indicating that the reversed temperature gradient is much greater.

A3.5. Conclusions

A 300 mm capable laminar flow thermophoretic deposition device demonstrates near uniform coverage of nanoparticles on a 150 mm wafer. Modeling suggests device operation is robust over a wide range of flow rates. A sparse array of particles randomly oriented over the surface was stably attached and remained adhered over a two-month period in which characterization by AFM was performed. Longer deposition times are expected to maintain deposition uniformity and yield coverage approaching monolayer.

Deposition of nearly monodisperse nanoparticles may also self-assemble into close-packed structures, provided that agglomeration in the aerosol phase is avoided. Device fabrication with aerosol nanoparticles deposited using thermophoresis remains a potential new process for meeting narrower bandwidth requirements or producing new devices in which the nanoparticles' spatial positioning must meet tight tolerances.

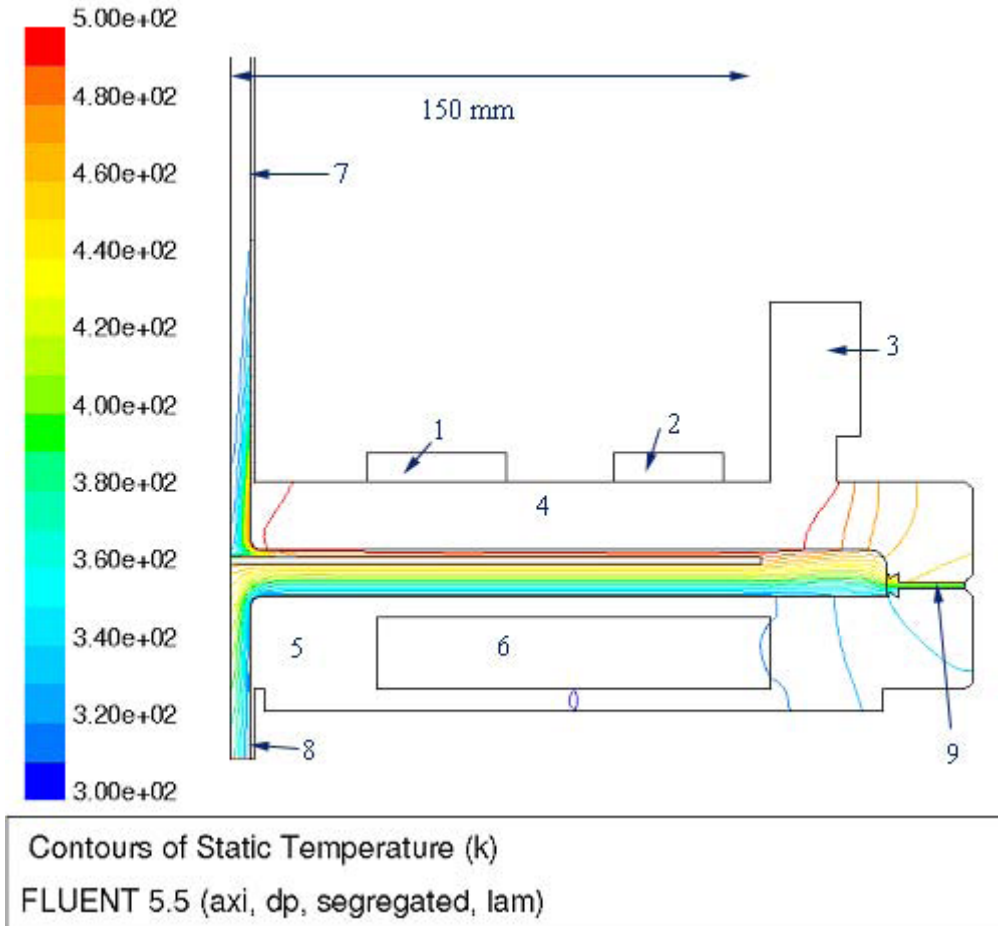


Figure A3.1. Schematic of Thermophoretic Depositor with Isotherms.

Isotherms of deposition chamber modeled in Fluent. Components of chamber: 1. Inner ring heater. 2. Outer ring heater. 3. Band heater and mount. 4. Top MDC stainless steel Flange. 5. Bottom MDC stainless steel Flange. 6. Water cooling chamber. 7. Aerosol inlet. 8. Gas outlet. 9. Viton Gasket. Modeled average current supplied to the heaters (with listed power capacity) as follows: 1. Inner ring heater, 0.4 A/1000 W, middle ring heater, 2. 0.6 A/1500 W, 3. Outer band heater 7.5 A/1500 W.

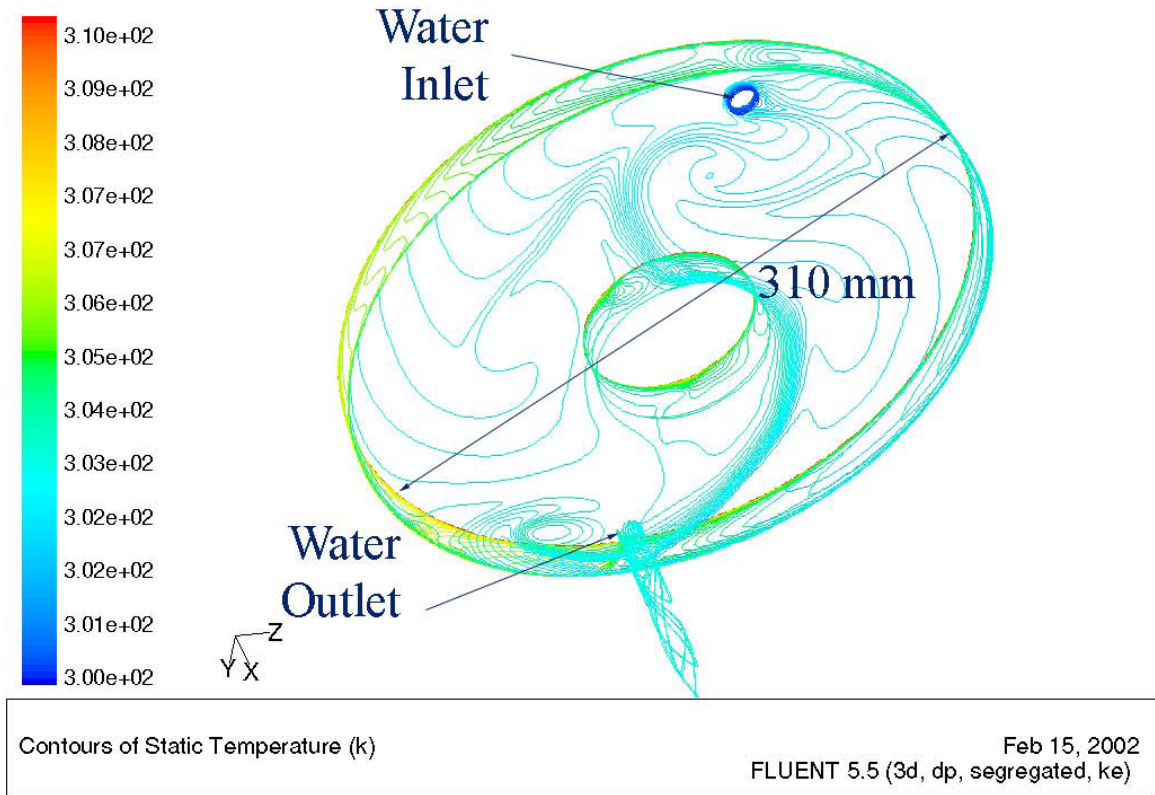


Figure A3.2. Modeled Temperature Profile.

Modeled temperature rise for a constant 1800 W heater on the outer band and top of a water-cooled chamber with 30 LPM flow rate.

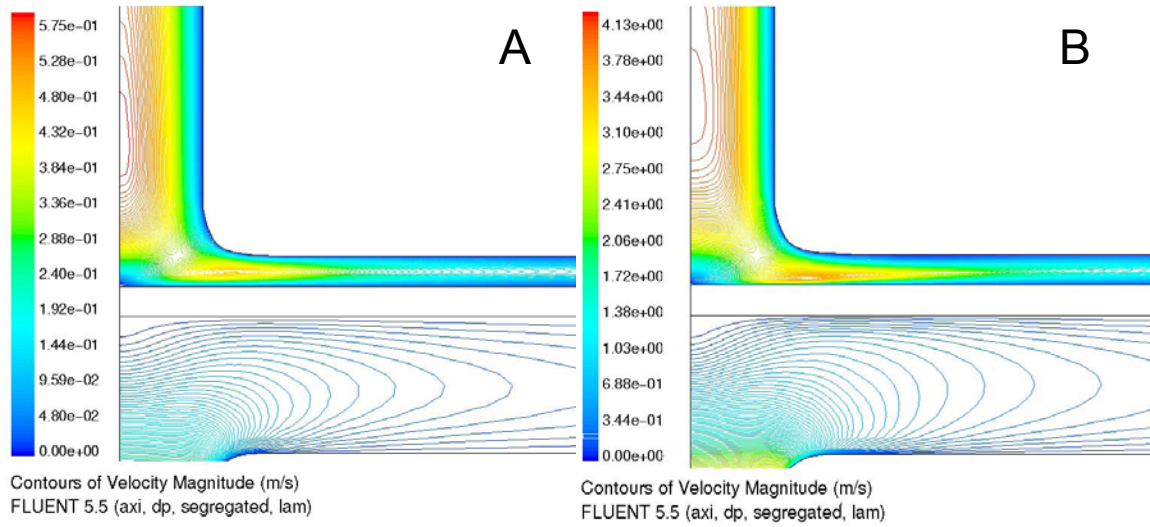


Figure A3.3. Modeled Velocity Contours for Flow Rates of 1.5 and 15 SLM.

Velocity contour plots for flow rates (A) 1500 sccm and (B) 15,000 sccm without separation as modeled in Fluent.

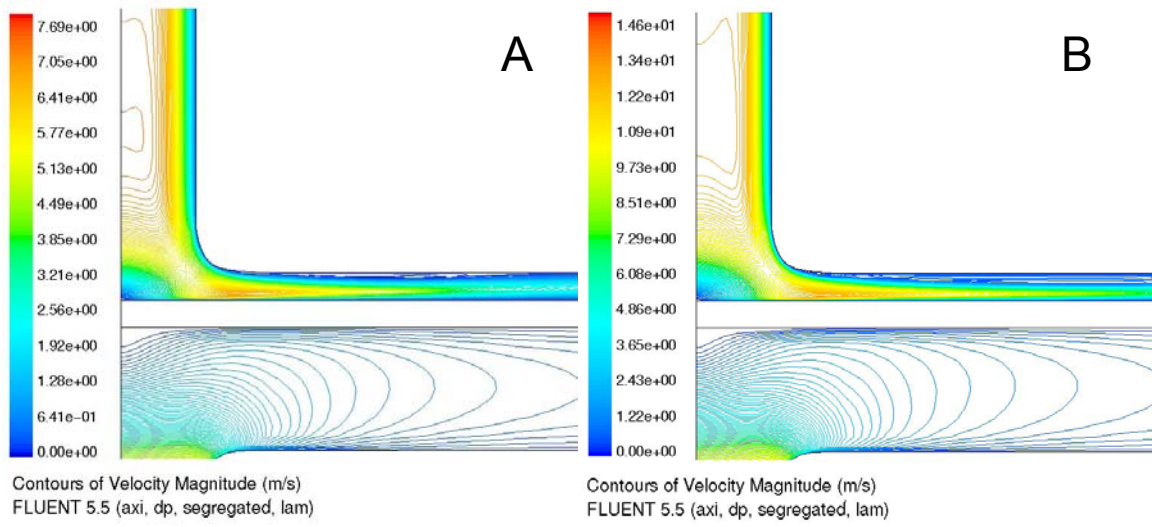


Figure A3.4. Modeled Velocity Contours for Flow Rates of 35 and 60 SLM.

Velocity contour plots for flow rates of (a) 35,000 sccm (b) 60,000 sccm with separation as modeled in Fluent.

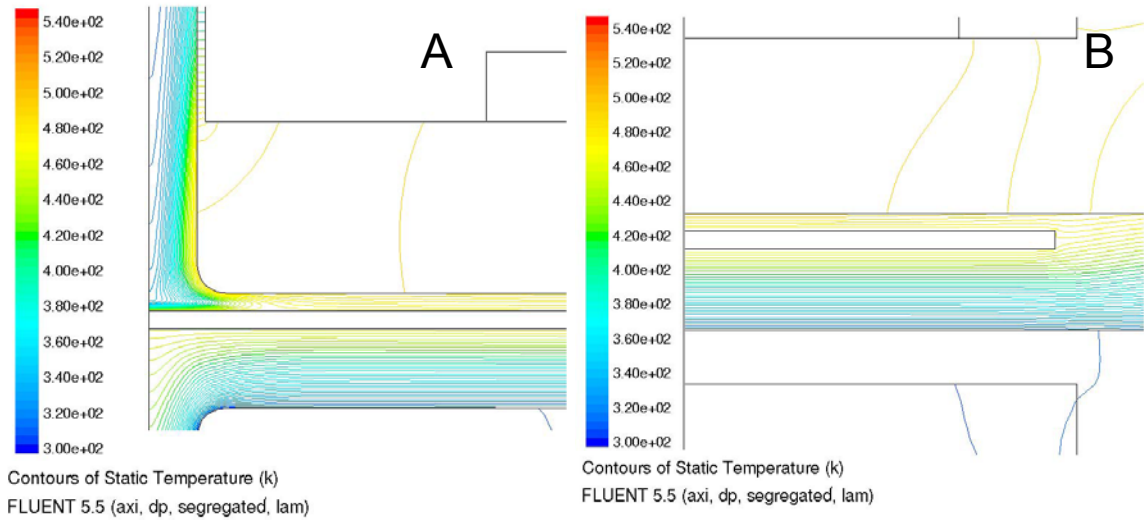


Figure A3.5. Modeled Temperature Contours.

Temperature contour plots modeled in Fluent. (A) Modeled temperature profile at the inlet and outlet region. (B) Modeled temperature profile at the edge of wafer region.

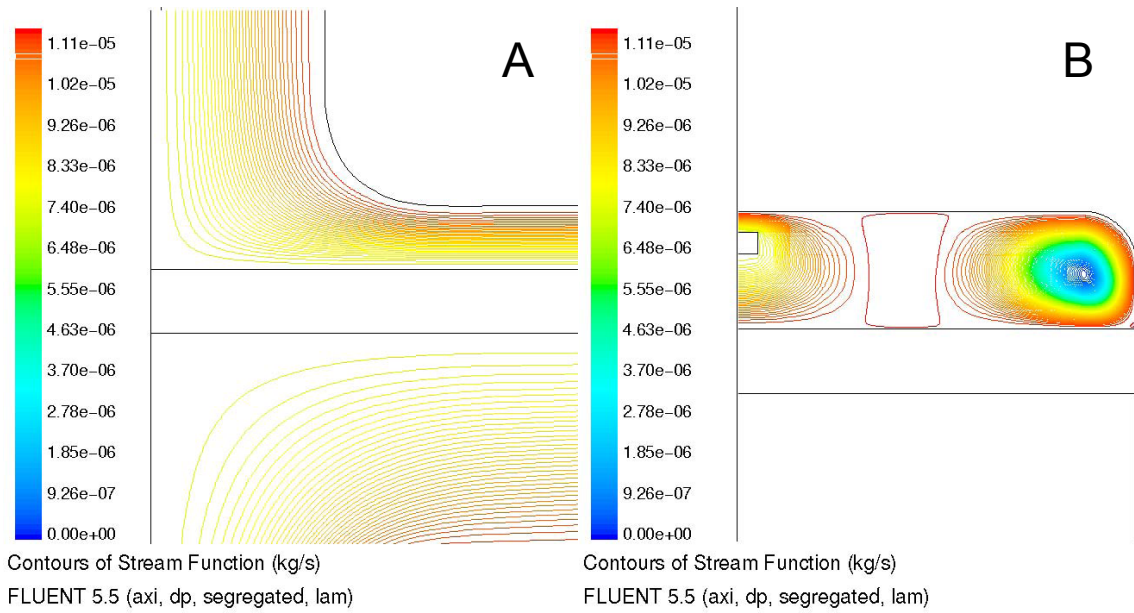


Figure A3.6. Modeled Stream Function Plots.

Stream function plots modeled in Fluent for flow rates of 1500 sccm. (A) Modeled streamlines at the inlet and outlet region. (B) Modeled streamlines at the edge of wafer region.

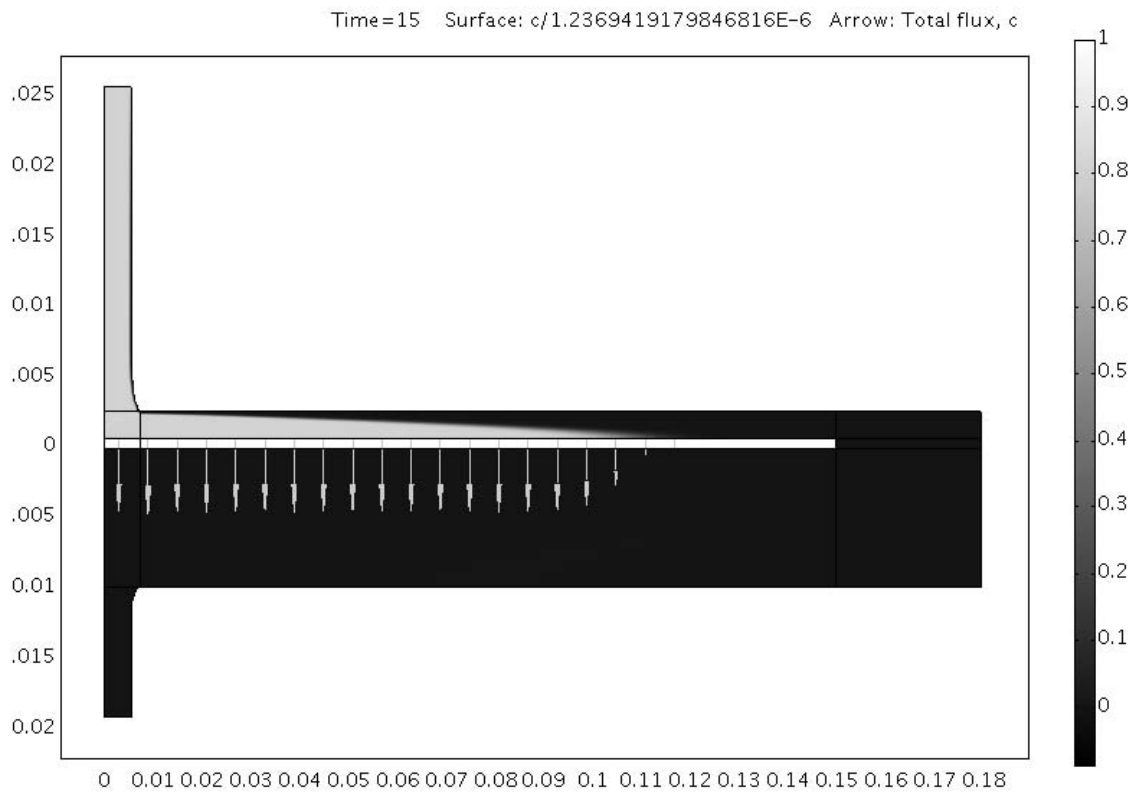


Figure A3.7. Modeled Deposition Profile.

Normalized particle deposition and concentration at 1600 sccm modeled in Femlab.

Arrows indicate particle flux rate at the wafer surface.

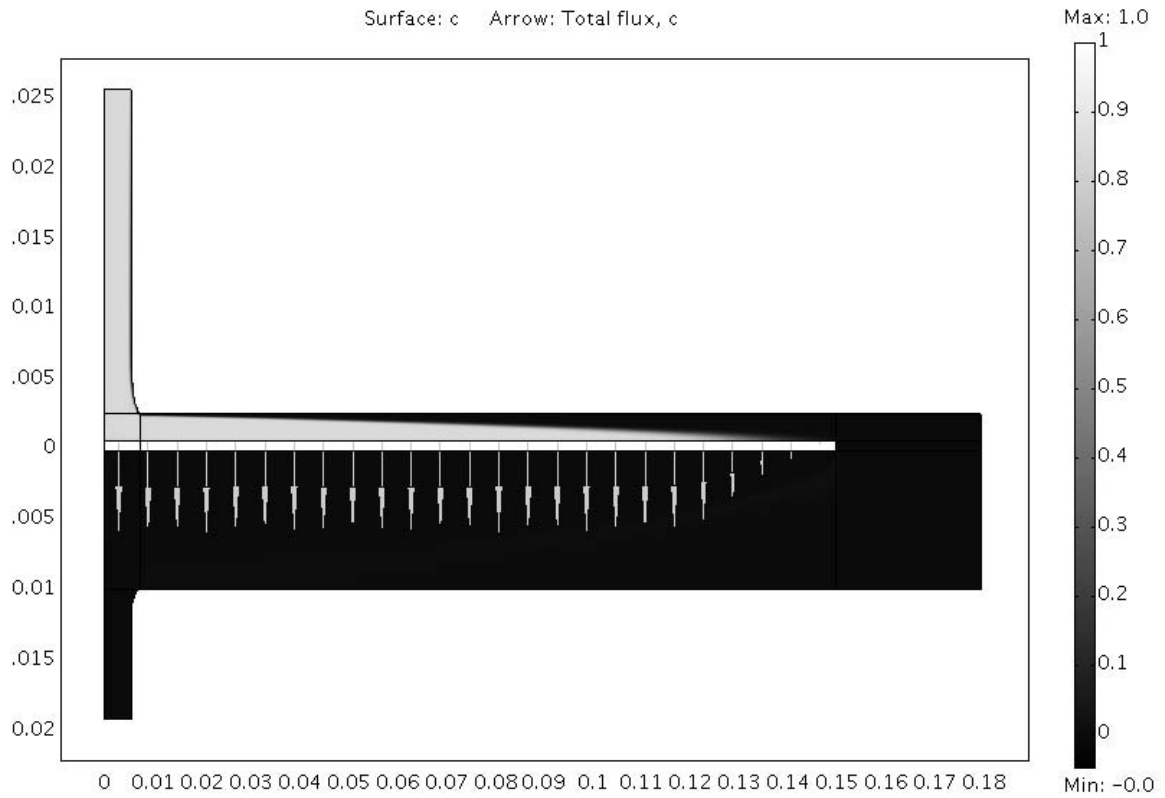


Figure A3.8. Modeled Deposition Profile.

Normalized particle deposition and concentration at 2400 sccm modeled in Femlab.

Arrows indicate particle flux rate at the wafer surface.

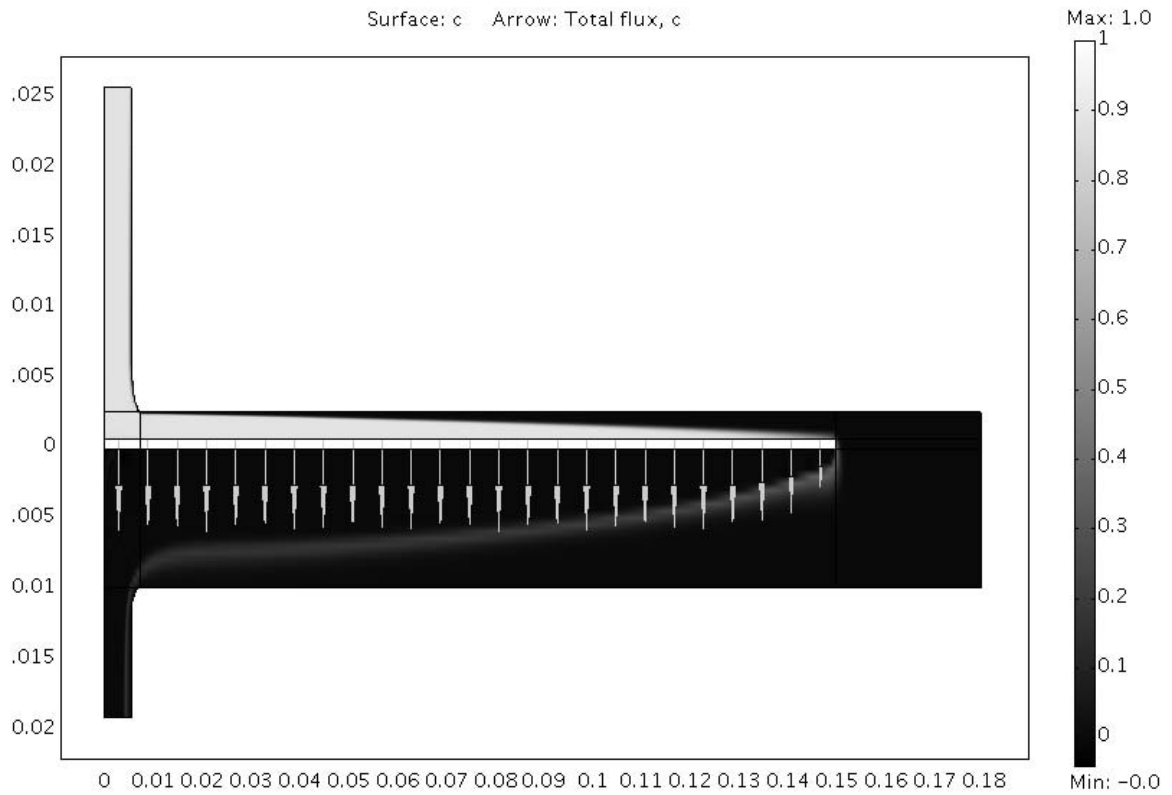


Figure A3.9. Modeled Deposition Profile.

Normalized particle deposition and concentration at 3000 sccm modeled in Femlab.

Arrows indicate particle flux rate at the wafer surface.

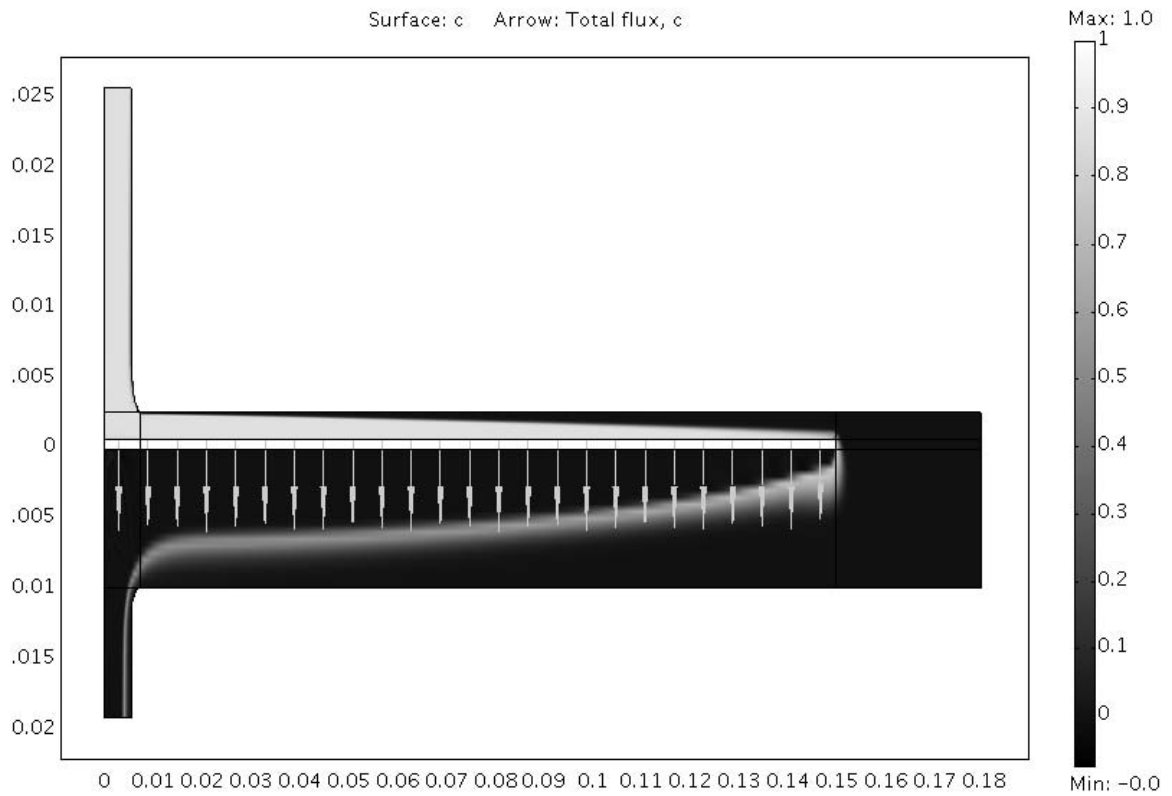


Figure A3.10. Modeled Deposition Profile.

Normalized particle deposition and concentration at 3600 sccm modeled in Femlab.

Arrows indicate particle flux rate at the wafer surface.

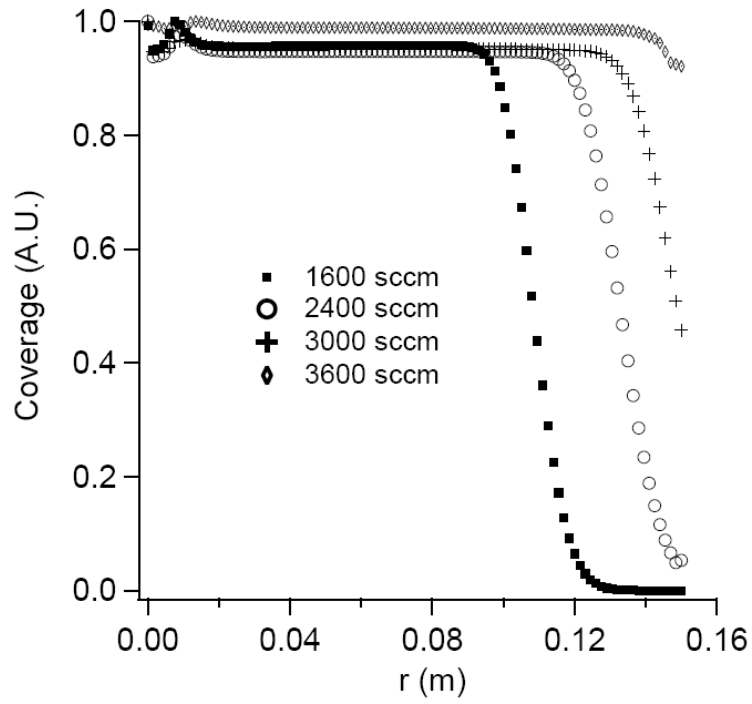


Figure A3.11. Plot of Deposition Profile.

Model predictions for particle deposition on 300 mm silicon wafer at various flow rates.

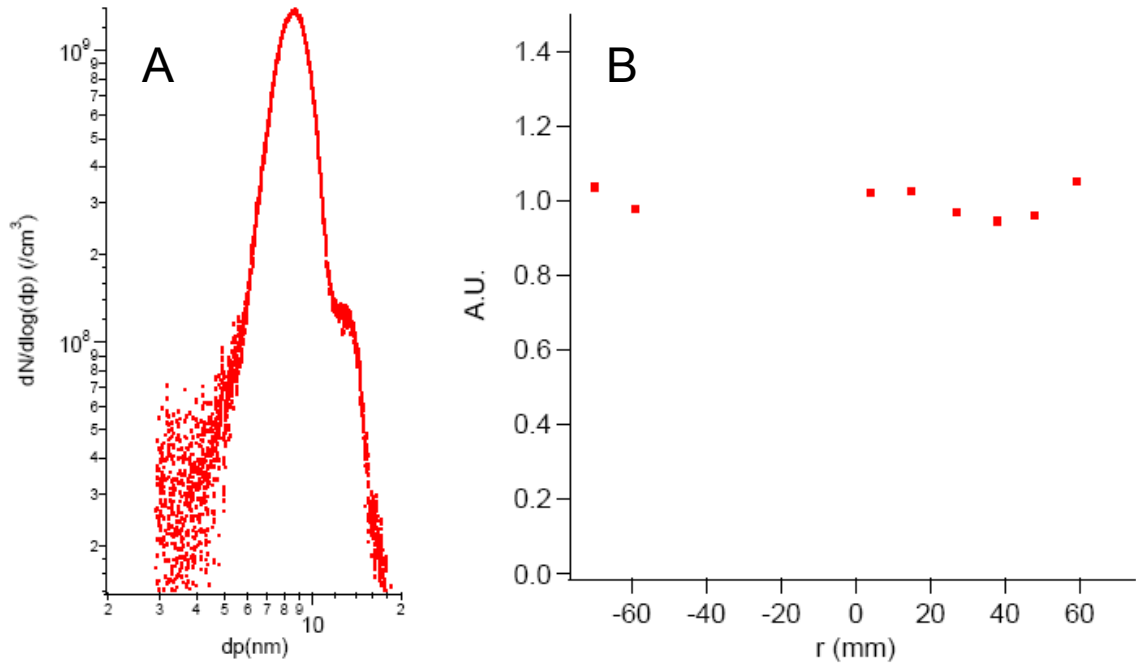


Figure A3.12. Particle Size Distribution and Wafer Coverage.

PSD and particle coverage on 150 mm silicon wafer. AFM images are seen in Figure A3.13. (A) PSD of nanoparticles deposited on 150 mm wafer. (B) Particle coverage normalized by mean.

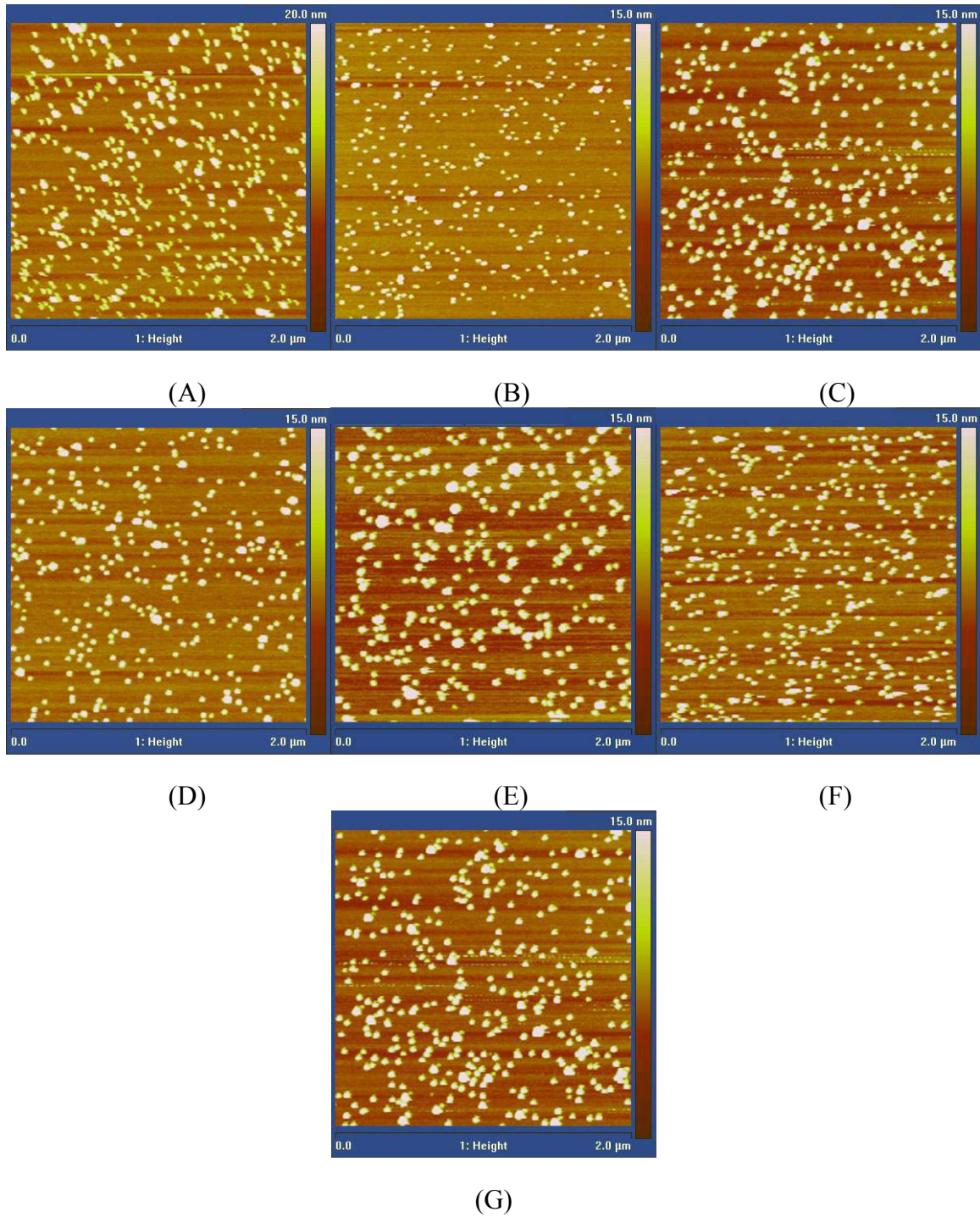


Figure A3.13. AFM Images of Deposited Particles.

AFM images of particle deposition on 150 mm wafer. (A) $r = 70$ mm, (B) $r = 59$ mm, (C) $r = 48$ mm, (D) $r = 38$ mm, (E) $r = 27$ mm, (F) $r = 15$ mm, (G) $r = 4$ mm.

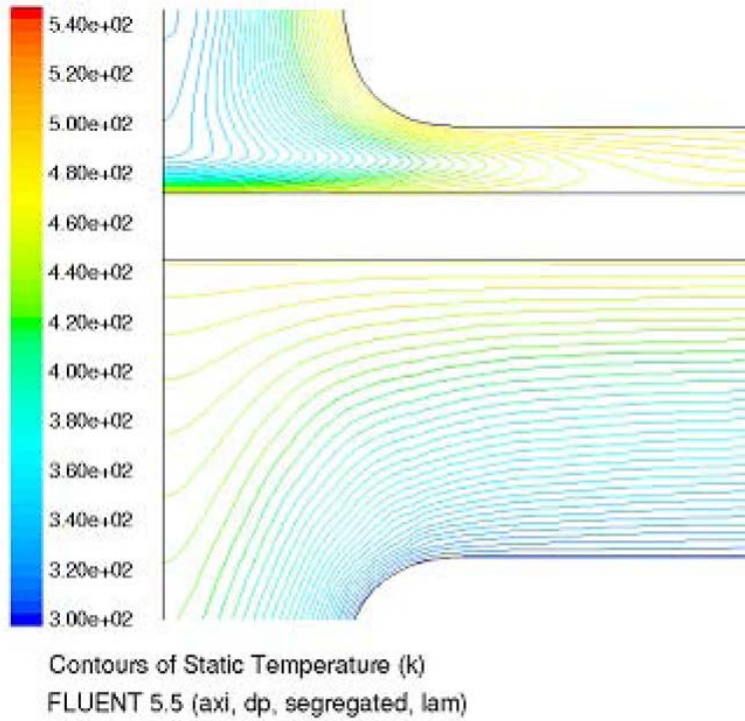


Figure A3.14. Modeled Inlet Temperature Distribution without Inlet Heating.

Model predicts an unfavorable temperature gradient at the wafer surface when the aerosol is not preheated.

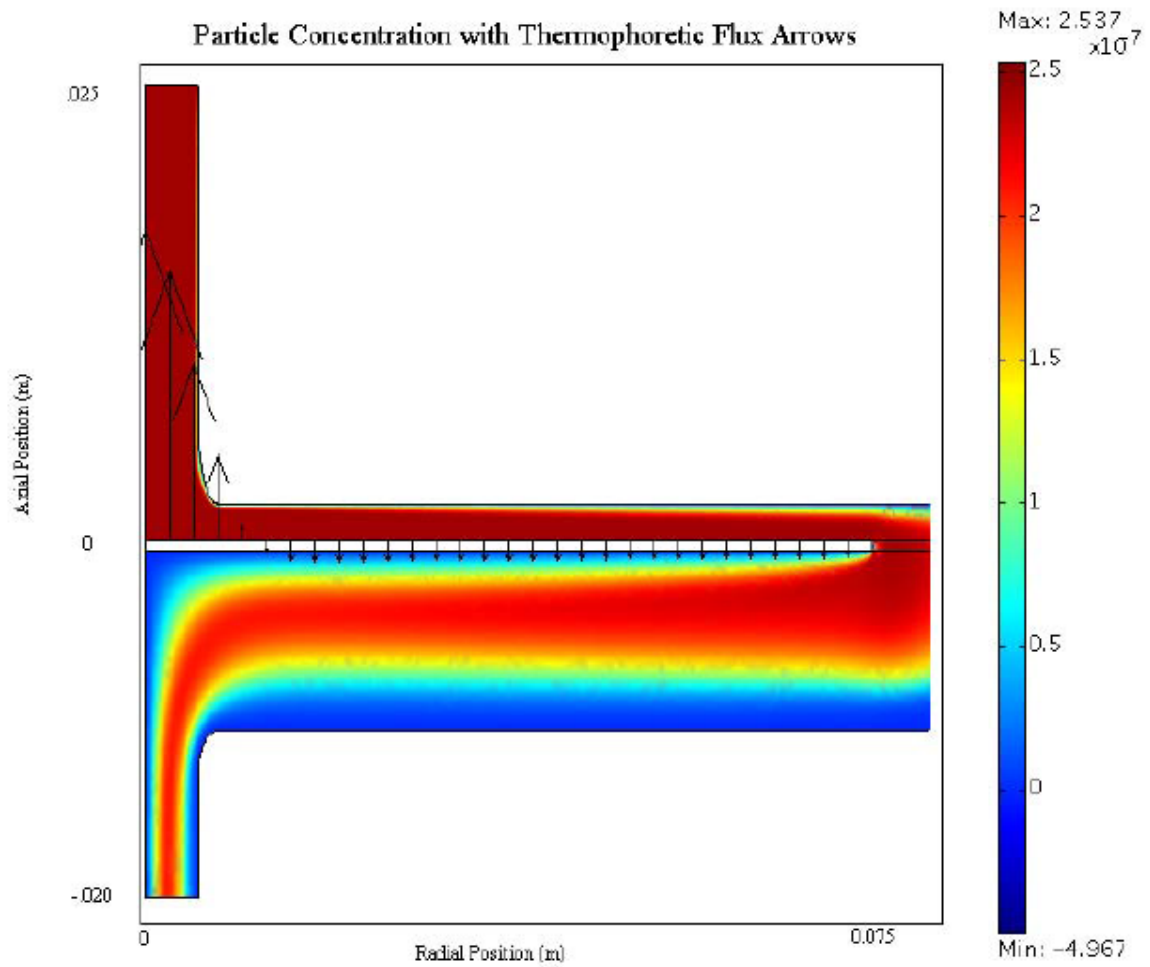


Figure A3.15. Deposition Profile without Inlet Heating.

Model predicts the lack of deposition at the wafer center if the aerosol is not preheated.

The arrows are proportional to the magnitude of thermophoretic particle flux.

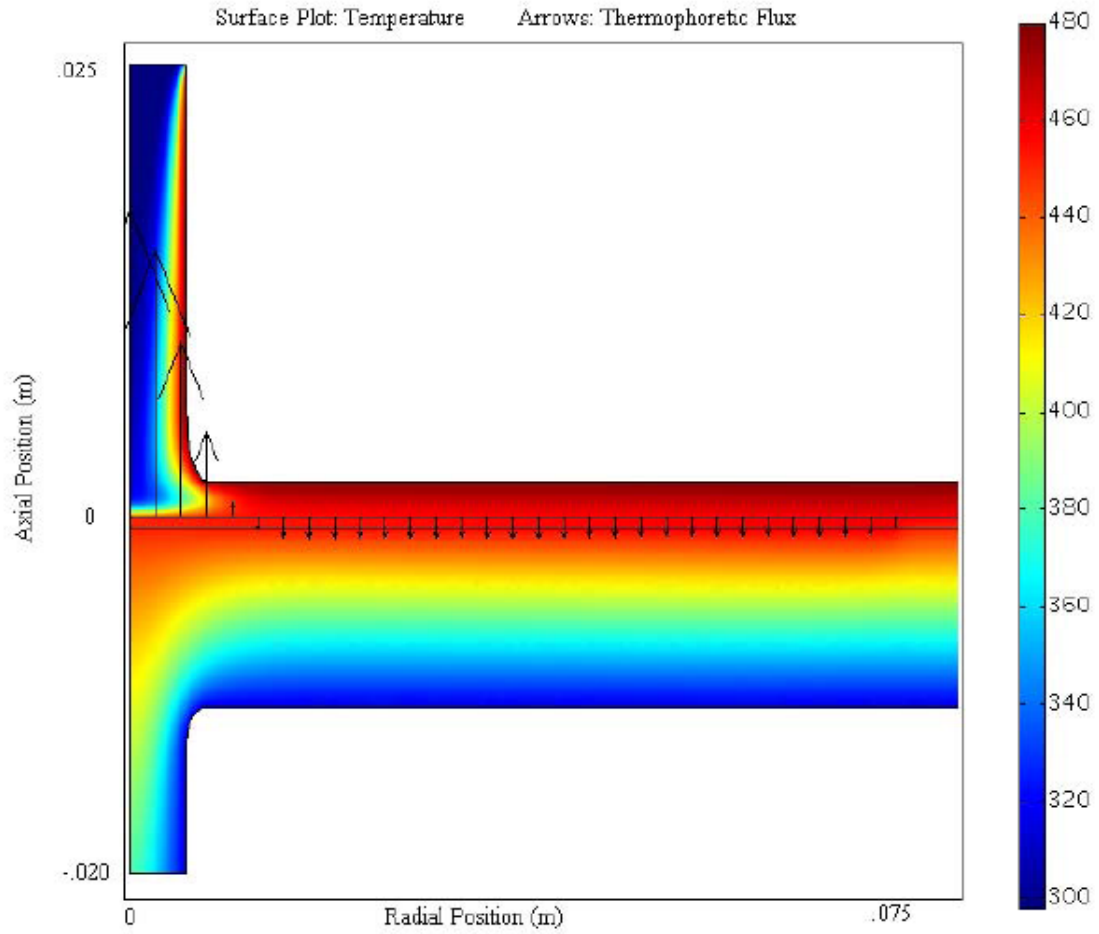


Figure A3.16. Particle Deposition without Inlet Heating.

Modeling in Femlab corroborates the predicted reversed temperature gradient when aerosol is not preheated.

References

1. U. Banin, Y. Cao, D. Katz, and O. Millo, *Nature*, **400**, 542, 1999.
2. M. Bruchez Jr, M. Moronne, P. Gin, S. Weiss, and A. Alivisatos, *Science*, **281**, 2013, 1998.
3. E. Klarreich, *Nature*, **413**, 450, 2001.
4. M. Han, X. Gao, J. Su, and S. Nie, *Nature Biotechnology*, **19**, 631, 2001.
5. P. Miquel, and J. Katz, *Journal of Material Research*, **9**, 746, 1994.
6. M. Glikin, *Theoretical Foundations of Chemical Engineering*, **30**, 390, 1996.
7. M. Glikin, D. Kutakova, and I. Glikina, *Adsorption Science and Technology*, **19**, 101, 2001.
8. R. Houriet, R. Vacassy, and H. Hofmann, *NanoStructured Materials*, **11**, 1155, 1999.
9. M. Glikin, D. Kutakova, and E. Prin, *Chemical Engineering Science*, **54**, 4337, 1999.
10. T. Johannessen, J. Jensen, M. Mosleh, J. Johansen, U. Quaade, and H. Livbjerg, *Chemical Engineering Research and Design*, **82**, 1444, 2004.
11. M. Glikin, I. Glikina, and E. Kauffeldt, *Adsorption Science and Technology*, **23**, 135, 2005.
12. W. Teoh, L. Mädler, D. Beydoun, S. Pratsinis, and R. Amal, *Chemical Engineering Science*, **60**, 5852, 2005.
13. J. Liqiang, W. Baiqi, X. Baifu, L. Shudan, S. Keying, C. Weimin, and F. Honggang, *Journal of Solid State Chemistry*, **177**, 4221, 2004.
14. H. Bai, C. Chen, C. Lin, W. Den, and C. Changs, *Industrial and Engineering Chemical Research*, **43**, 7200, 2004.
15. S. Coe, W. Woo, M. Bawendi, Bulovi, and V. cacute, *Nature*, **420**, 800, 2002.

16. M. Gao, J. Sun, E. Dulkeith, N. Gaponik, U. Lemmer, and J. Feldmann, *Langmuir*, **18**, 4098, 2002.
17. V. Colvin, M. Schlamp, and A. Alivisatos, *Nature*, **370**, 354, 1994.
18. R. Walters, G. Bourianoff, and H. Atwater, *Luminescence*, **600**, 700, 2005.
19. S. Kershaw, M. Harrison, A. Rogach, and A. Kornowski, *IEEE Journal of Selected Topics in Quantum Electronics*, **6**, 534, 2000.
20. A. Malko, A. Mikhailovsky, M. Petruska, J. Hollingsworth, H. Htoon, M. Bawendi, and V. Klimov, *Applied Physics Letters*, **81**, 1303, 2002.
21. R. Walters, P. Kik, J. Casperson, H. Atwater, R. Lindstedt, M. Giorgi, and G. Bourianoff, *Applied Physics Letters*, **85**, 2622, 2004.
22. D. Klein, R. Roth, A. Lim, A. Alivisatos, and P. McEuen, *Nature*, **389**, 699, 1997.
23. J. Holmes, K. Ziegler, R. Doty, L. Pell, K. Johnston, and B. Korgel, *Journal of the American Chemical Society*, **123**, 3743, 2001.
24. L. Pell, A. Schricker, F. Mikulec, and B. Korgel, *Langmuir*, **20**, 6546, 2004.
25. P. Shah, T. Hanrath, K. Johnston, and B. Korgel, *Journal of Physical Chemistry B*, **108**, 9574, 2004.
26. D. English, L. Pell, Z. Yu, P. Barbara, and B. Korgel, *Nano Letters*, **2**, 681, 2002.
27. S. Tiwari, F. Rana, H. Hanafi, A. Hartstein, E. Crabbe, and K. Chan, *Applied Physics Letters*, **68**, 1377, 1996.
28. T. Feng, H. Yu, M. Dicken, J. Heath, and H. Atwater, *Applied Physics Letters*, **86**, 033103, 2005.
29. M. Brongersma, A. Polman, K. Min, and H. Atwater, *Journal of Applied Physics*, **86**, 759, 1999.

30. M. Ostraat, J. De Blauwe, M. Green, L. Bell, H. Atwater, and R. Flagan, *Journal of the Electrochemical Society*, **148**, G265, 2001.
31. M. Ostraat, J. De Blauwe, M. Green, L. Bell, M. Brongersma, J. Casperson, R. Flagan, and H. Atwater, *Applied Physics Letters*, **79**, 433, 2001.
32. H. Rumpf, K. Sommer, and K. Steier, *International Chemical Engineering*, **18**, 1978.
33. H. Rumpf, K. Sommer, and K. Steier, *Chemie Ingenieur Technik*, **48**, 300, 1976.
34. D. Phares, G. Smedley, and R. Flagan, *Journal of Aerosol Science*, **31**, 1335, 2000.
35. G. Smedley, D. Phares, and R. Flagan, *Experiments in Fluids*, **26**, 324, 1999.
36. G. Smedley, D. Phares, and R. Flagan, *Experiments in Fluids*, **26**, 116, 1999.
37. G. Ulrich, *Chemical Engineering News*, **62**, 22, 1984.
38. S. Pratsinis, *Progress in Energy and Combustion Science*, **24**, 197, 1998.
39. W. Stark, and S. Pratsinis, *Powder technology*, **126**, 103, 2002.
40. R. Mueller, L. Mädler, and S. Pratsinis, *Chemical Engineering Science*, **58**, 1969, 2003.
41. W. R. Cannon, S. C. Danforth, J. S. Haggerty, and R. A. Marra, *American Ceramic Society Bulletin*, **59**, 1980.
42. W. R. Cannon, S. C. Danforth, J. H. Flint, K. S. Lai, and J. S. Haggerty, *American Ceramic Society Bulletin*, **58**, 1979.
43. H. Branz, L. Liem, C. Harris, S. Fan, J. Flint, D. Adler, and J. Haggerty, *Solar cells*, **21**, 177, 1987.
44. U. Kortshagen, U. Bhandarkar, M. Swihart, and S. Girshick, *Pure and Applied Chemistry*, **71**, 1871, 1999.
45. N. Rao, S. Girshick, J. Heberlein, P. McMurry, S. Jones, D. Hansen, and B. Micheel, *Plasma Chemistry and Plasma Processing*, **15**, 581, 1995.

46. D. Holunga, R. Flagan, and H. Atwater, *Industrial and Engineering Chemical Research*, **44**, 6332, 2005.
47. R. Bird, W. Stewart, and E. Lightfoot, *Transport Phenomena* (John Wiley and Sons, New York, New York, ed. 1st, 1960).
48. R. Flagan, and M. Lunden, *Materials Science and Engineering. A, Structural Materials: Properties, Microstructure and Processing*, **204**, 113, 1995.
49. R. C. Flagan, and J. H. Seinfeld, *Fundamentals of Air Pollution Engineering*. (Prentice Hall, Englewood Cliffs, NJ, 1998).
50. S. Corrsin, *AIChE Journal*, **3**, 329, 1957.
51. S. Zhang, Y. Akutsu, L. Russell, R. Flagan, and J. Seinfeld, *Aerosol Science and Technology*, **23**, 357, 1995.
52. S. Zhang, and R. Flagan, *Journal of Aerosol Science*, **27**, 1179, 1996.
53. R. P. Camata, H. A. Atwater, and R. C. Flagan, *Journal of Aerosol Science*, **32**, 583, 2001.
54. D. Collins, R. Flagan, and J. Seinfeld, *Aerosol Science and Technology*, **36**, 1, 2002.
55. R. Flagan, *Aerosol Science and Technology*, **30**, 556, 1999.